

# Accelerated Innovation Deployment (AID) Demonstration Project: Testing, Performance Evaluation, and Documentation of the Little Silver Creek Bridge

Final Report  
August 2018



IOWA STATE UNIVERSITY  
Institute for Transportation

Sponsored by  
Federal Highway Administration  
Iowa Department of Transportation  
(InTrans Project 14-524)

## **About the Bridge Engineering Center**

The mission of the Bridge Engineering Center (BEC) at Iowa State University is to conduct research on bridge technologies to help bridge designers/owners design, build, and maintain long-lasting bridges.

### **Disclaimer Notice**

The contents of this report reflect the views of the authors, who are responsible for the facts and the accuracy of the information presented herein. The opinions, findings and conclusions expressed in this publication are those of the authors and not necessarily those of the sponsors.

The sponsors assume no liability for the contents or use of the information contained in this document. This report does not constitute a standard, specification, or regulation.

The sponsors do not endorse products or manufacturers. Trademarks or manufacturers' names appear in this report only because they are considered essential to the objective of the document.

### **Non-Discrimination Statement**

Iowa State University does not discriminate on the basis of race, color, age, ethnicity, religion, national origin, pregnancy, sexual orientation, gender identity, genetic information, sex, marital status, disability, or status as a U.S. veteran. Inquiries regarding non-discrimination policies may be directed to Office of Equal Opportunity, Title IX/ADA Coordinator, and Affirmative Action Officer, 3350 Beardshear Hall, Ames, Iowa 50011, 515-294-7612, email [eooffice@iastate.edu](mailto:eooffice@iastate.edu).

### **Iowa Department of Transportation Statements**

Federal and state laws prohibit employment and/or public accommodation discrimination on the basis of age, color, creed, disability, gender identity, national origin, pregnancy, race, religion, sex, sexual orientation or veteran's status. If you believe you have been discriminated against, please contact the Iowa Civil Rights Commission at 800-457-4416 or Iowa Department of Transportation's affirmative action officer. If you need accommodations because of a disability to access the Iowa Department of Transportation's services, contact the agency's affirmative action officer at 800-262-0003.

The preparation of this report was financed in part through funds provided by the Iowa Department of Transportation through its "Second Revised Agreement for the Management of Research Conducted by Iowa State University for the Iowa Department of Transportation" and its amendments.

The opinions, findings, and conclusions expressed in this publication are those of the authors and not necessarily those of the Iowa Department of Transportation or the U.S. Department of Transportation Federal Highway Administration.

### Technical Report Documentation Page

<b>1. Report No.</b> InTrans Project 14-524	<b>2. Government Accession No.</b>	<b>3. Recipient's Catalog No.</b>	
<b>4. Title and Subtitle</b> Accelerated Innovation Deployment (AID) Demonstration Project: Testing, Performance Evaluation, and Documentation of the Little Silver Creek Bridge		<b>5. Report Date</b> August 2018	
		<b>6. Performing Organization Code</b>	
<b>7. Author(s)</b> Ahmad Abu-Hawash (orcid.org/0000-0003-0751-7574), Yaohua "Jimmy" Deng (orcid.org/0000-0003-0779-6112), Andrew Putz (orcid.org/0000-0001-7389-0583), and Brent Phares (orcid.org/0000-0001-5894-4774)		<b>8. Performing Organization Report No.</b> InTrans Project 14-524	
<b>9. Performing Organization Name and Address</b> Bridge Engineering Center Iowa State University 2711 South Loop Drive, Suite 4700 Ames, IA 50010-8664		<b>10. Work Unit No. (TRAVIS)</b>	
		<b>11. Contract or Grant No.</b>	
<b>12. Sponsoring Organization Name and Address</b> Iowa Department of Transportation      Federal Highway Administration 800 Lincoln Way                              1200 New Jersey Avenue, SE Ames, IA 50010                                Washington, DC 20590		<b>13. Type of Report and Period Covered</b> Final Report	
		<b>14. Sponsoring Agency Code</b>	
<b>15. Supplementary Notes</b> Visit <a href="http://www.intrans.iastate.edu">www.intrans.iastate.edu</a> for color pdfs of this and other research reports.			
<b>16. Abstract</b> <p>The objective of this project is to evaluate the performance of a second-generation accelerated bridge construction (ABC) bridge that utilizes two types of continuity connections: the transverse joint at pier diaphragms and the longitudinal joint between precast superstructure/deck units.</p> <p>The bridge replacement project located on IA 92 over Little Silver Creek in Pottawattamie County, Iowa was used to demonstrate a second-generation ABC technique that had been previously used in Iowa. As a part of the holistic evaluation, the performance of an ultra-high performance concrete (UHPC) longitudinal joint detail and a high-performance material (HPM) transverse joint detail were studied through laboratory testing and numerical simulations. Additionally, field testing was conducted to evaluate the in-place integrity of the bridge.</p> <p>The goals of this project are to demonstrate the performance and benefits of the ABC techniques using prefabricated bridge elements and systems (PBES) and HPMS and to contribute toward increased adoption of the technologies by Iowa and other states.</p> <p>Through this project, the Iowa DOT gained valuable insights into the innovative ABC techniques used. The following were some of the lessons learned:</p> <ul style="list-style-type: none"> <li>• UHPC is an excellent material for longitudinal closure pour connections.</li> <li>• There may not be a need to use a compression block for the beam-to-beam transverse closure pours on a similar ABC project in the future.</li> <li>• The UHPC longitudinal joints and the HPC transverse joints at the pier location are sufficient for the modular bridge systems of ABC projects.</li> </ul>			
<b>17. Key Words</b> accelerated bridge construction—ABC joints—bridge replacement— longitudinal bridge connections—transverse bridge connections—ultra-high performance concrete		<b>18. Distribution Statement</b> No restrictions.	
<b>19. Security Classification (of this report)</b> Unclassified.	<b>20. Security Classification (of this page)</b> Unclassified.	<b>21. No. of Pages</b> 110	<b>22. Price</b> NA



# **ACCELERATED INNOVATION DEPLOYMENT (AID) DEMONSTRATION PROJECT: TESTING, PERFORMANCE EVALUATION, AND DOCUMENTATION OF THE LITTLE SILVER CREEK BRIDGE**

**Final Report  
August 2018**

**Principal Investigator**  
Brent Phares, Director  
Bridge Engineering Center, Iowa State University

**Co-Principal Investigator**  
Yaohua “Jimmy” Deng, Bridge Engineer  
Bridge Engineering Center, Iowa State University

**Authors**  
Ahmad Abu-Hawash, Yaohua “Jimmy” Deng, Andrew Putz, and Brent Phares

Sponsored by  
Iowa Department of Transportation and  
Federal Highway Administration  
Accelerated Innovation Deployment (AID) Program

Preparation of this report was financed in part  
through funds provided by the Iowa Department of Transportation  
through its Research Management Agreement with the  
Institute for Transportation  
(InTrans Project 14-524)

A report from  
**Bridge Engineering Center**  
**Institute for Transportation**  
**Iowa State University**  
2711 South Loop Drive, Suite 4700  
Ames, IA 50010-8664  
Phone: 515-294-8103 / Fax: 515-294-0467  
[www.intrans.iastate.edu](http://www.intrans.iastate.edu)



## TABLE OF CONTENTS

ACKNOWLEDGMENTS .....	ix
EXECUTIVE SUMMARY .....	xi
Schedule .....	xi
Quality.....	xi
User Costs .....	xii
User Satisfaction .....	xii
Lessons Learned.....	xii
INTRODUCTION .....	1
Accelerated Innovation Deployment (AID) Demonstration Grants .....	1
Report Scope and Organization .....	1
Project Overview .....	1
PROJECT DETAILS .....	2
Background.....	2
Project Description.....	4
Data Collection and Analysis.....	5
LABORATORY TESTING, RESULTS, AND DISCUSSIONS.....	6
Laboratory Testing of Longitudinal Connections.....	8
Test Results and Discussions for Longitudinal Connections.....	17
Laboratory Testing of Transverse Connections.....	31
Test Results and Discussions for Transverse Connections.....	40
Numerical Simulation, Results, and Discussions .....	56
FIELD TESTING, RESULTS, AND DISCUSSIONS.....	70
Instrumentation and Loading Plan .....	70
Live Load Distribution Factors.....	74
FE Modeling of Little Silver Creek Bridge .....	78
Analyses and Comparisons of Measured and Predicted Results .....	82
SUMMARY AND CONCLUSIONS .....	91
TECHNOLOGY TRANSFER.....	94
REFERENCES .....	95

## LIST OF FIGURES

Figure 1. Location of the Little Silver Creek Bridge .....	3
Figure 2. Little Silver Creek Bridge on IA 92 .....	6
Figure 3. Supports at abutments and piers .....	7
Figure 4. Constructed Little Silver Creek Bridge .....	8
Figure 5. Segment for design of longitudinal connections .....	9
Figure 6. Details of jointed specimens.....	10
Figure 7. Details of jointless specimens .....	11
Figure 8. Fabrication sequence of jointless and jointed longitudinal connection specimens .....	13
Figure 9. Jointed specimen curing and ponding tests .....	15
Figure 10. Longitudinal connection strength tests and instrumentation .....	16
Figure 11. Examination of ponding test.....	17
Figure 12. Crack patterns.....	18
Figure 13. Flexural cracking.....	19
Figure 14. Failure cracks.....	20
Figure 15. Longitudinal connection joint investigation.....	20
Figure 16. Comparison of longitudinal connection joint surfaces.....	21
Figure 17. Load vs. strain - jointless Specimen C1 (1st Test) .....	22
Figure 18. Load vs. strain - jointless Specimen C1 (2nd Test).....	22
Figure 19. Load vs. strain - jointless Specimen C2 .....	23
Figure 20. Load vs. strain - jointless Specimen C3 .....	23
Figure 21. Load vs. strain - Specimen J1 (Plastic Form Liner-UHPC).....	24
Figure 22. Load vs. strain - Specimen J2 (Form-Retarder-UHPC) .....	24
Figure 23. Load vs. strain - Specimen J4 (Rubber Form Liner-UHPC).....	25
Figure 24. Load vs. strain - Specimen K1 (Form-Retarder-K-UHPC).....	25
Figure 25. Load vs. strain - Specimen K2 (Plastic Form Liner-K-UHPC).....	26
Figure 26. Load vs. strain - Specimen K3 (Rubber Form Liner-K-UHPC) .....	26
Figure 27. Load vs. deflection for all Test A specimens .....	31
Figure 28. Segment for design of transverse connections .....	32
Figure 29. Longitudinal joint specimen details.....	33
Figure 30. Reinforcing bar layout of deck .....	34
Figure 31. Details of the compression block .....	35
Figure 32. Transverse connection fabrication procedure.....	36
Figure 33. Transverse connection strength test setup details.....	37
Figure 34. Transverse connection strength test setup .....	38
Figure 35. Strain gauges on steel bars embedded in specimen deck panels .....	39
Figure 36. Strain gauges on specimen steel girders and compression block .....	40
Figure 37. Crack formations on deck slab for each specimen .....	42
Figure 38. Diaphragm cracks on short side for each specimen .....	42
Figure 39. Diaphragm cracks on long side for each specimen .....	43
Figure 40. Localized failure of Specimen II under the loading point.....	43
Figure 41. Specimen II reinforcing steel examination.....	44
Figure 42. Cracking of diaphragm for Specimen I .....	45
Figure 43. Revised loading configuration of Specimen I .....	45
Figure 44. Transverse connection load vs. strain 6 in. west of the diaphragm - Specimen I .....	46

Figure 45. Transverse connection load vs. strain 6 in. west of the diaphragm - Specimen II .....	47
Figure 46. Transverse connection load vs. strain center of the diaphragm - Specimen I .....	47
Figure 47. Transverse connection load vs. strain center of the diaphragm - Specimen II .....	48
Figure 48. Transverse connection load vs. strain 6 in. east of the diaphragm - Specimen I .....	48
Figure 49. Transverse connection load vs. strain 6 in. east of the diaphragm - Specimen II .....	49
Figure 50. Transverse strain values 6 in. west of the diaphragm for the two specimens .....	51
Figure 51. Transverse strain values center of diaphragm for the two specimens .....	51
Figure 52. Transverse strain values 6 in. east of the diaphragm for the two specimens.....	51
Figure 53. Load vs. strain on girder at midpoint for the two specimens .....	52
Figure 54. Load vs. strain on girder 6 in. outside of diaphragm for the two specimens.....	53
Figure 55. Load vs. strain on compression block .....	54
Figure 56. Load vs. displacement of both specimens .....	54
Figure 57. West vs. east loading rates.....	55
Figure 58. FE model of jointed (or jointless) specimens .....	57
Figure 59. Comparison of relationships obtained from test results and FE models .....	59
Figure 60. Stresses in concrete and reinforcing bar at failure predicted by FE models and forces in developed STM model .....	61
Figure 61. Finite element model of specimens .....	64
Figure 62. Strains in steel bars - Specimen I .....	65
Figure 63. Strain comparison in steel bars at the diaphragm center .....	66
Figure 64. Strains in steel girders 6 in. from diaphragm .....	67
Figure 65. Strain comparison in compression block.....	67
Figure 66. Strains or stress in different components of specimens.....	68
Figure 67. Strain gauges installed on the bridge-Test #1.....	71
Figure 68. Strain gauges installed on the bridge-Test #2.....	72
Figure 69. Load paths on the bridge .....	73
Figure 70. Configurations of dump trucks for Test #1 and Test #2.....	73
Figure 71. Derived LDFs at Section M for Load Paths 1 and 2 .....	75
Figure 72. Details of Little Silver Creek Bridge FE model .....	79
Figure 73. Sensors on girder cross-section – positive moment region .....	81
Figure 74. Re-named strain gauges on bottom flanges.....	83
Figure 75. Strain comparisons between FE and test results at Section A.....	86
Figure 76. Strain comparisons between FE and test results at Section M .....	87
Figure 77. Strain comparisons between FE and test results at Section P1 .....	88
Figure 78. Strain comparisons between FE and test results at Section P2 .....	89

## LIST OF TABLES

Table 1. Summary of all test results.....	27
Table 2. Test results for each surface preparation technique.....	28
Table 3. Summary of results by joint material.....	29
Table 4. Compressive strength test results for joint materials .....	30
Table 5. HPC concrete deck and diaphragm compressive strength tests results .....	41
Table 6. Distance from loading to gauge locations.....	41
Table 7. Summary of test results at each cross-section .....	50
Table 8. Summary of critical test results .....	55
Table 9. Summary and comparisons of test and FE results .....	60
Table 10. Summary of results .....	65
Table 11. Dump truck weight details .....	74
Table 12. Maximum LDFs at different bridge cross-sections and under different load paths – Test #1 .....	76
Table 13. Maximum LDFs at different bridge cross-sections and under different load paths – Test #2.....	77
Table 14. Comparisons of LDFs with those estimated using AASHTO LRFD equations – Test #1 .....	77
Table 15. Comparisons of LDFs with those estimated using AASHTO LRFD equations – Test #2.....	78
Table 16. Little Silver Creek Bridge parameter values and ranges .....	80
Table 17. Neutral axis determination at different girder cross-sections .....	82
Table 18. Optimized parameter values .....	84
Table 19. Statistical values for optimization process.....	85

## **ACKNOWLEDGMENTS**

The research team would like to acknowledge the Federal Highway Administration for an Accelerated Innovation Deployment (AID) Demonstration grant used to help fund this project.



## **EXECUTIVE SUMMARY**

The IA 92 over Little Silver Creek bridge replacement project incorporates numerous innovative technologies contributing toward advancements in project safety, construction schedule, construction impact, project quality, user satisfaction, and service life.

This bridge replacement project represents the Iowa Department of Transportation's (DOT's) second-generation design efforts for accelerated bridge construction (ABC) using prefabricated bridge elements and systems (PBES). Generally based on the US 6 over Keg Creek modular decked beam concept in Pottawattamie County, Iowa, the Little Silver Creek Bridge project (also in Pottawattamie County, Iowa), builds on the experience gained and lessons learned from the Iowa DOT's 2011 Second Strategic Highway Research Program (SHRP2) Project R04 demonstration project.

The Little Silver Creek Bridge replacement project was recognized by the Federal Highway Administration (FHWA) for accelerated implementation and adoption of innovative technology in highway transportation. This project was the recipient of an incentive funding grant of \$1 million as a part of FHWA's Accelerated Innovation Deployment (AID) program.

The objective of this project is to evaluate the performance of a second-generation ABC bridge that utilizes two types of continuity connections: the transverse joint at pier diaphragms and the longitudinal joint between precast superstructure/deck units.

The goals of this project are to demonstrate the performance and benefits of the ABC techniques using PBES and high-performance materials (HPMs) and to contribute toward increased adoption of the technologies by Iowa and other states.

### **Schedule**

Streamlining the project delivery process results in earlier overall project completion. This in turn provides greater service to our end users sooner. The combination of accelerated construction techniques reduced the duration that highway users were impacted. It is estimated that the construction time would be six months under non-accelerated construction; however, for this project, the actual construction time requiring road closure was only 24 days.

The innovative construction concept reduced the traffic detour duration by more than 85%. The shorter duration of closure relates to a significant reduction of total out-of-distance trip time as compared to the duration for more traditional construction methods.

### **Quality**

- It is anticipated that the use of prefabricated/precast components has improved quality and long-term performance of the bridge given that the entire superstructure was produced in a

casting yard. Strict compliance with specifications was ensured.

- Improved service life (100+ years) will be achieved through the use of HPMs (i.e. stainless steel and UHPC) and prefabricated elements with the goal of significant reduction in future maintenance.
- Although no longer an innovation in Iowa, improved consolidation was achieved from using fully contained flooded backfill treatment. Problems with settlement that results in bumps at the bridge are not anticipated; thus, a better ride will increase driver satisfaction.
- This project did not require specialized construction equipment. In fact, one of the most significant advantages of this bridge system is that it was constructed by a smaller, local contractor using commonly-available construction equipment. The elimination of specialized equipment brings the concept of ABC to within the reach of virtually all bridge owners and contractors around the country.

### **User Costs**

As mentioned above, the project was completed with only 24 days of closure. An engineer's estimate indicates that a typical bridge construction project of this type would require 115 working days. User costs at this location have been estimated by the Iowa DOT Office of Contracts to be approximately \$9,000 per day, resulting in a user cost savings of \$846,000.

### **User Satisfaction**

Given that a similar project delivery had been completed in the vicinity of the project site, coupled with the fact that a similar user satisfaction survey was completed for that project, no additional user satisfaction information was collected for this project. However, the previous project (the Keg Creek Bridge, also in Pottawattamie County) satisfaction survey indicated that about 85% of respondents agreed that closing the roadway was important.

Similarly, about 97% of respondents were satisfied or somewhat satisfied with the level of communication from the Iowa DOT regarding the construction work with about 84% relying upon radio for communications.

Not surprisingly, 85% of respondents indicated that the inconvenience associated with construction was minimal and the remainder indicated moderate inconvenience. No respondents indicated an impact on their plans to visit businesses along the corridor.

### **Lessons Learned**

Through this project, the Iowa DOT gained valuable insights into the innovative ABC techniques used. The following were some of the lessons learned:

- UHPC is an excellent material for longitudinal closure pour connections.
- There may not be a need to use a compression block for the beam-to-beam transverse closure pours on a similar ABC project in the future.
- The UHPC longitudinal joints and the HPC transverse joints at the pier location are sufficient for the modular bridge systems of ABC projects.



## **INTRODUCTION**

### **Accelerated Innovation Deployment (AID) Demonstration Grants**

The Accelerated Innovation Deployment (AID) program is one aspect of the multi-faceted Technology and Innovation Deployment Program (TIDP) approach, which provides funding and other resources to offset the risk of trying an innovation. The AID Demonstration funds are available for any project eligible for assistance under Title 23 of the United States Code.

Projects eligible for funding include proven innovative practices or technologies, such as those included in the Every Day Counts (EDC) initiative. Innovations may include infrastructure and non-infrastructure strategies or activities, which the award recipient intends to implement and adopt as a significant improvement from their conventional practice.

Entities eligible to apply included state departments of transportation (DOTs), Federal Land Management Agencies, and tribal governments, as well as metropolitan planning organizations (MPOs) and local governments, which applied through their state DOTs as subrecipients.

### **Report Scope and Organization**

This interim report documents the Iowa DOT demonstration grant award for the replacement of the IA 92 bridge over Little Silver Creek using an accelerated bridge construction (ABC) technique: prefabricated bridge elements and systems (PBES) connected by closure pour connections. This report presents details relevant to the employed project innovation(s), the overarching TIDP goals, performance metrics measurement and analysis, lessons learned, and the status of activities related to adoption of the PBES and closure pour connections as conventional practice by the Iowa DOT.

### **Project Overview**

This project demonstrates the use of prefabricated bridge elements and systems (PBES) and high performance materials (HPMs) to replace a bridge located on IA 92 over Little Silver Creek in Pottawattamie County, Iowa. The innovation of the project was to utilize a rapid renewal technique to address several issues associated with bridge replacement projects including increased traffic congestion, work-zone safety concerns, and economic constraints. The project contributes to a faster construction schedule, reduced construction impact, improved project quality, greater user satisfaction, and longer service life.

This project addressed the following TIDP goal: improving highway efficiency, safety, mobility, reliability, service life, environmental protection, sustainability, and quality, while reducing project completion/construction time. The goals of this project are to demonstrate the performance and benefits of ABC techniques using prefabricated bridge elements and high performance materials and to contribute toward increased adoption of the technologies by Iowa and other states.

## **PROJECT DETAILS**

### **Background**

Historically, the construction of bridges did not interfere with public transportation. This was primarily due to the fact that these bridges were brand new and constructed simultaneously with the roadway. Nowadays, the already established roadway infrastructure in the US is deteriorating rapidly.

Specifically speaking, the US roadway infrastructure consists of more than 600,000 bridges and about 25% of those bridges are in need of repair or replacement. Currently, the average age of bridges is 44 years and these bridges were typically designed for a life expectancy of 50 years (ASCE 2015).

More than 20% of bridges in Iowa alone are considered structurally deficient, meaning that deterioration is predominant in one or more components, but the bridge is not yet unsafe to use (Mulholland and Vander Wert 2015). This makes Iowa the third worst state in the country in terms of structurally sound bridges (Shoup et al. 2011). With approximately 24,000 bridges throughout the state, repairing all of the deficiencies would not be feasible using traditional construction practices.

New techniques are currently being studied to help manage the required bridge construction throughout the US in the next few years. These new techniques are providing greater safety in the work-zone and fewer impacts on the area surrounding construction, minimizing traffic disturbances, and greatly reducing construction time that impacts traffic. Among these techniques is ABC, which was being developed and studied under the Second Strategic Highway Research Program (SHRP2) and elsewhere.

ABC techniques taking advantage of prefabricated bridge elements and high performance materials are more and more commonly being utilized for bridge replacement projects resulting in minimal road closure time/traffic interruption and re-construction of long-lasting highway bridges. Moving toward increased adoption, these techniques have been utilized in several demonstration bridge projects.

For instance, the goal of the SHRP2 Project R04 was to develop standards and codified language for ABC and to also provide for the construction of demonstration bridges like the Keg Creek Bridge in Pottawattamie County, Iowa, which consisted of several prefabricated steel beam/concrete deck components connected with both transverse and longitudinal closure pours. To address design concerns about performance in the negative moment region, laboratory tests were conducted to evaluate the UHPC transverse full-depth deck joint over the pier of the demonstration bridge (Hartwell 2011).

As part of Iowa's growing program to utilize ABC technologies and approaches, discussions continue about constructing even more of the bridge system using prefabricated bridge elements

and systems (PBES) like those originally used for the Keg Creek Bridge. This continued evolution of promising concepts is a demonstration of the Iowa DOT's commitment to enhancing bridge construction.

The second-generation bridge system was utilized to replace the bridge on IA 92 over Little Silver Creek in Pottawattamie County, Iowa shown in Figure 1.



Map data ©2016 Google Imagery ©2016 DigitalGlobe, USDA Farm Service Agency

**Figure 1. Location of the Little Silver Creek Bridge**

For this project, prefabricated bridge elements were placed adjacent to each other on the substructure and connected using closure pour connections. The use of prefabricated components improves construction quality and reduces traffic disruption time on the bridge site. Longitudinal and transverse closure pour connections were utilized to transfer forces transversely and longitudinally along the bridge.

Longitudinal connections in many ABC systems are an important deck-level component between prefabricated components. These longitudinal connections are heavily stressed by traffic loads and environmental effects, giving rise to a concern about their durability. At this time, one of the most common materials used to complete the longitudinal joints is UHPC, which is an ideal closure material that has high durability, high strength, superior bond action, very low

permeability, and short development lengths for reinforcements (Lafarge Ductal 2011). Materials such as UHPC are commonly utilized in an attempt to provide the strongest and most durable link between adjacent modules. Design of the joint detail used with prefabricated bridge elements is one of the most important aspects of an ABC design because of its role in ensuring a safe, long-lived structure (Lafarge Ductal 2011, Li et al. 2010). Not only do the joints need to provide adequate shear and flexural strength, they need to be easy to construct in the field. The structure becomes more complicated to construct as the joint detail becomes more complex and additional complexity frequently adds construction time. Using UHPC for the longitudinal connections can improve the performance of the longitudinal connection, reduce the connection width, and simplify the reinforcement configurations in the connection (Graybeal 2010).

Due to the potential for concrete crushing and cracking, negative moment transfer above pier supports are still a point of concern when trying to make simple spans continuous for live loads. Transverse connections are generally completed using HPC due to less restrictive geometries than those found in longitudinal connections. HPC is predominantly used to help counter environmental effects that can lead to premature deterioration. The HPC is placed between two adjacent elements over the pier locations to form the diaphragm and bridge deck. This portion of many bridges is of particular importance due to the forces that are imposed at this connection. The forces that are transferred over the pier locations can get very large under heavy traffic loads and growing span lengths. The induced tensile forces are primarily accounted for by the reinforcement in the bridge deck. As such, additional reinforcing bars are added to this location to reduce potential problems and control cracking.

A recent study by the Bridge Engineering Center specifically studied negative moment reinforcement (Phares et al. 2015). The research found that current Iowa DOT requirements for negative moment reinforcement were satisfactory and that the supports do not have any issues with significant cracking.

## **Project Description**

In traditional construction, the concrete diaphragm is the only component used as the compressive force transfer mechanism between prestressed concrete girders. The bridge replacement project evaluated in this work utilizes steel girders and the idea of embedding a steel section in the bottom region of the diaphragm between two adjacent girders was developed. The steel section resembled the design of a concrete masonry unit and is referred to as a steel compression block. The purpose of this block was to better transfer the compressive forces through the concrete diaphragm while eliminating excessive compressive stress seen in the concrete.

The Iowa DOT has made it a priority to move toward delivering bridges with less impact on the traveling public. As such, tools have been developed to determine when and where ABC systems should be used and, also, which are the best systems for a given situation. This demonstration project continues these efforts toward better project delivery.

## **Data Collection and Analysis**

Performance measures consistent with the project goals were jointly established for this project by the Iowa DOT and the FHWA to qualify, not quantify, the effectiveness of the innovation—to inform the AID Demonstration program in working toward best practices, programmatic performance measures, and future decision making guidelines.

Data were collected to determine the impact of using PBES and HPMs on safety, schedule, cost, quality, and user impacts before, during, and after construction and demonstrate the ability to meet the following goals:

- Achieve a safer environment for the traveling public and workers
- Reduce overall project delivery time and associated costs
- Reduce life-cycle costs through producing a high-quality project
- Reduce impacts to the traveling public and businesses in the vicinity
- Satisfy the needs and desires of our customers

## LABORATORY TESTING, RESULTS, AND DISCUSSIONS

As mentioned previously, this project is evaluating the performance and benefits of using PBES connected by closure pour connections. Prefabricated bridge elements fabricated in a controlled environment generally have a high level of quality. However, the closure pour connections commonly used in both the longitudinal and transverse directions can be the most critical components in a modular bridge due to potential issues related to serviceability, ductility, strength, and load transfer.

The bridge replacement project located on IA 92 over Little Silver Creek in Pottawattamie County, Iowa was used to demonstrate a second-generation ABC technique that had been previously used in Iowa. As a part of the holistic evaluation, the performance of a UHPC longitudinal joint detail and an HPC transverse joint detail were studied through laboratory testing and numerical simulations. Additionally, field testing was conducted to evaluate the in-place integrity of the bridge.

The Little Silver Creek Bridge is a skewed three-span steel girder bridge with a length of 234 ft, a roadway width of 44 ft, and a skew angle of 15 degrees. The bridge span lengths are 91, 92, and 51 ft from the west to east. Each span of the bridge has 16 prefabricated modules consisting of two W40×149 girders and a 7-ft wide concrete deck, as shown in Figure 2.

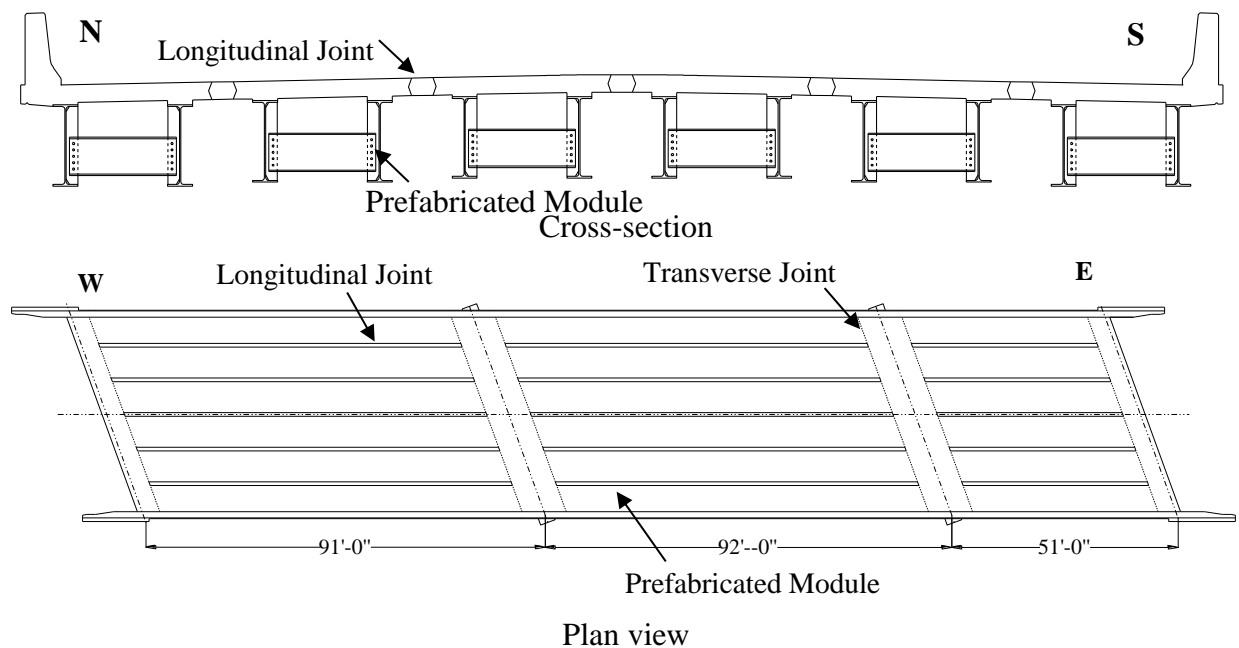


**Figure 2. Little Silver Creek Bridge on IA 92**

The deck depth is 8.25 in. The west and center spans have three diaphragms spaced at 25 ft within the 50-ft girder center region and the eastern span has two diaphragms spaced at 15 ft within the 30-ft girder center region. All diaphragms have a cross-section of MC18x42.7. The

girders within each module are spaced at 4 ft-6 in. and the adjacent girders between two modules are spaced at 3 ft-4 in.

The modules were fabricated at a casting yard located in the immediate vicinity of the bridge. Longitudinal joints with a width of 10 in. were pre-formed between adjacent modules as shown in Figure 2.

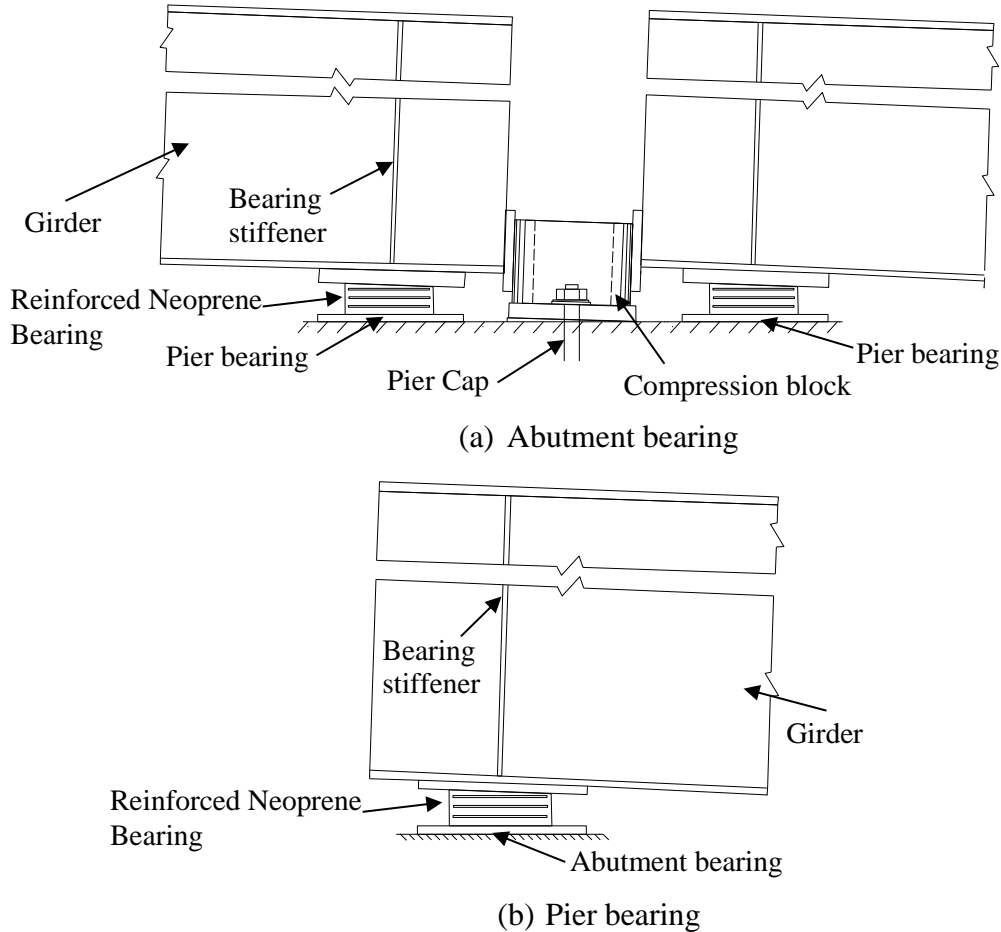


**Figure 3. Supports at abutments and piers**

These joints were specified to be completed with UHPC to establish transverse continuity throughout the structure as alluded to previously. The transverse closure pours for the diaphragms over the piers were completed using HPC to achieve longitudinal continuity at the pier locations as shown in Figure 2(b). The bearing configurations at the abutments and piers are shown in Figure 3(a) and Figure 3(b), respectively.

Note that compression blocks were placed at the bottom of girders as shown in Figure 3(b) and were used to transfer compressive forces at the diaphragms. Several images of the Little Silver Creek Bridge are shown in Figure 4.



**Figure 4. Constructed Little Silver Creek Bridge**

### **Laboratory Testing of Longitudinal Connections**

An experimental program consisting of ponding and strength tests was designed and implemented to investigate the failure modes and flexural behavior of the longitudinal connections. These laboratory tests were completed to establish the behavior of the joint using various finishing methods and materials.

#### *Specimen Design and Fabrication*

The test specimens were designed based on the actual details of the Little Silver Creek Bridge and the details of the segment for the specimen designs are shown in Figure 5.

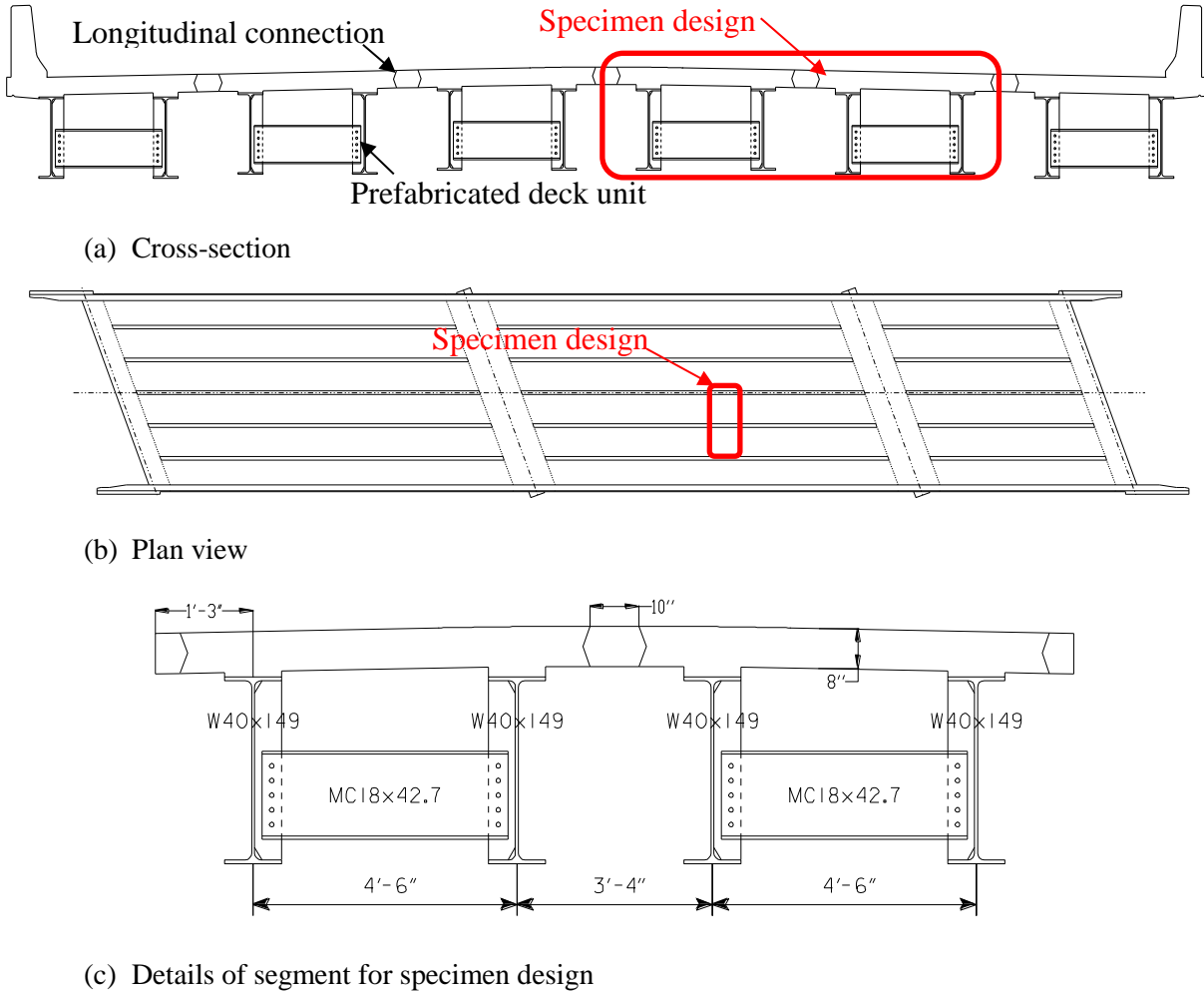
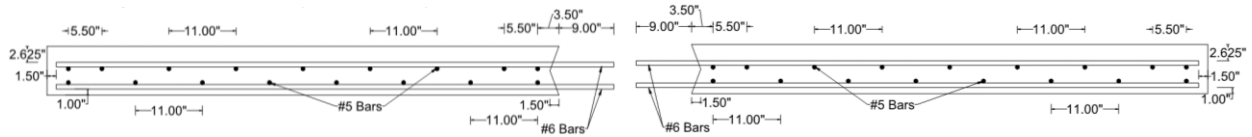


**Figure 5. Segment for design of longitudinal connections**

A total of nine specimens were designed, fabricated, instrumented, and tested in the Iowa State University Structural Engineering Laboratory. Six of these specimens (jointed specimens) were designed with a joint that replicated the specific Little Silver Creek Bridge detail. (Three of the specimens were constructed using Ductal UHPC, and three specimens were constructed using Korean-UHPC (K-UHPC)). In addition, three specimens were designed and fabricated without a connection and consisted of a single, continuous deck panel. These three specimens were intended to serve as a baseline to which the behavior of the jointed specimens could be compared.

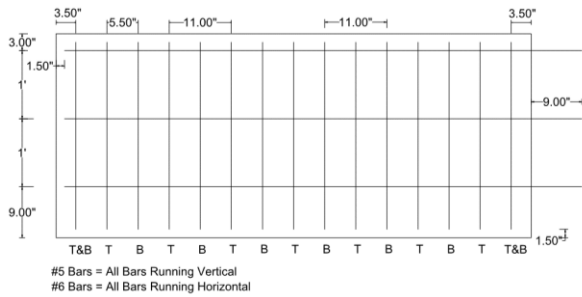
Each of the jointed specimens had two deck panels with a width of 7 ft, a length of 3 ft, a depth of 8 in., and a 10 in. wide UHPC longitudinal connection between the two deck panels. The jointless specimens had the same overall geometry as the jointed specimens, minus the joint. Details for the reinforcement and cross-sections were determined based on the details from two adjacent modules (Figure 5) matching the exact layout specified in the bridge plans.

The cross-sections and reinforcement details of the jointed specimens are shown in Figure 6.

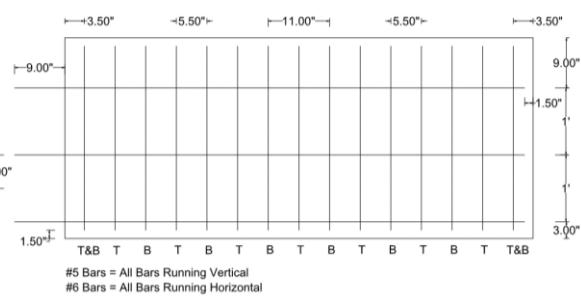


(a) Cross-section - left deck panel

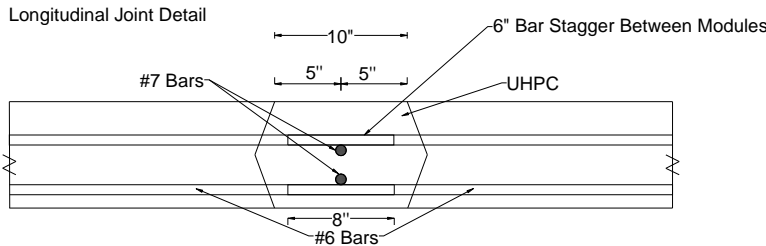
(b) Cross-section - right deck panel



(c) Rebar layout - left deck panel



(d) Rebar layout - right deck panel



(e) UHPC connection detail

**Figure 6. Details of jointed specimens**

As shown in Figure 6(a) and Figure 6(b), a clear cover of 2.625 in. and 1 in. was used for the top and bottom steel bars, respectively. As shown in Figure 6(a) through Figure 6(d), the longitudinal bars were #5 bars spaced at 11 in. and the transverse bars were #6 bars spaced at 1 ft. The top and bottom longitudinal bars were staggered at a distance of 5.5 in. And the transverse bars of the two deck panels were staggered panel-to-panel at a distance of 6 in., fitting into the deck joint connection shown in Figure 6(c) and Figure 6(d). All #6 bars projected 9 in. into the 10 in. UHPC connection with an overlap length of 8 in., as shown in Figure 6(e). Two #7 bars were also placed in the center of the connection above and below the #6 bars, as shown in Figure 6(e).

The only other difference between the six jointed specimens, besides the joint material, was the surface preparation in the joint. All of the joints were textured, but the joint surface preparation technique varied for each. The textured surface was specified by the Iowa DOT to be a minimum concrete surface profile (CSP) 6. Three types of surface preparation techniques were utilized to texture the joint surface of the three jointed specimens (two types of form liners, known as: rubber sandblast medium and plastic sandblast, and a form retarder). The rubber form liner was

product #121 Sandblast #3 provided by Scott System, Inc. The plastic form liner was product #8001 Sandblast Medium provided by Custom Rock Form liner.

There were two different types of form-retarders to choose from: a paint-like material that is applied directly to the forms or a sprayable liquid that is applied on freshly placed concrete. The paint-like material was selected for this project.

After the concrete had cured and the forms were removed, the surface with the form-retarder was power-washed to produce an exposed aggregate finish. Each of the three surface conditions were used once each for both the Ductal-UHPC and the K-UHPC specimens. The different techniques were evaluated to determine the performance and feasibility of use with large-scale construction.

The three surface treatments considered in this work met the designer’s criteria of achieving a specified CSP level. As will be seen, since the loads considered in this work were much higher than the strength limit loads considered for design, the surface treatments selected didn’t provide an interface bond higher than the concrete tensile capacity.

For comparison purposes, three specimens without a connection consisting of a single deck panel were also evaluated. These jointless specimens are, as much as anything, a “normal” baseline with which the jointed test results could be compared. Each specimen had a width of 14 ft-10 in., a length of 3 ft, and a depth of 8 in. The configuration of these specimens were established to best represent a standard bridge deck with the same amount of reinforcement as the jointed specimens, as shown in Figure 7.

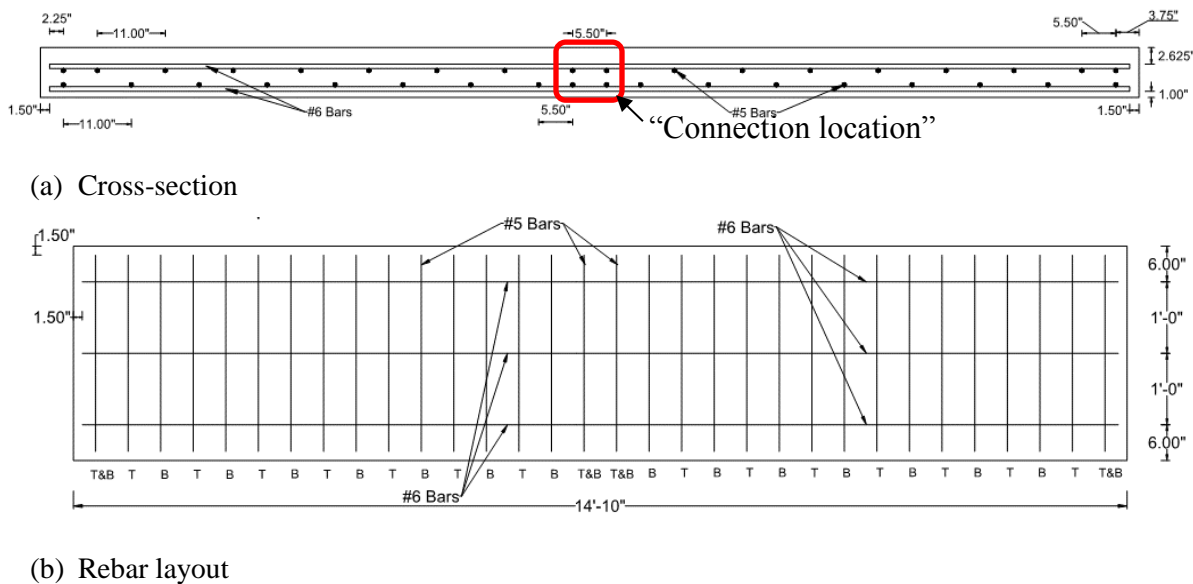


**Figure 7. Details of jointless specimens**

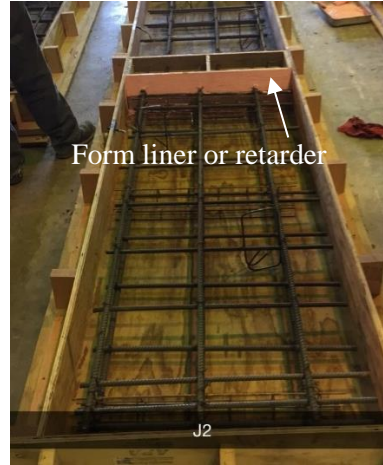
Note that all of the reinforcing steel bars had the same covers and spacing. To represent the reinforcing steel bar layout in a standard bridge deck, the #6 bars ran the continuous width of the

specimen with no overlap. The #6 bars were spaced at 1 ft with 6 in. to the edge of the specimen and the #5 bars were evenly spaced at 11 in across the whole deck panel with 3.75 in. of clear distance to the edges, as shown in Figure 7(b). Four #5 bars at a spacing of 5.5 in. were designed at the “connection location,” as shown in Figure 7(a).

The specimens were fabricated in the Structural Engineering Laboratory at Iowa State University. All three of the jointless specimens were fabricated first, followed by the three jointed Ductal-UHPC specimens, and finally the three jointed K-UHPC specimens. The specimens all followed the same fabrication process shown in Figure 8.



(a) Formwork and rebar–jointless specimen



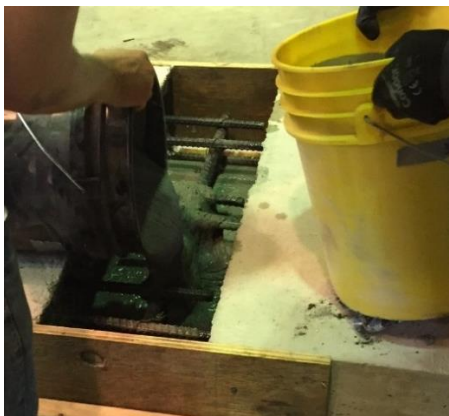
(b) Formwork and rebar–jointed specimen



(c) Placement of normal-strength concrete



(d) Finish of normal-strength concrete



(e) Placement of UHPC



(f) Finish of UHPC

**Figure 8. Fabrication sequence of jointless and jointed longitudinal connection specimens**

All of the bars were laid out and marked according to the specimen details. After everything was in the proper location, the bars were tied together to form the specified mats. The specimen formwork was constructed using normal plywood. Plywood sheets were laid down and marked to the designed dimensions.

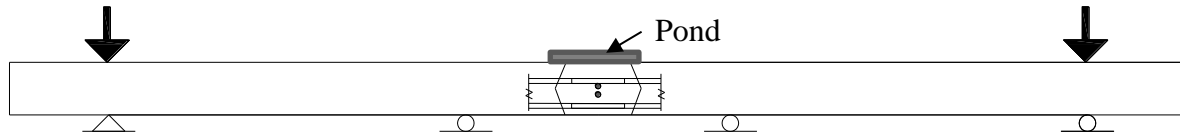
Before placing the steel reinforcing mats into the forms, uniaxial strain gauges were installed on the transverse bars near the joint location. The steel bars were installed and placed into the formwork as shown in Figure 8(a) and Figure 8(b). The form liner or retarder was then applied to the formwork at the connection interface as shown in Figure 8(b). The placement and surface finish of the concrete for the deck panels are as shown in Figure 8(c) and Figure 8(d), respectively.

After 28 days, the two deck panels of each jointed specimen were properly oriented, the connection formed, and the UHPC placed into the formwork as shown in Figure 8(e). The finished UHPC connection is shown in Figure 8(f). The jointless specimens were tested after 28-day curing and the 28-day compressive strength of the normal-strength concrete was measured to be 5.2 ksi.

Testing for the jointed specimens was able to start as soon as the compressive strength of the UHPC reached 15 ksi, but no sooner than four days as four days is the minimum cure time specified by the Iowa DOT. The ductal UHPC jointed specimens were tested after a 6-day cure of the UHPC, which had a measured 6-day compressive strength of 18.2 ksi. The average compressive strength of the K-UHPC after a 6-day cure was measured at 15.7 ksi, and the testing of the K-UHPC jointed specimens began the following day.

#### *Curing and Ponding Tests*

Ponding tests for a Ductal-UHPC and a K-UHPC jointed specimen were conducted to check if the UHPC connection developed cracks during curing. During the placement and curing of the UHPC pour, vertical restraining forces (as shown in Figure 9(a)) were applied at the specimen ends to simulate the transverse restraint provided by the girders.



(a) Test setup of curing and ponding tests



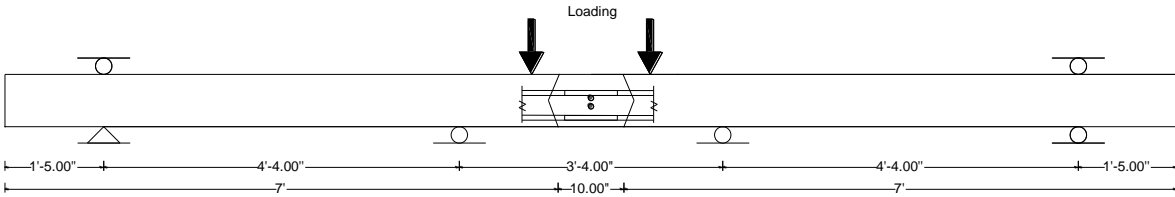
(b) Enclosure for ponding test

**Figure 9. Jointed specimen curing and ponding tests**

The test setups were determined based on the bridge details shown previously in Figure 2. During the curing process, the interface between the UHPC and the normal concrete were visually observed to record any crack formation. At the 5th day after UHPC placement, a pond was formed on the top of the connection for 6 hours to check if any leakage occurred at the connection and interface, as shown in Figure 9(a). To form the pond, a 3 in. tall watertight wall was constructed all the way around the joint as shown in Figure 9(b). About 1 in. of water was placed in the pond (following the Iowa DOT specified procedures). This experimental ponding regimen followed the ponding regimen specified for construction of the actual bridge.

### *Strength Tests*

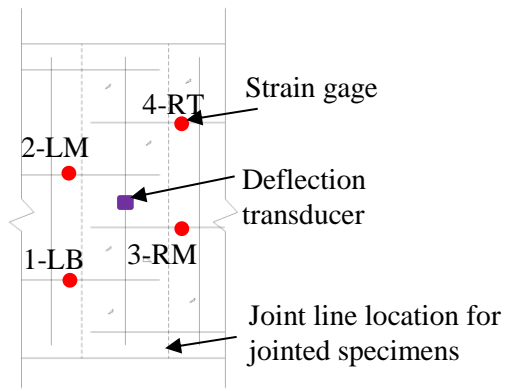
Strength tests were conducted to check if the jointed specimens had the same strength as that of the jointless specimens. All specimens were tested utilizing the same loading and boundary conditions shown in Figure 10(a) and Figure 10(b).



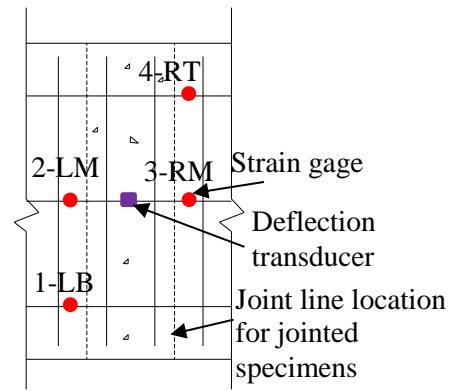
(a) Test setup of strength tests



(b) Continuous strength testing setup



(c) Instrumentation of jointed specimens



(d) Instrumentation of jointless specimens

**Figure 10. Longitudinal connection strength tests and instrumentation**

Each specimen was supported in a manner that simulates the girders in each adjacent precast unit. The center span was 3 ft-4 in. long and the two outside spans were 4 ft-4 in. long, replicating the planned girder spacing. The supports ran the entire length of the specimen.

For each jointed specimen, four strain gauges were installed on the bottom layer of reinforcing bars and embedded 2 in. from the outermost line of the connection interface before concrete placement (see Figure 10(c)). A deflection transducer was installed on the bottom of the specimen at the mid-center span (see Figure 10(c)). For each jointless specimen, the instrumentation layouts were the same as the jointed specimens, as shown in Figure 10(d).

Two-line loads were applied to the jointed specimen 3.5 in. from the outermost interface surface. The same loading approach was used for the jointless specimens. The loads were continuously applied on the specimens by two hydraulic actuators, each fitted with load cells to record the applied loading. Visual crack mapping techniques were utilized to monitor and document crack formation in the deck panels, joint material, and interfaces during loading. Loading of each specimen was stopped and the cracks of each specimen were marked approximately every 50 kips, until the steel yielded. The loading continued until it was decided that each specimen had failed.

## Test Results and Discussions for Longitudinal Connections

### *Curing and Ponding Tests*

During curing of the UHPC, no cracks were found at the interface between the UHPC (either K-UHPC or Ductal-UHPC) and the HPC. During the ponding test, no leakage was found at the two sides and bottom of the connection, as shown in Figure 11.

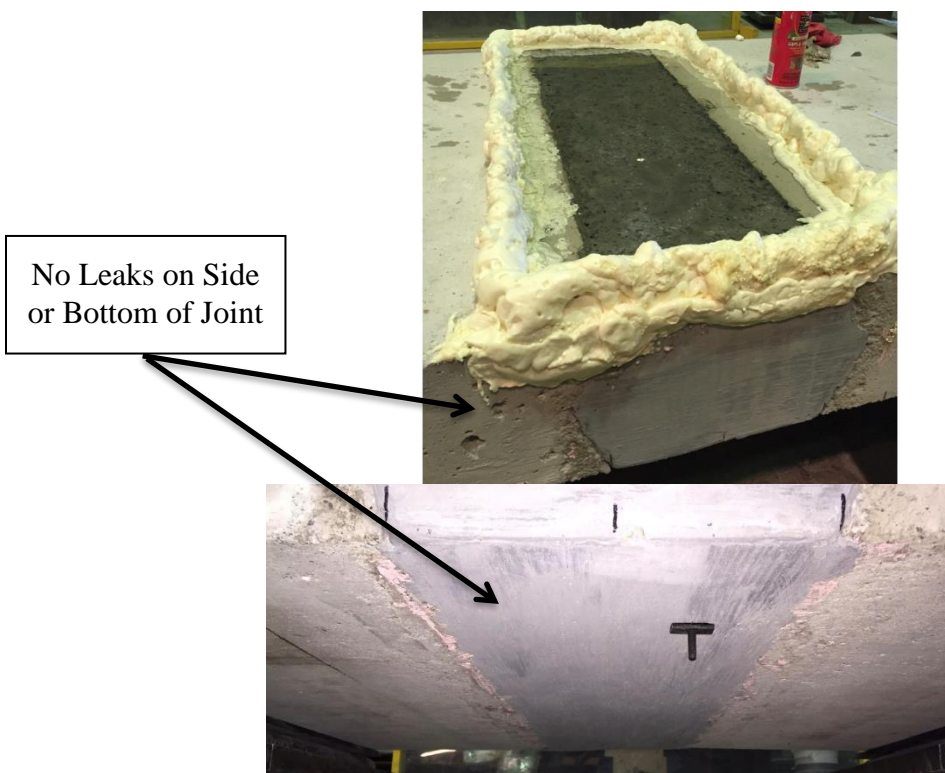


**Figure 11. Examination of ponding test**

As a result, it was concluded that a good bond was achieved at the interface between the concrete and UHPC and the deformation due to early-age drying shrinkage and temperature change did not cause any cracks in the connection and interface.

### *Crack and Failure Patterns*

Crack mapping was used during all tests to track crack initiation and crack growth patterns. The loading on each specimen was stopped and cracks were marked at approximately every 50 kips until it was no longer safe to be close to the test apparatus. Cracking for all of the specimens originated in the negative moment region over the two interior supports, as shown in Figure 12.

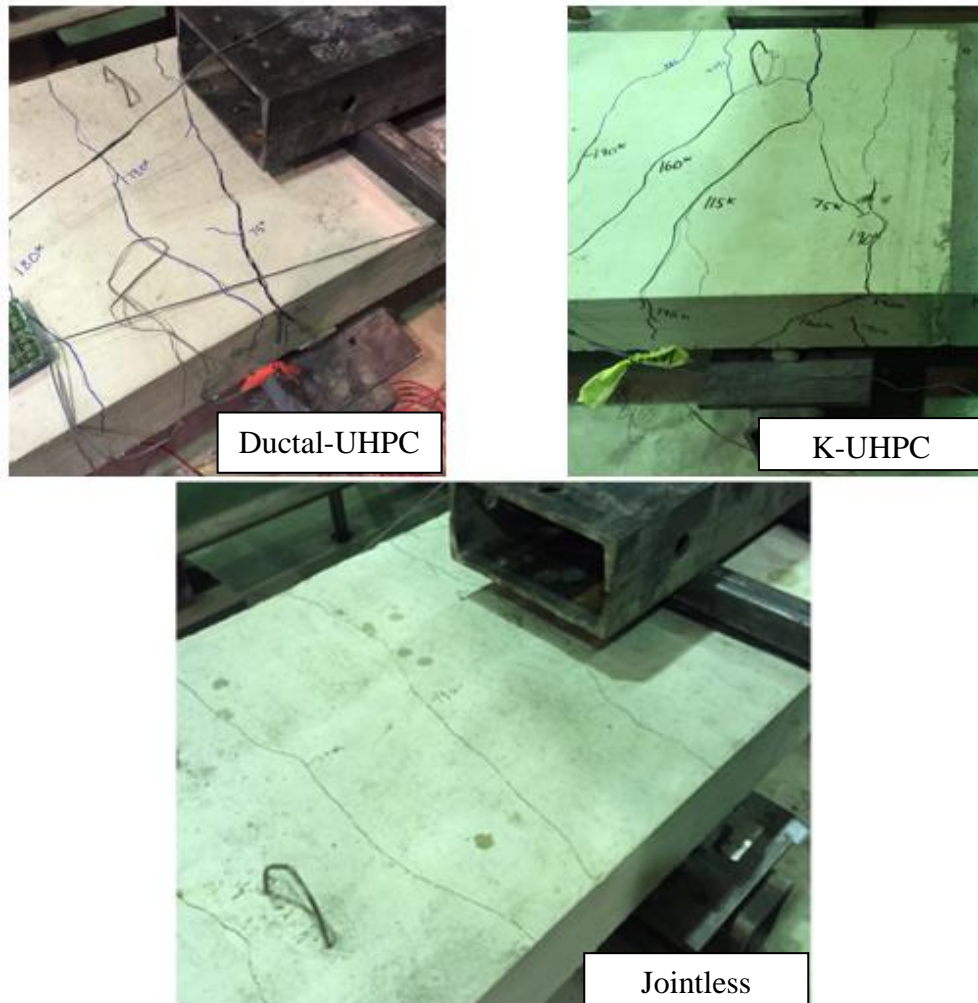


**Figure 12. Crack patterns**

The first cracks ran continuously over the entire length of the specimens. Then, cracks were found at the first and third spans, and some of the initial cracks become noticeably wider. Around this time, cracking was also observed on the bottom and side surfaces of the specimen between the two interior supports and at the joint interface, as shown in Figure 13.

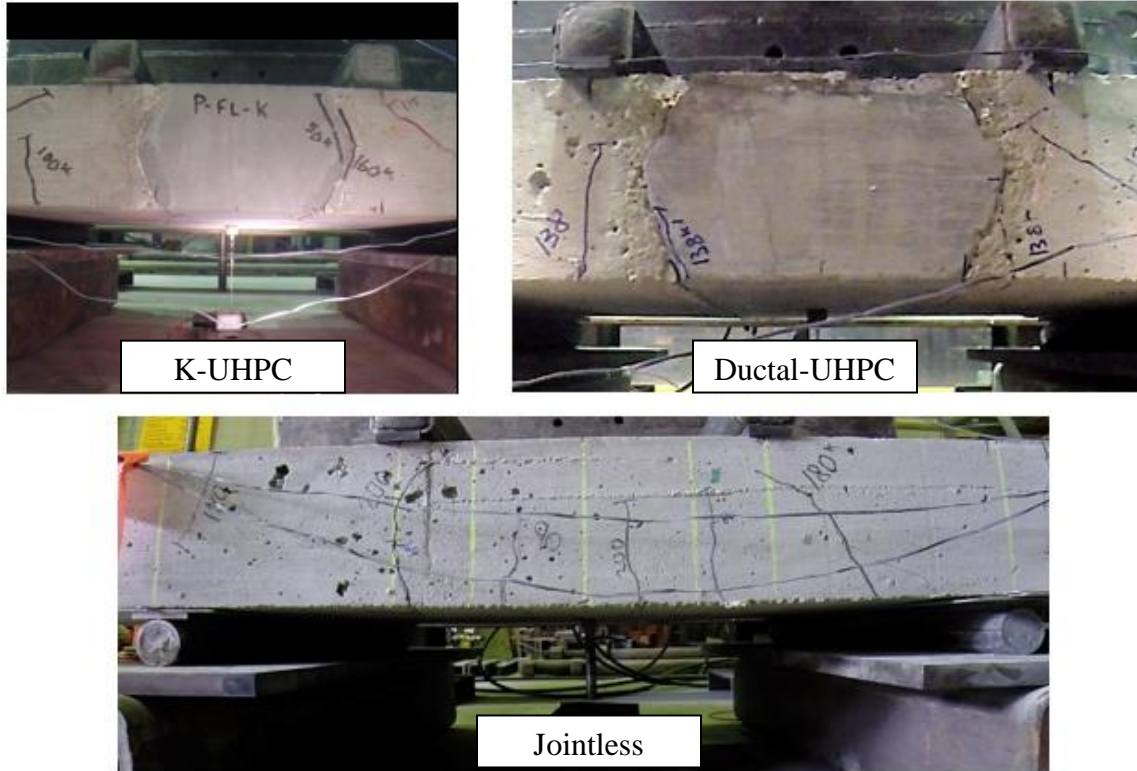


**Figure 13. Flexural cracking**

Near the time that the steel yielded, vertical flexural cracks became visible on the sides of the specimens. As shown in Figure 13, significantly more flexural cracks formed on the jointless specimens than both types of jointed specimens. Following the yielding of the steel bars, cracking started to form diagonally from the loading line to the interior supports. No crack was found in the joint materials (i.e., K-UHPC and Ductal-UHPC). In general, all specimens had a similar crack pattern.

At failure of each specimen, the specimens were subjected to a flexural-shear failure that included abrupt crushing of the top surface of the concrete deck and large diagonal cracking as shown in Figure 14.

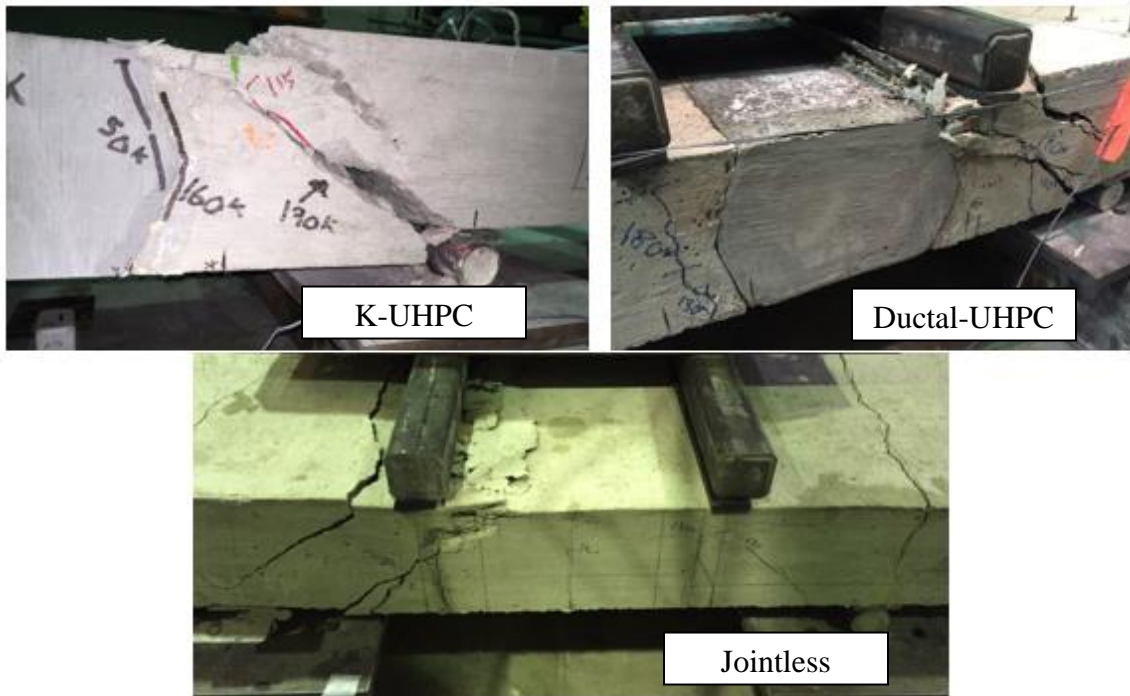


**Figure 14. Failure cracks**

The angle of the major diagonal cracks for each specimen was approximately 35 degrees. In general, all specimens had a similar failure pattern.

Both types of joint materials maintained a solid connection to the modules. After testing was finalized, the specimens were taken apart to examine the bond between the bars and the joint as shown in Figure 15.



**Figure 15. Longitudinal connection joint investigation**

There was no observed slip between the reinforcing steel and the joint, and no fracture was observed in the bar.

### *Comparison of Surface Preparation Techniques*

The three joint surface preparation techniques produced slightly different CSPs. The form-retarder produced the roughest surface profile, followed by the rubber form liner, and then the plastic form liner, which produced the smoothest surface, as shown in Figure 16.

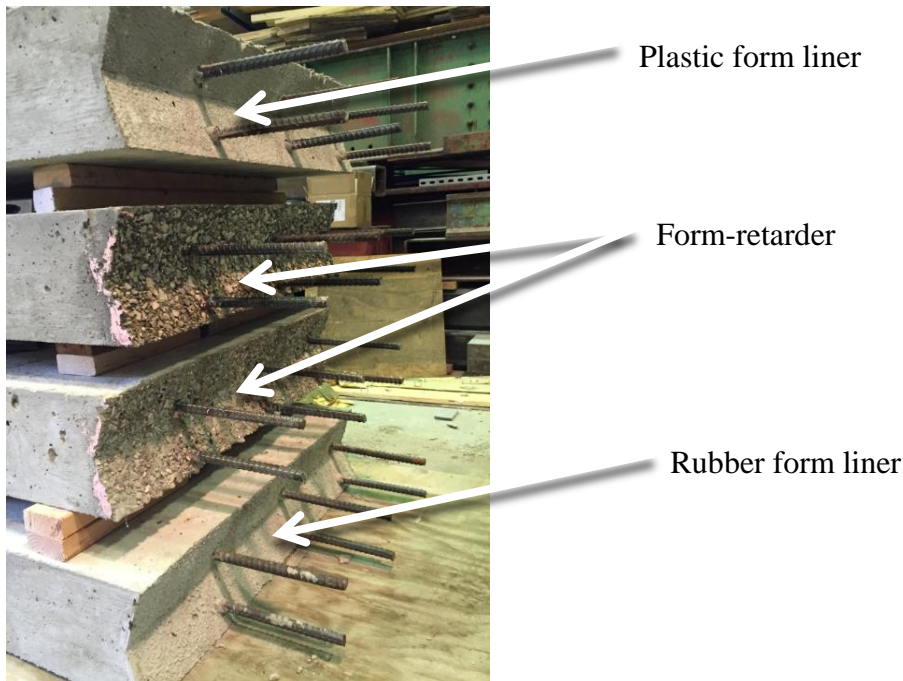


**Figure 16. Comparison of longitudinal connection joint surfaces**

The exposed aggregate surface was noticeably different between the specimens using the form liners and form-retarder as shown in Figure 16. The goal of using three different techniques was to select the best method to achieve the desired CSP.

Applying the form-retarder was the easiest to construct method evaluated in this project. It was fairly simple to paint on; however, some spots were difficult to reach because of the layout of the reinforcing steel mats.

After the forms were removed, the specimens were lifted outside the laboratory using a forklift. Once outside, the forms were power-washed to remove the chemical compound and provide the exposed aggregate finish. The rubber and plastic form liners were very similar in terms of constructability. Cutting and attaching the form liners to the joint forms was a fairly simple and quick task.

*Load, Strains, and Deflections*

Load-strain relationships were developed for each of the specimens and are shown in Figure 17 through Figure 26.

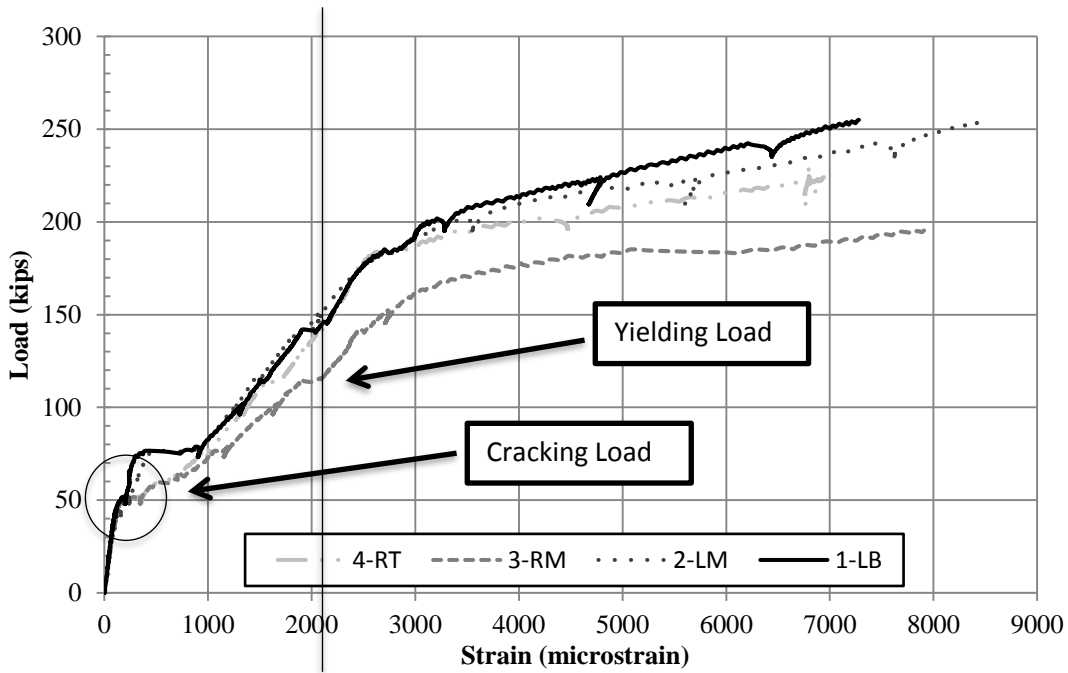


**Figure 17. Load vs. strain - jointless Specimen C1 (1st Test)**

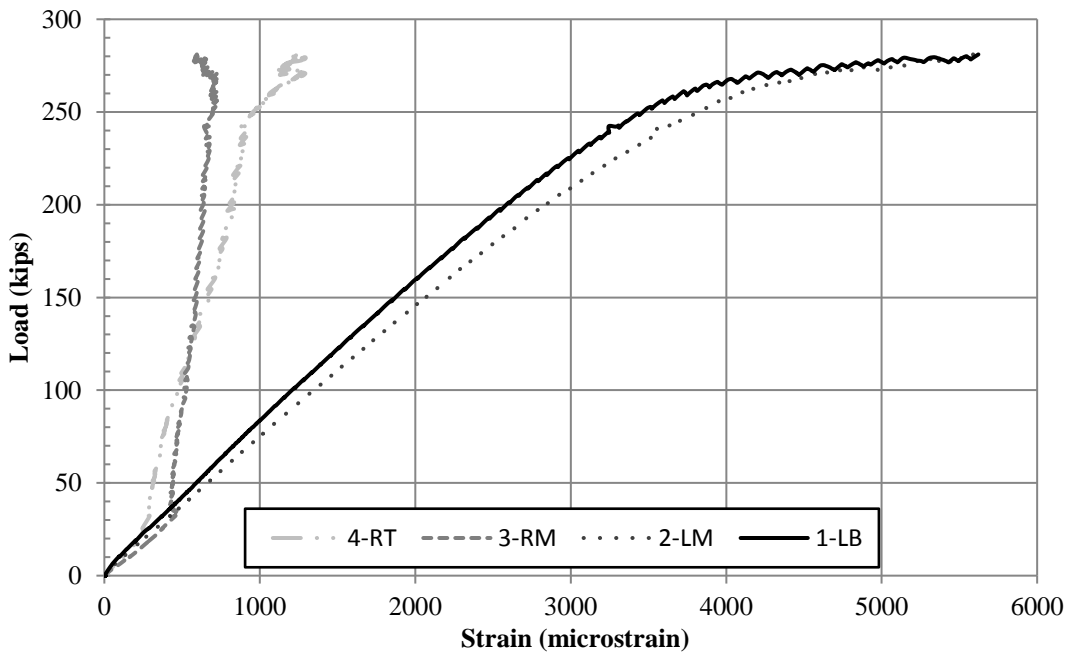


**Figure 18. Load vs. strain - jointless Specimen C1 (2nd Test)**

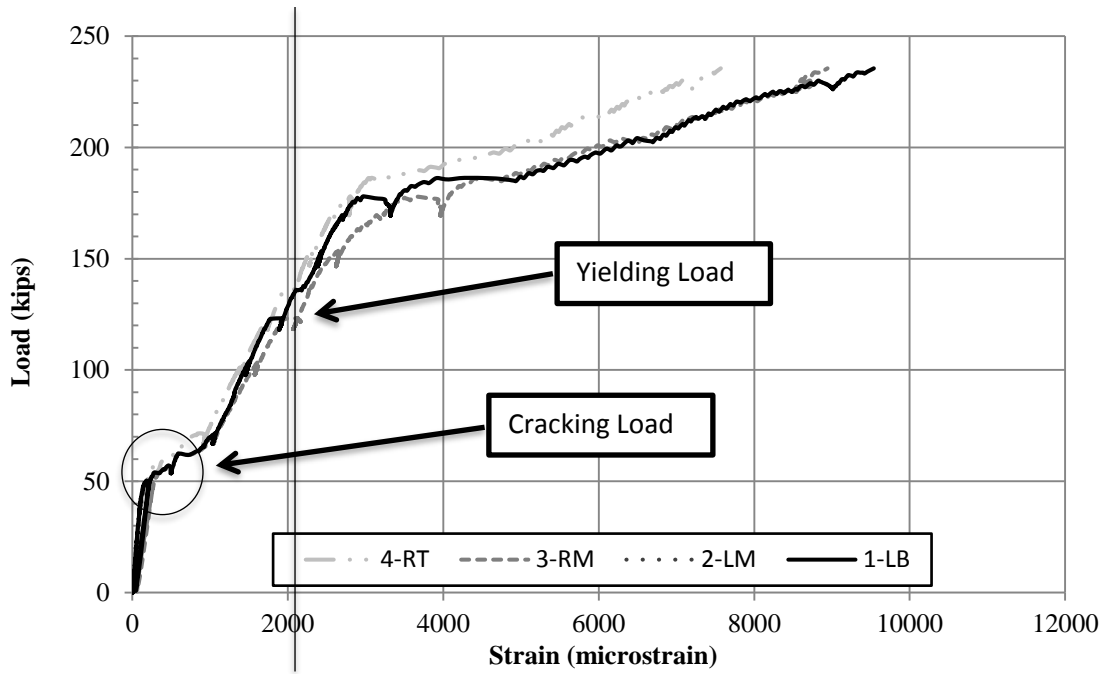


**Figure 19. Load vs. strain - jointless Specimen C2**

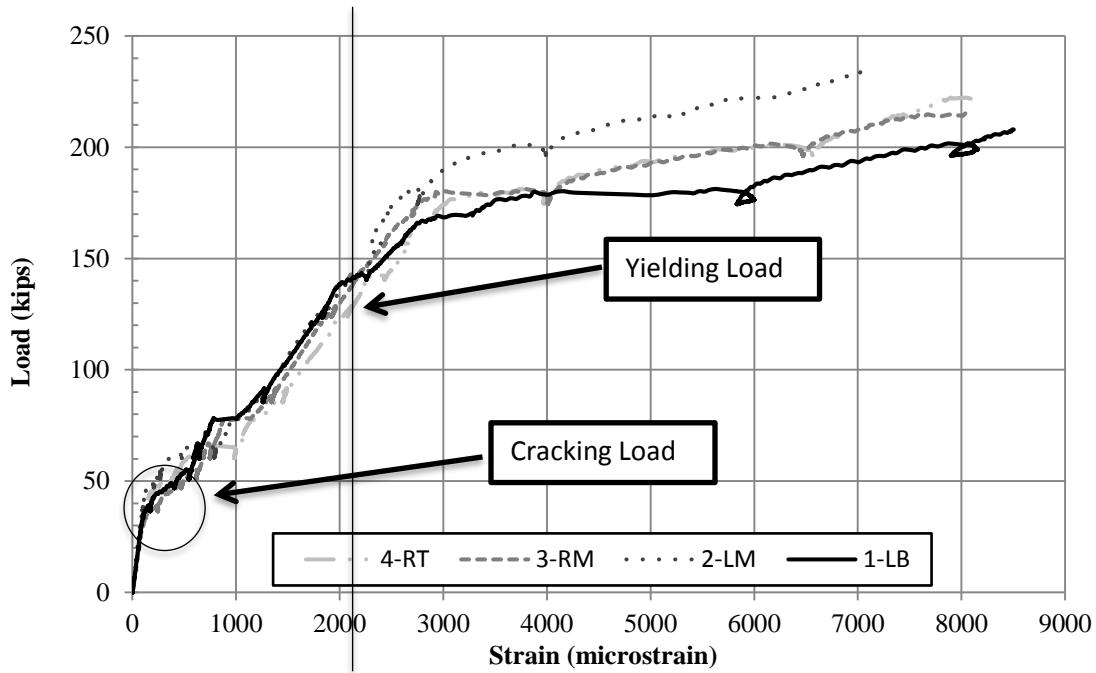


**Figure 20. Load vs. strain - jointless Specimen C3**

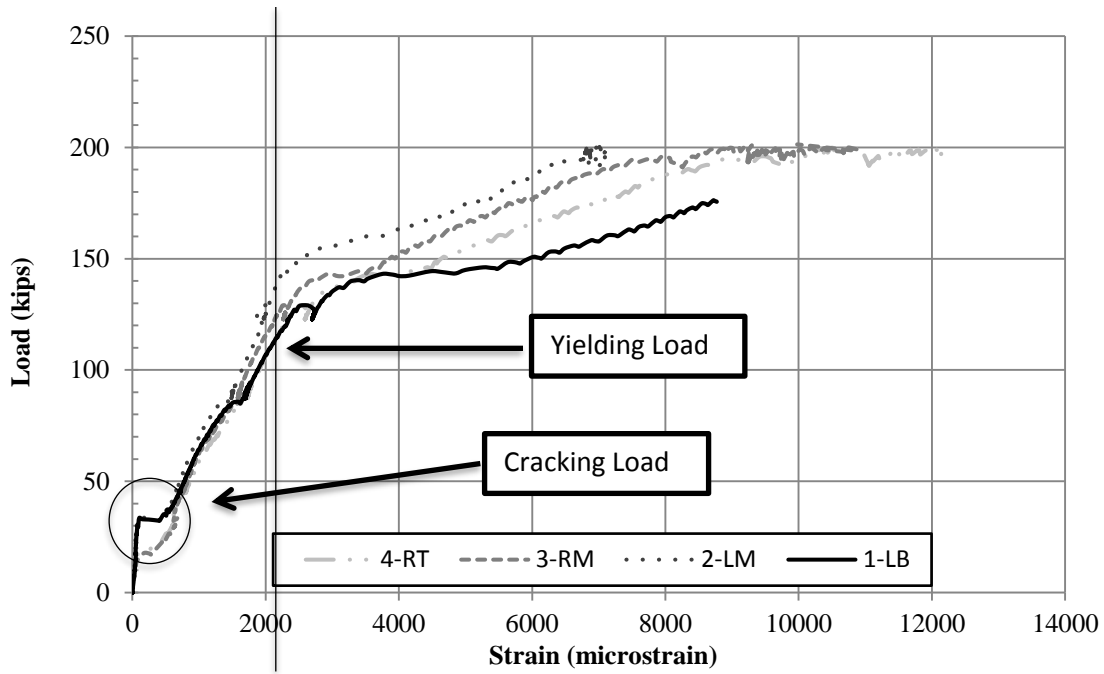


**Figure 21. Load vs. strain - Specimen J1 (Plastic Form Liner-UHPC)**

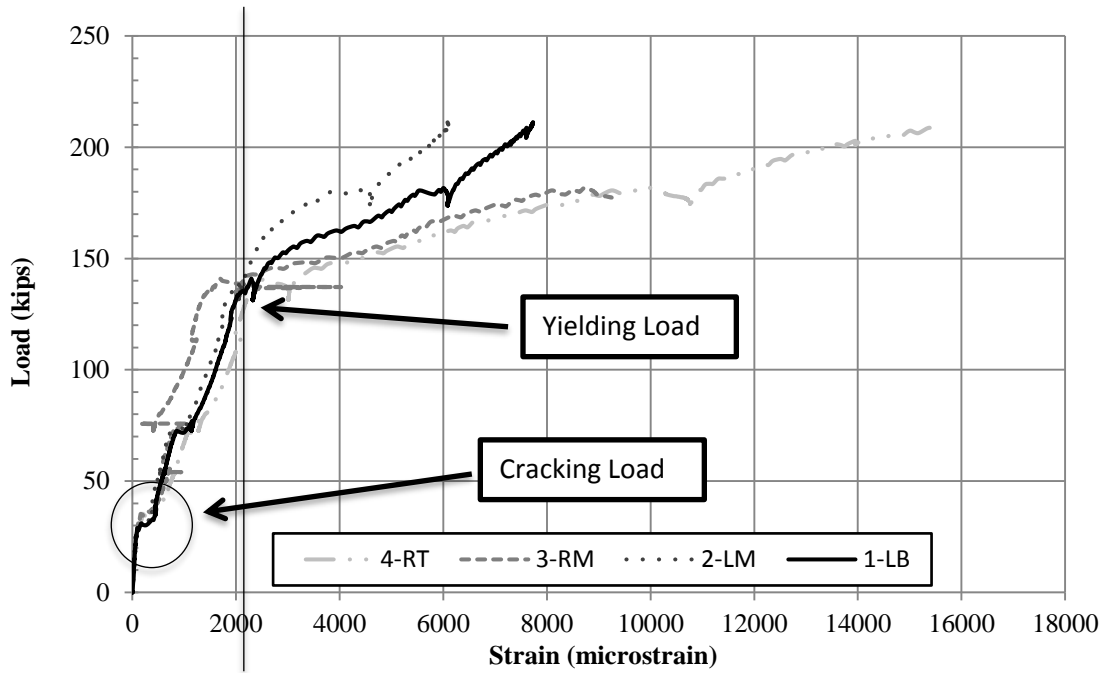


**Figure 22. Load vs. strain - Specimen J2 (Form-Retarder-UHPC)**

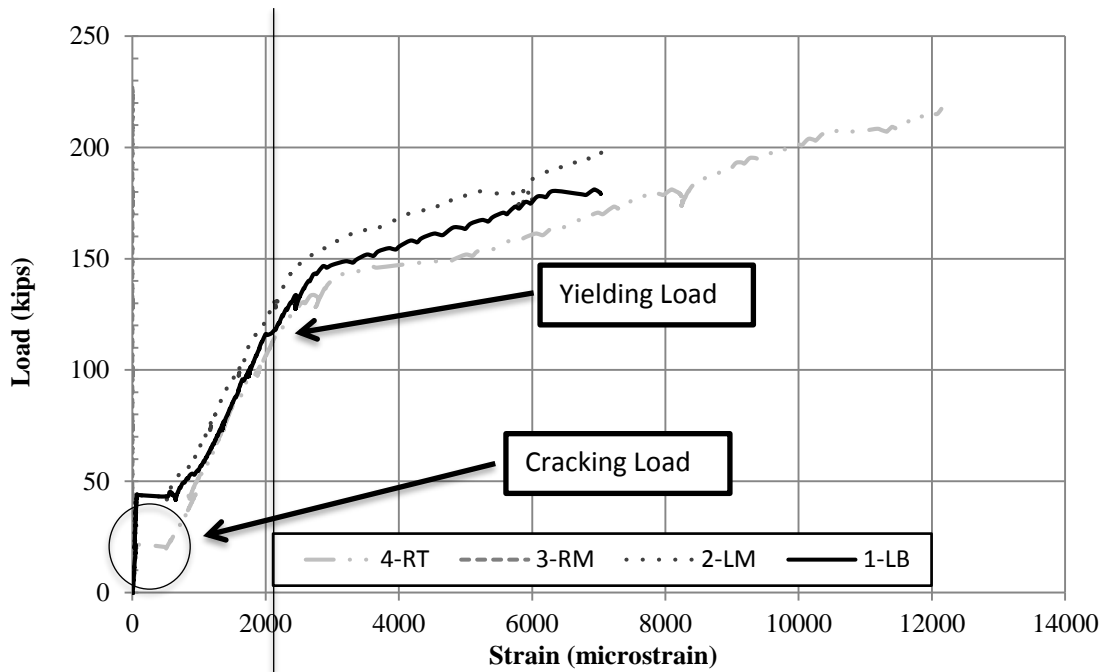


**Figure 23. Load vs. strain - Specimen J4 (Rubber Form Liner-UHPC)**

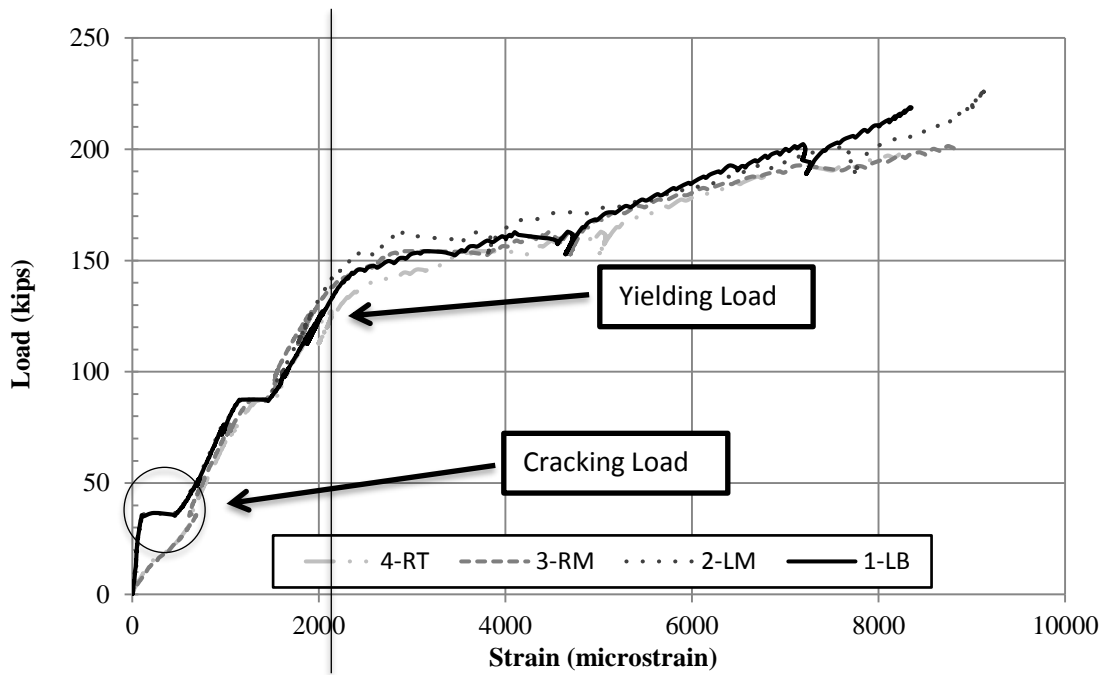


**Figure 24. Load vs. strain - Specimen K1 (Form-Retarder-K-UHPC)**

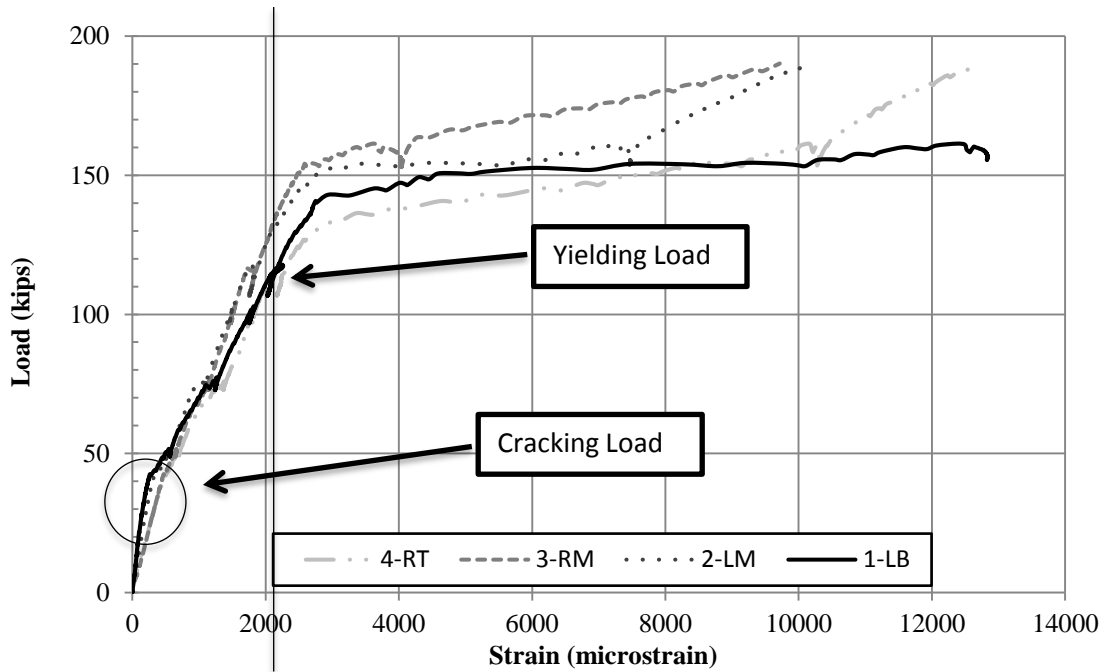


**Figure 25. Load vs. strain - Specimen K2 (Plastic Form Liner-K-UHPC)**

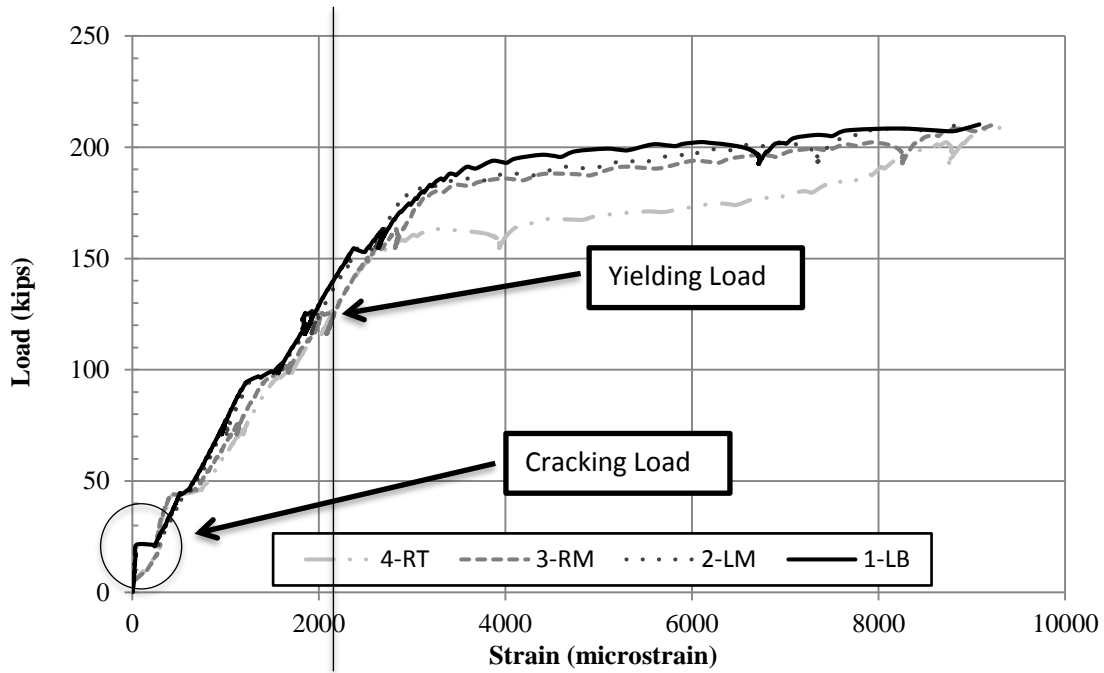


**Figure 26. Load vs. strain - Specimen K3 (Rubber Form Liner-K-UHPC)**

Locations of the embedded gauges used for the figures were illustrated previously in Figure 10(c) and Figure 10(d). Through the developed relationships, it was possible to determine several characteristics of the specimens including the cracking load, steel yielding load, and failure load.

The cracking load was estimated based on the load-strain relationships of the embedded strain gauges. The first point the strain value reached a plateau (an abrupt increase in strain) was recorded as the cracking load. For locations where the initial plateau was not as evident, the cracking load was determined once the first steel reinforcement in the deck reached a strain value equal to that of tensile cracking of concrete, which corresponds to about 135 micro-strains based on a linear stress-strain curve.

Given that the embedded strain gauges were very close to the surface of the deck, the results produced from strain gauge readings are assumed to closely represent the strain values seen on the deck surface. As for the yielding load, Grade 60 reinforcing steel was used for this project, which has a theoretical yield strain of 2,069 microstrain. The load at which the average strain in the cross section exceeded this limit was recorded as the yielding load of steel reinforcement. The maximum load that was reached prior to failure was recorded as the failure load. Values for the cracking load, yielding load, and failure load are clearly illustrated for each specimen in Figure 17 through Figure 26.

The results from all of the load-strain relationships were summarized and are shown in Table 1.

**Table 1. Summary of all test results**

Type of Specimens		Joint Surface Preparation Technique	Load at Concrete Cracking (kips)	Load at Steel Yield (kips)	Load at Specimen Failure (kips)	Deflection at Failure Load (in.)
			Measured	Measured	Measured	Measured
Jointless specimens	C1	N/A	52	115	250	0.37
	C2	N/A	56	123	235	0.42
	C3	N/A	39	126	230	0.39
Jointed specimens (Ductal-UHPC)	Form-Retarder		31	114	210	0.38
	Plastic Form Liner		34	110	195	---
	Rubber Form Liner		20	112	225	0.39
Jointed specimens (K-UHPC)	Form-Retarder		35	125	228	---
	Plastic Form Liner		39	114	190	0.33
	Rubber Form Liner		22	125	210	0.29

N/A = not applicable, --- = bad data

These relationships were used to make several different comparisons between all of the specimens. Overall, the results showed a large deviation in the cracking load between the three types of specimens.

The continuous specimens had a significantly higher load prior to cracking than the jointed specimens. It was also quite varied depending on which surface preparation technique was

utilized. In general, the plastic form liner resulted the highest crack load, then the form retarder, and then the rubber form liner.

The pattern for the yielding load was not as distinct; however, the jointless and K-UHPC specimens were able to sustain slightly higher loads on average prior to yielding than the Ductal-UHPC specimens. The specimens using the plastic form liner had the lowest yielding load for both types of joint material. The failure loads of the specimens followed a very similar pattern as the yielding loads. The jointless specimens were measured to be stronger than the jointed specimens, and, once again, sustained higher loads prior to failure. As far as the jointed specimens, the rubber form liner and the form-retarder outperformed the plastic form liner for ultimate strength.

Also of interest for this testing was which joint surface preparation method performed best. Generally, each preparation technique was used twice. The performance of each technique was determined based on the results from the strength tests and overall constructability including time and labor cost. The results from the strength tests for each technique are summarized in Table 2.

**Table 2. Test results for each surface preparation technique**

Joint Surface Preparation Technique		Load at Concrete Cracking (kips)		Load at Steel Yield (kips)		Load at Specimen Failure (kips)		Deflection at Maximum Load (in.)	
		Measured	Average	Measured	Average	Measured	Average	Measured	Average
Form-Retarder	Ductal UHPC	31	33	114	119.5	210	219	0.38	0.38
	K-UHPC	35		125		228		---	
Plastic Form Liner	Ductal UHPC	34	36.5	110	112	195	192.5	---	0.33
	K-UHPC	39		114		190		0.33	
Rubber Form Liner	Ductal UHPC	20	21	112	118.5	225	217.5	0.39	0.34
	K-UHPC	22		125		210		0.29	

--- = bad data

As shown in Table 2, the cracking loads for the three techniques were very inconsistent. The plastic form liner produced the most favorable results and was able to withstand a load of 36.5 kips prior to cracking. The form-retarder was close behind with 33 kips; followed by the rubber form liner, which was only able to handle 21 kips before cracking.

Yielding loads were very comparable between the three techniques, all varying with just a few kips difference. It should be noted that the plastic form liner was the first to yield, despite the fact that the initial performance appeared to be superior to the other two techniques.

A similar pattern was followed for the failure load for each technique. The rubber form liner and the form-retarder performed the best and withstood just under 220 kips at the point of failure. The plastic form liner, on the other hand, fell just short of the 200 kip mark. The results for each technique were very comparable regardless of joint material.

The performance of each joint material was also analyzed. The results were rearranged to directly compare the effect of the joint material and are summarized in Table 3.

**Table 3. Summary of results by joint material**

Type of Jointed Specimens	Joint Surface Preparation Technique	Load at Concrete Cracking (kips)		Load at Steel Yield (kips)		Load at Specimen Failure (kips)		Deflection at Maximum Load (in.)	
		Measured	Average	Measured	Average	Measured	Average	Measured	Average
Ductal-UHPC specimens	Form-Retarder	31	28.3	114	112	210	210	0.38	0.385
	Plastic Form Liner	34		110		195		---	
	Rubber Form Liner	20		112		225		0.39	
K-UHPC specimens	Form-Retarder	35	32	125	121.3	228	209.3	---	0.31
	Plastic Form Liner	39		114		190		0.33	
	Rubber Form Liner	22		125		210		0.29	

Keep in mind that there were some discrepancies in the results between the joint construction techniques that were used. However, as mentioned before, the joint construction technique appeared to perform about the same for the two types of joint material. For this reason, the results can directly be compared.

As shown in Table 3, several tests were run and used to compare the different joint materials. A quick glance at the strength test results shows that the performance of the two materials was very similar. The average of the three specimens for each material cracked at around 30 kips and failed after a load of 210 kips was applied. Based solely on these results, one can conclude that either material would be suitable to use for the joints. However, another consideration taken into account was the constructability of the material; which the two mix designs varied on in that aspect.

Both of the mixes were created on site using the same drum mixer. The mix design for the Ductal-UHPC was provided by the Iowa DOT and is referenced as SP-120245a. All of the procedures outlined in the mix design were followed during the mixing process. The actual mixing of the material went very smoothly. Several 3 in. by 6 in. cylinders were cast during the placement of the UHPC to track the strength throughout the curing process. This was particularly important with the minimum strength requirements for the project. The results from the compression test are shown in Table 4.

**Table 4. Compressive strength test results for joint materials**

<b>Days</b>	<b>Ductal-UHPC (psi)</b>	<b>K-UHPC (psi)</b>
0	0	0
4	12,950	13,099
5	14,015	N/A
6	N/A	15,697
7	16,864	16,102
28	N/A	19,300

N/A = No data collected

The values listed in the table are the average strengths based on the three tests.

In preparation for the compressive strength testing, the cylinders were removed from the plastic molds and then saw cut to form smooth ends. Wood shims were also used during the testing in hopes to better distribute the load across the whole specimen and fill any void spaces. It was anticipated that the strength requirements would be achieved on Day 4. For this reason, as well as volume limitations of the mixer, only 9 cylinders were cast. Three cylinders were to be tested on Day 3, 4, and finally 28 days. As shown in the table, this was not plausible due to initially low strengths. The strength requirements were not reached until Day 7, which is when testing began.

The Korea Institute of Civil Engineering and Building Technology (KICT) provided the mix procedure for the K-UHPC. The mix procedure for the K-UHPC was very precise and required time step sequences to be followed. Even with close attention to detail, the first round of mixing was not a success. Everything appeared to be running smoothly until suddenly the material became very hard and appeared to lose all of its viscosity. Given that all of the proper procedures were followed, it was assumed that the volume produced from the mix quantities that were given was too large for the mixer to handle.

The second round of mixing was split into three separate batches. Only enough material to fill one specimen was mixed at a time. Everything went as planned for this round of mixing. Several 3 in. by 6 in. cylinders were cast for each of the three mixes. The average compressive strength between the three mixes was determined and is shown in Table 4. It should be noted that all three mixes produced very consistent strength results. The required 15 ksi strength of the K-UHPC was achieved in 6 days, but the specimens were tested on the 7th day to keep the cure times consistent.

Load deflection relationships were also produced from the deflection transducer that was attached to the bottom surface in the center of each specimen, as shown in Figure 27.

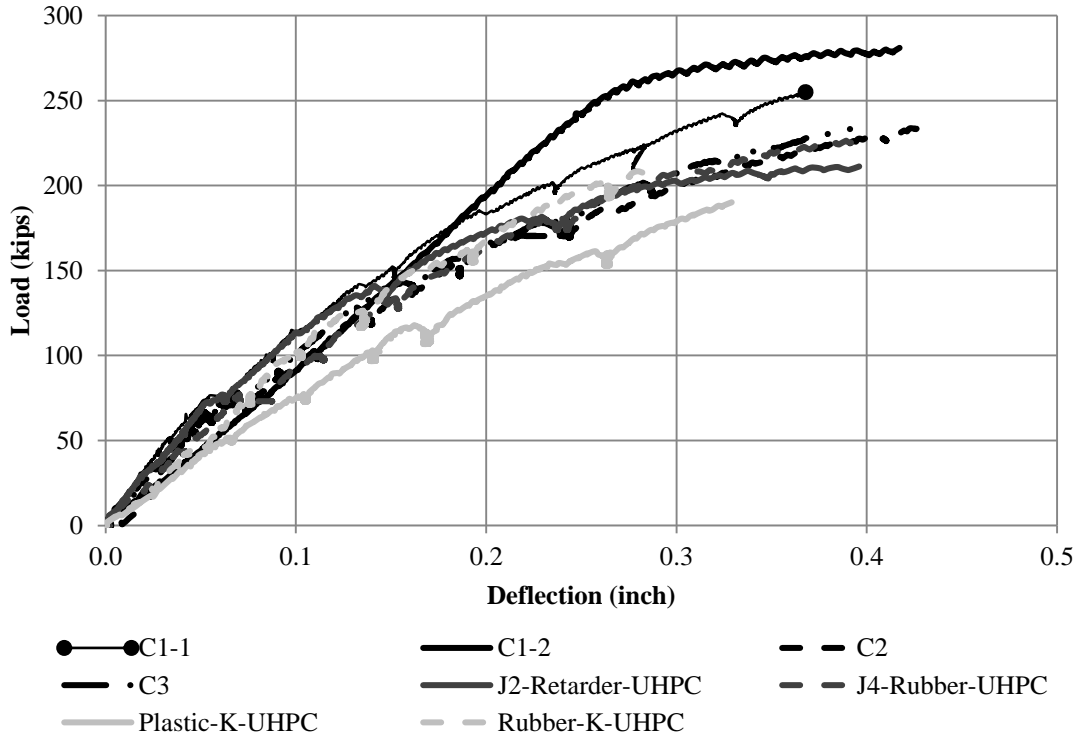


**Figure 27. Load vs. deflection for all Test A specimens**

Note the locations of the transducers are shown previously in Figure 10(c) and Figure 10(d). There was error in the instrumentation for two of the specimens. As a result, the data produced from Specimen J1 (Plastic Form Liner-UHPC) and K1 (Form-Retarder-K-UHPC) are not included. All results were very comparable. The deflections at failure for each specimen were shown previously in Table 1.

Some of the specimens carried additional load after failure, but the graph only shows deflection up until failure, to keep it consistent. Deflection of almost all specimens appeared to be just over 1/3 in. at the time of failure. This was the case for the continuous specimens as well as all of the jointed specimens. As shown previously in Table 3, the K-UHPC specimens produced smaller deflection results than the Ductal-UHPC ones. However, the results were very close and the difference was less than 1/10 in. It appeared the surface preparation technique had little effect on deflection, which is shown previously in Table 2.

### Laboratory Testing of Transverse Connections

An experimental program consisting of strength tests on transverse connections was designed and implemented to evaluate the behavior, strength, and failure modes of the HPC transverse connection of the Little Silver Creek Bridge and to understand the importance of including the somewhat complex compression block in future designs.

### Specimen Design and Fabrication

Two specimens were designed, fabricated, instrumented, and tested to evaluate the performance of the transverse joints with and without a compression block at the pier locations in the laboratory. The test specimens were also designed based on the actual details of the Little Silver Creek Bridge shown in Figure 28.

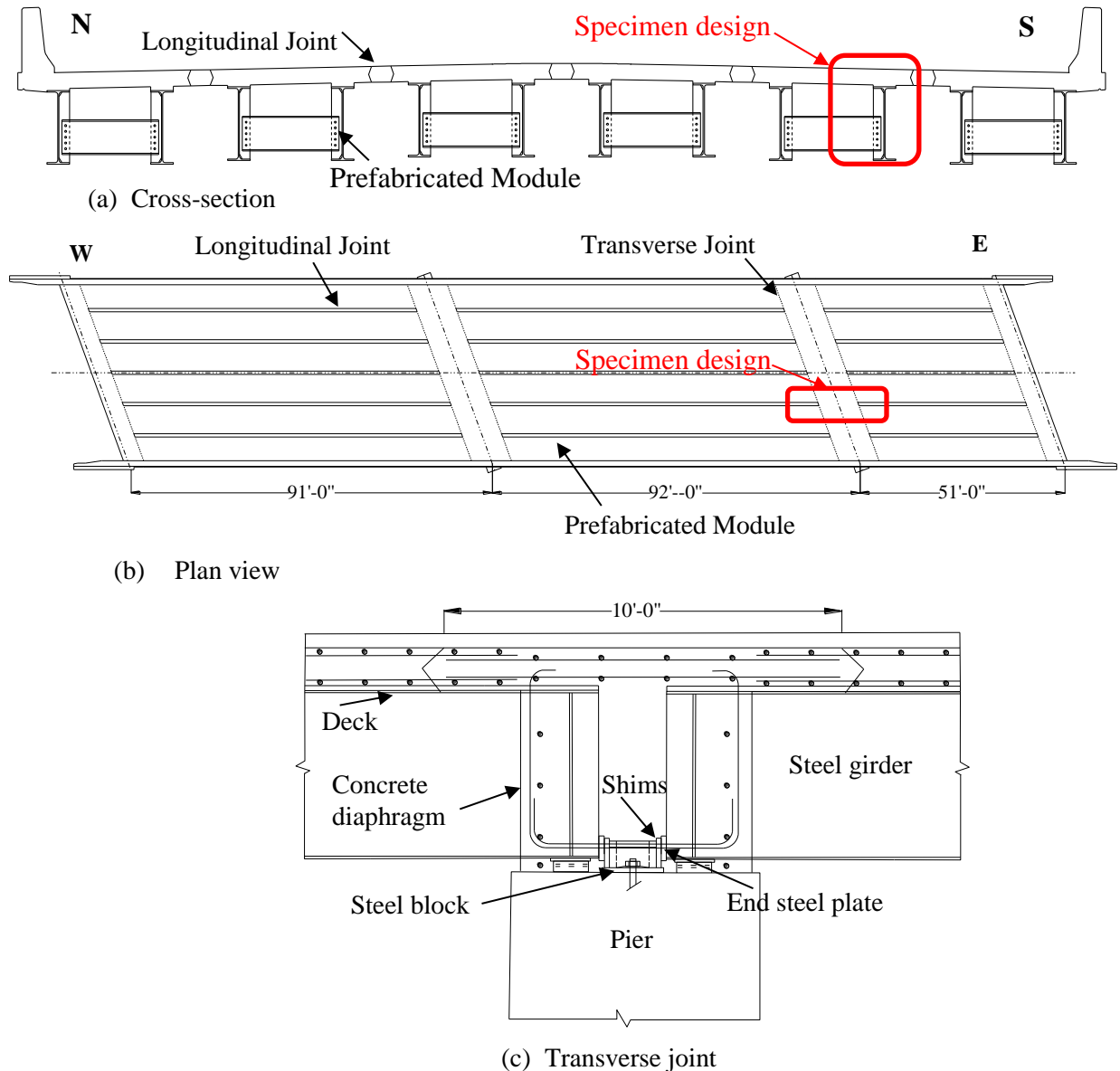
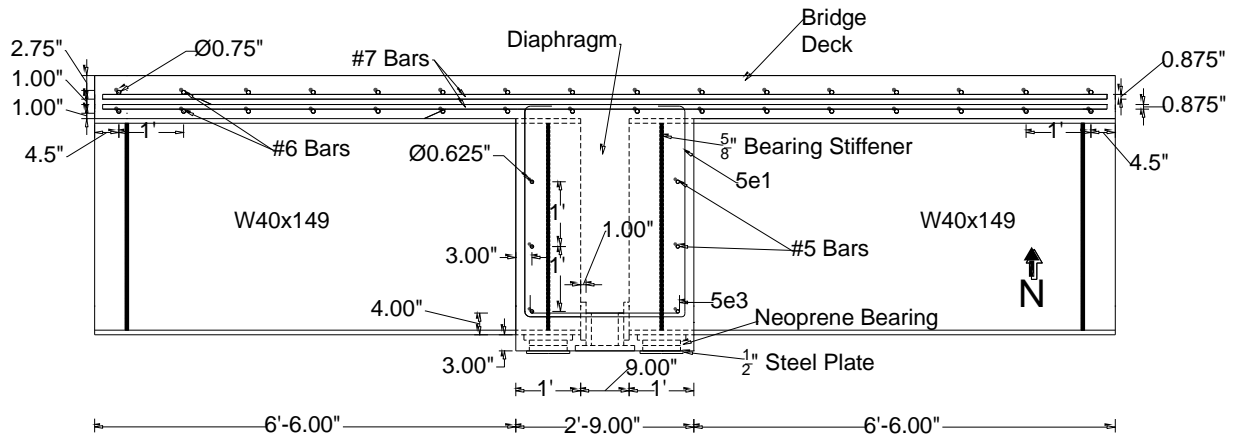
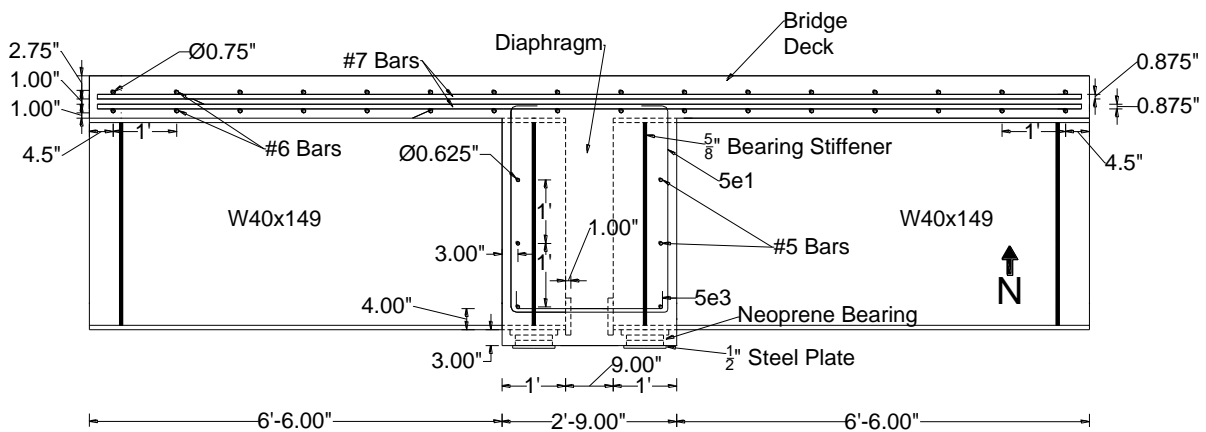


**Figure 28. Segment for design of transverse connections**

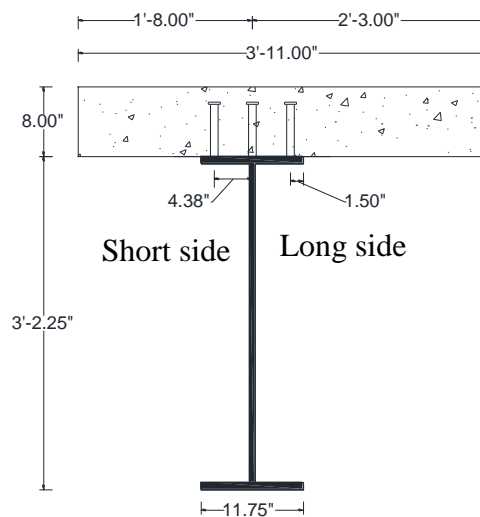
Note that the girders of each prefabricated module were spaced at 4 ft-6 in. and the adjacent girders between two modules were spaced at 3 ft-4 in. A specimen (referred to as Specimen I) was designed to exactly replicate the bridge details and included a compression block between the two longitudinally aligned girders as shown in Figure 29(a).



(a) Specimen I



(b) Specimen II



(c) Cross-section of composite beam

**Figure 29. Transverse joint specimen details**

Another specimen with no compression block (referred to as Specimen II) had the same design details as Specimen I minus the compression block and is shown in Figure 29(b). Each of the specimens consisted of two steel girders, a deck panel, and a concrete diaphragm, as shown in Figure 29. The steel girders had a W40x149 cross-section, a length of 7 ft-6 in, and a 9 in. longitudinal gap between them. Each girder had stiffeners on each side of the web over the support location as well as underneath the loading point, as shown in Figure 29. The girder top flange had shear studs with a length of 6 in. and a diameter of 7/8 in. The shear studs had longitudinal and transverse spacing of 8 in. and 4-3/8 in, respectively. The diaphragm had a length of 2 ft-9 in., a width of 3 ft-11 in., and a depth of 4 ft-1.5 in. The deck panel had a depth of 8 in. and a width the same as the diaphragm. Due to the uneven girder spacing, the steel girders were offset 3.5 in. from the deck centerline, resulting in one overhang being 7 in. wider than the other shown in Figure 29(c).

The longitudinal diaphragm reinforcement was placed through 1 in. drilled holes in the girder webs. A spacing of 3 in. was used from the face of the diaphragm to the inside edge of the reinforcement. There were 3 holes drilled on each side of the diaphragm. The first hole was drilled 4 in. above the bottom flange of the girder. 1 ft was used for the spacing between the next two reinforcing bars. These dimensions were duplicated for all 4 reinforcement locations between the two specimens and are shown in Figure 29(a) and Figure 29(b). #5 bars were used for the longitudinal reinforcement in the diaphragm and were 3 ft-8 in. long. A total of four #5 bars were used for shear reinforcement in each diaphragm and the bent bar details are shown in Figure 29(a) and Figure 29(b).

The deck panel of each specimen had two identical layers of steel reinforcement as shown in Figure 30.

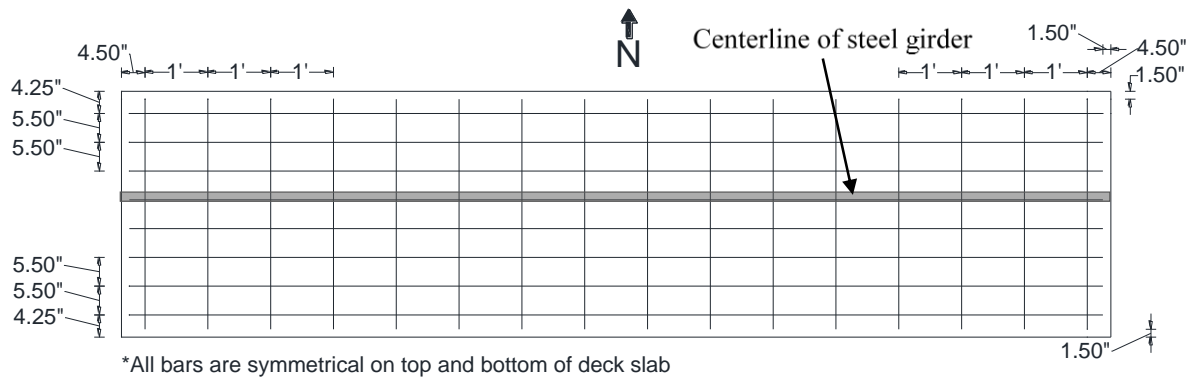
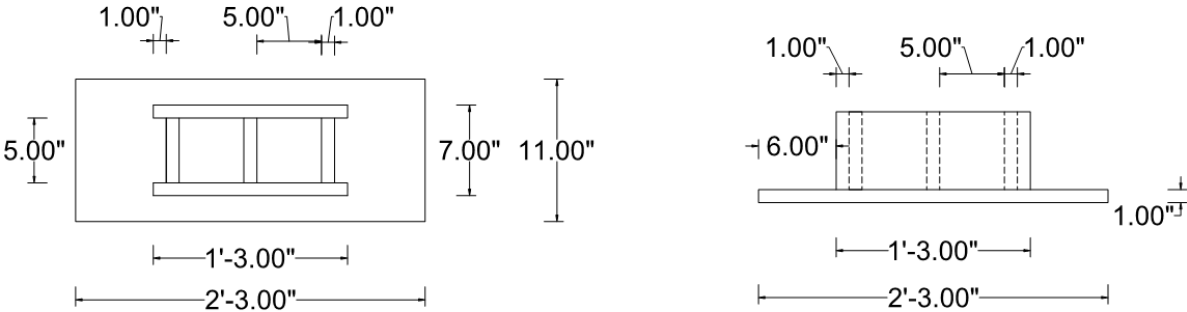


**Figure 30. Reinforcing bar layout of deck**

Each layer contained eight #7 bars in the longitudinal direction and sixteen #6 bars in the transverse direction, evenly spaced at 5.5 and 12 in., respectively, as shown in Figure 30. The longitudinal and transverse reinforcement ran continuously along the length and width of the specimen, respectively.

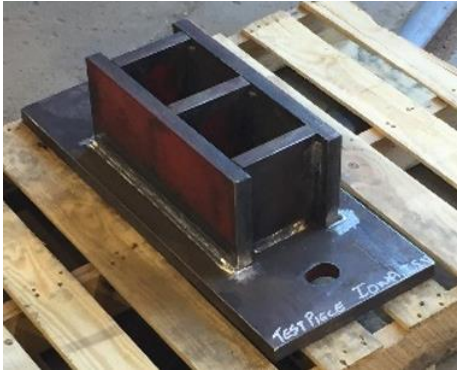
Concrete cover was 1 and 2.75 in. at the deck bottom and top, respectively. The concrete was specified to use the standard Iowa DOT HPC-D with a nominal compressive strength of 5 ksi.

The compression block and end steel plates were made of 1-in. thick steel plates, with details shown in Figure 29(a) and Figure 31.



(a) Top view

(b) Side view

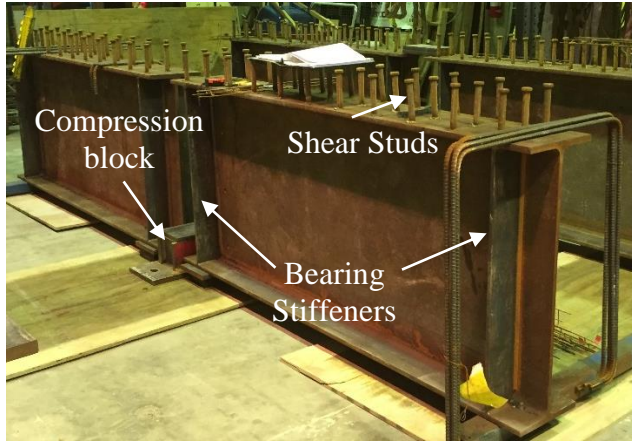


(c) Fabricated compression block

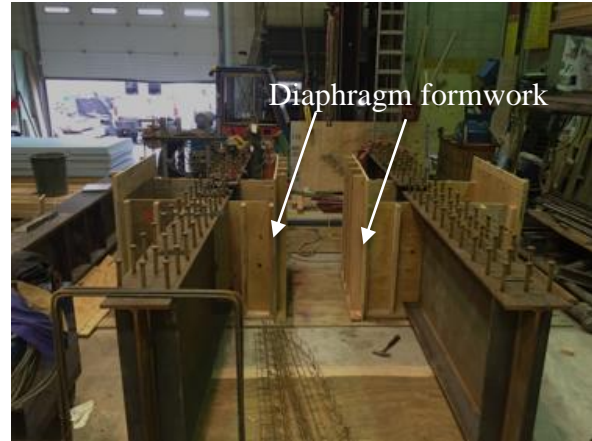
**Figure 31. Details of the compression block**

It should be noted that only incorporating a compression block into one specimen but keeping the rest of the design exactly the same made it possible to directly compare the results and to determine the effect the compression block had on the performance of the transverse connection.

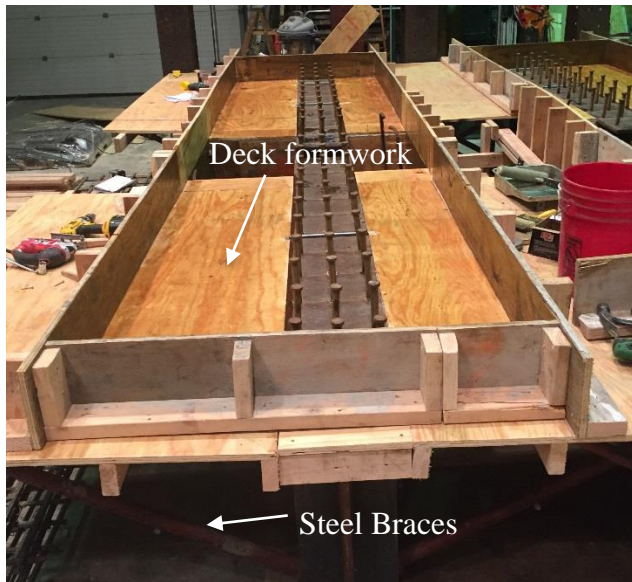
The shear studs were attached to the top flange as shown in Figure 32(a). To make sure the proper heat was being used, a 45-degree bending test was performed prior to welding the shear studs onto the girder flanges.



(a) Steel girders



(b) Diaphragm formwork



(c) Deck formwork



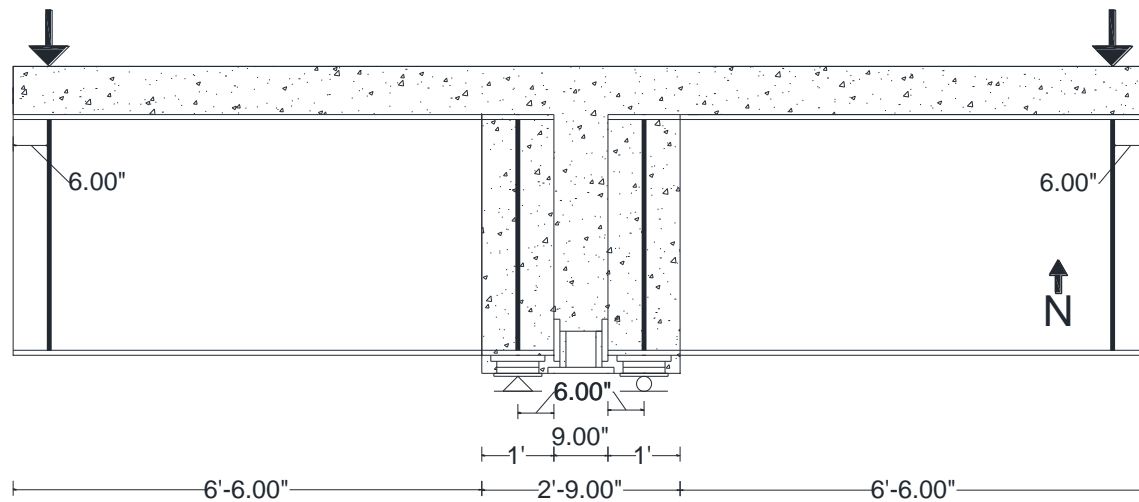
(d) Reinforcement

**Figure 32. Transverse connection fabrication procedure**

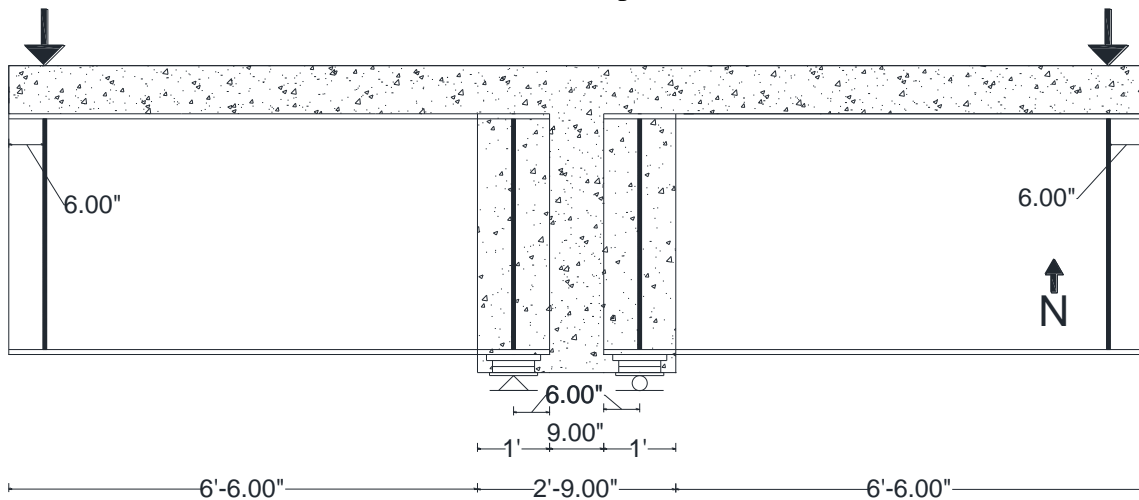
The compression block for the laboratory tests was fabricated by the same fabricator that would provide them for the Little Silver Creek Bridge, and the bearing stiffeners were full-length welded on each side. Construction of the formwork began when the girders were delivered to the laboratory. The sides for the diaphragm were constructed and slid into place forming a tight fit with the bottom flange as shown in Figure 32(b). The deck was formed and steel braces were used to support the overhangs of the decks as shown in Figure 32(c). After all of the formwork was assembled, the formwork was oiled and the reinforcing steel mats were lifted into place and the vertical diaphragm reinforcement was installed as shown in Figure 32(d). The concrete for the two specimens was placed using concrete from a single source and placed at the same time. Fifteen uniaxial strain gauges were installed on the top layer of the longitudinal bars near the diaphragm location prior to concrete placement. The specimens were tested after 28 days of curing and the 28-day compressive strength of the concrete was measured to be 5.5 ksi.

## Strength Tests

Strength tests were conducted on both specimens using the test setup. The goal was to determine how the compression block altered the performance of the specimen. In particular, strains were measured at several locations to determine how the compressive forces were being transferred through the diaphragms. To closely replicate the boundary conditions of the actual bridge, supports were placed under the bearing pads to simulate the contact points between the diaphragm and the pier. The supports were centered under the bearing pads and therefore located directly under the centerline of the girders. Figure 33 shows the setup details that were used.



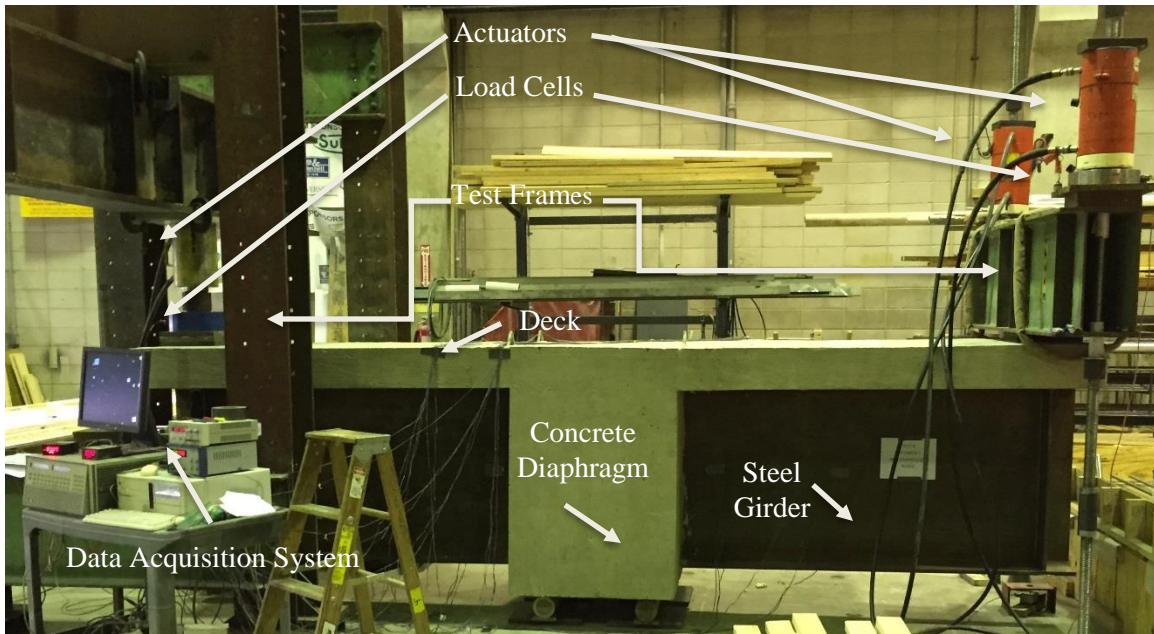
(a) Specimen I



(b) Specimen II

**Figure 33. Transverse connection strength test setup details**

Loading of the specimens was applied by a series of hydraulic actuators as shown in Figure 34.



(a) Front view



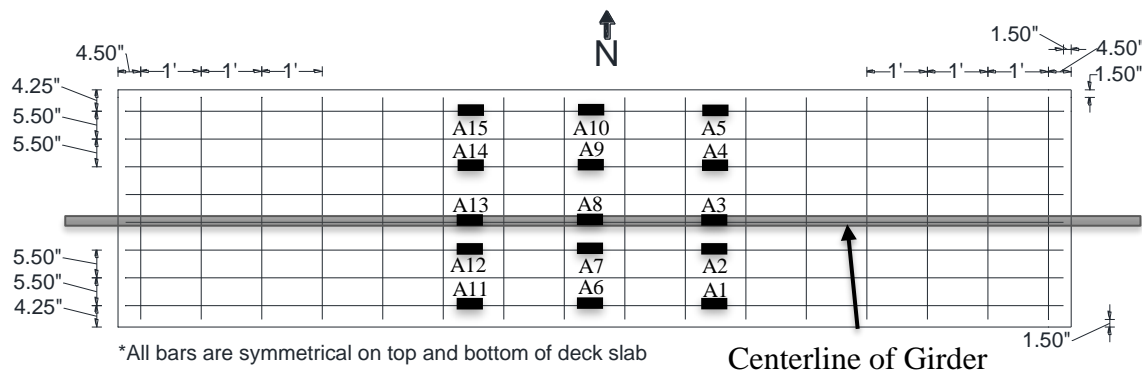
(b) Side view

**Figure 34. Transverse connection strength test setup**

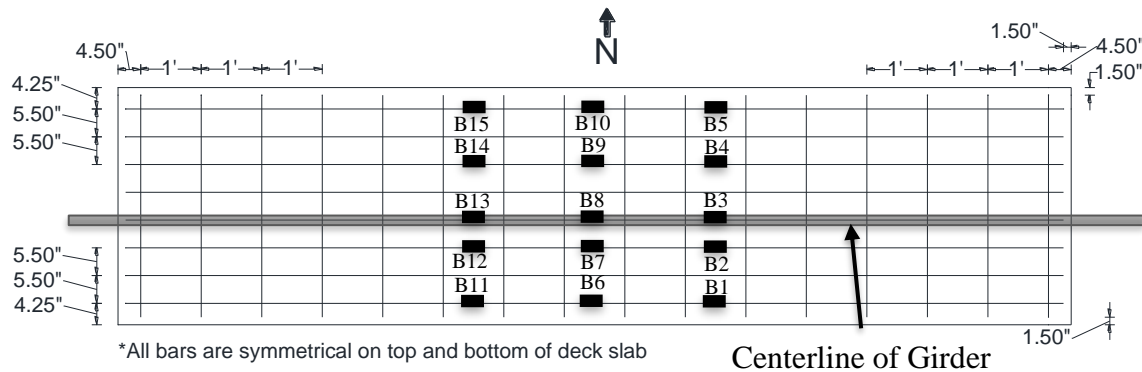
To produce the negative moment region at the diaphragm, two point loads were applied 6 in. from the outside edges of the specimens. The west side consisted of one 400 kip actuator mounted to a test frame while the east side consisted of two 200 kip hollow-core actuators secured to tie down rods. Due to the setup, the west actuator pressed down directly on a loading plate that was centered over the girder and the east actuators pressed down on a load beam that was positioned over a loading plate. A load cell was placed on each side and measured the applied load throughout the testing process.

During the testing process, the loading was stopped periodically to monitor crack formations. Conventional crack mapping techniques were used to document the crack patterns of each specimen. This was performed until the loading on each side reached approximately 300 kips and it was deemed no longer safe to approach the specimen. Cracks that formed after this point were marked after the load was removed and labeled with the maximum load applied.

The instrumentation plans for both specimens were exactly the same except for gauges placed on the compression block. For each specimen, there were 15 embedded strain gauges located in the deck panel and 12 surface-mounted strain gauges located on the girders. For the strain gauges on the steel bars embedded in the deck panel, five gauges were mounted in the center of the diaphragm and five gauges were installed 6 in. away from each side of the diaphragm as shown in Figure 35.



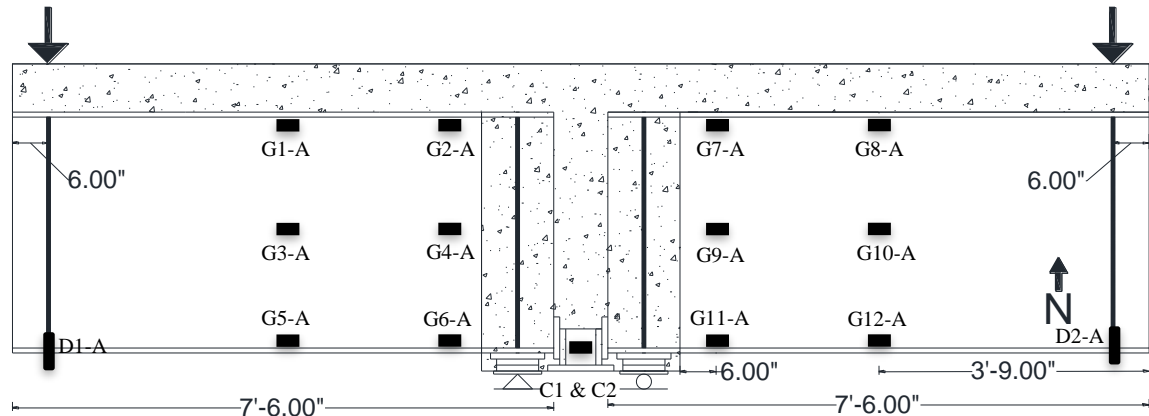
(a) Specimen I



(b) Specimen II

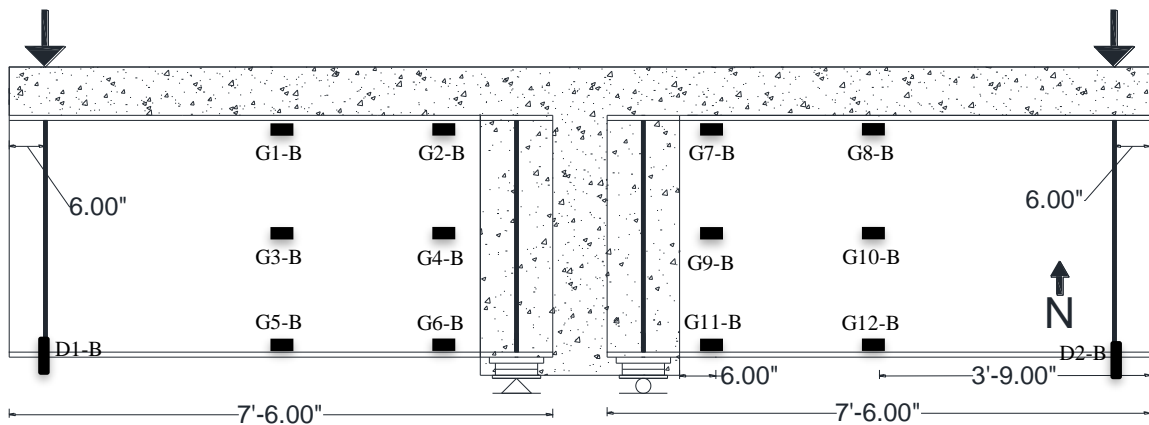
**Figure 35. Strain gauges on steel bars embedded in specimen deck panels**

The surface-mounted strain gauges on the girder were positioned on the bottom of the top flange, at the center of the web, and at the top of the bottom flange. Locations of these gauges were 6 in. outside the diaphragm and midpoint of the girder overhang for both the west and east side as shown in Figure 36.



\*Top gauges are attached to top flange.  
Bottom gauges are attached to bottom flange

(a) Specimen I



(b) Specimen II

**Figure 36. Strain gauges on specimen steel girders and compression block**

Note that the gauges with the letter A were installed on Specimen I and the gauges with the letter B were installed on Specimen II as shown in Figure 35 and Figure 36. Additionally, two strain gauges were installed on the outside face and mid-depth of the compression block of Specimen I. The locations that were used for the strain gauges made it possible to determine how the stresses were transferred through the diaphragm.

### Test Results and Discussions for Transverse Connections

#### *Concrete Compressive Strength*

The compressive strength of the concrete was tested to ensure adequate strength was attained for the specimens. Twelve 4 in. × 8 in. cylinders were cast during the placement of the HPC that was used for the concrete deck and diaphragm. Three cylinders were tested at a concrete age of 7, 14, and 28 days, respectively. The results for these tests are provided in Table 5.

**Table 5. HPC concrete deck and diaphragm compressive strength tests results**

<b>Concrete Age</b>	<b>Test 1 (psi)</b>	<b>Test 2 (psi)</b>	<b>Test 3 (psi)</b>	<b>Average (psi)</b>
7	3,582	3,605	3,389	3,525
14	4,750	4,770	4,630	4,717
28	5,540	5,462	5,590	5,531

Specimen II was tested after the concrete had a 28-day cure, since the HPC had exceeded the 5-ksi requirements. Due to the removal and set-up process, Specimen I was tested one week later after a 35-day cure time. For comparison purposes, all calculations were completed with an assumed average concrete compressive strength of 5,531 psi.

*Crack and Failure Patterns*

Conventional crack mapping techniques were used to monitor crack formations on both specimens. Locating the initial cracks and tracking their progression made it possible to determine how the stresses were transferred through the diaphragm. Cracks were mapped after load increments of 50 kips were applied to each end. All of the loads that were noted during testing are referenced here in terms of moments based on the locations for the point of interest. This was done for ease of the reader and to allow the moment capacity of the section to be directly analyzed. The distance of the moment arm for several key locations on the specimen is referenced in Table 6.

**Table 6. Distance from loading to gauge locations**

<b>Location</b>	<b>Moment Arm (ft)</b>
6 in. west of the diaphragm	5.5
Center of diaphragm	6.5
6 in. east of diaphragm	5.5
Midpoint of girder	3.25
Edge of diaphragm (lifting hooks)	6.0

Cracking for both specimens originated in the top of the deck slab right on the outside edges of the diaphragm as shown in Figure 37.

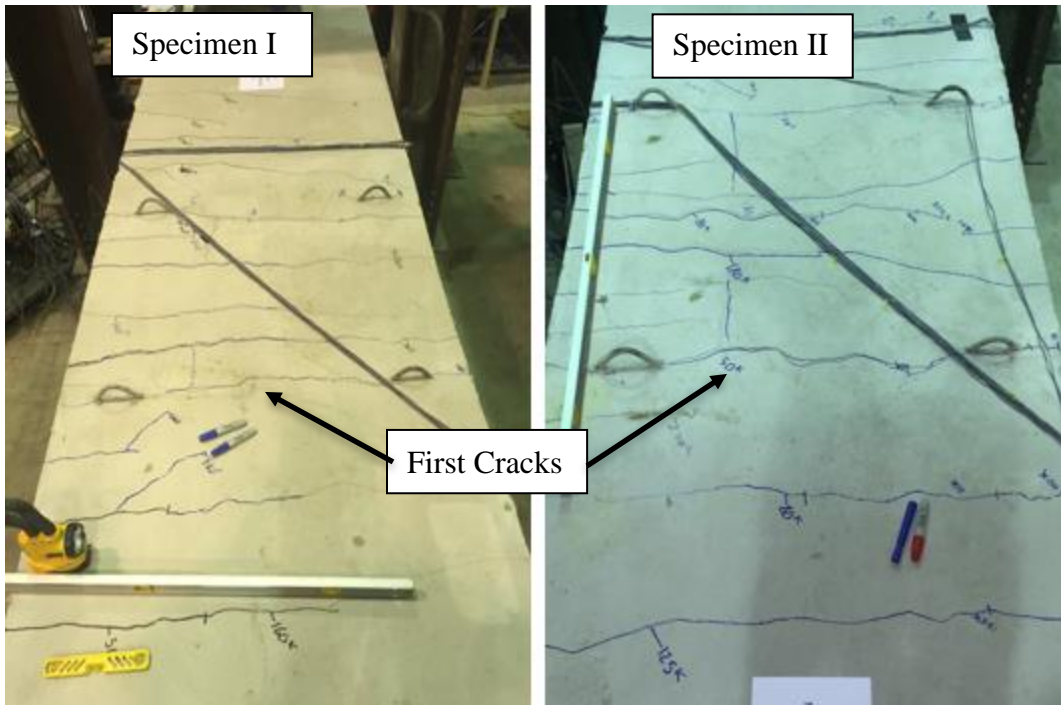


**Figure 37. Crack formations on deck slab for each specimen**

Cracking of Specimen II was first noticed when a load of about 50 kips was applied to each side, which corresponds to a moment around 300 ft-kip at the crack location. The first cracks ran across the width of the specimen along the same line as the lifting hooks. As the loading increased, cracks were formed 1 ft outside the edges of the diaphragm followed by cracks located in the center of the diaphragm. Vertical cracks on the sides of the specimen became noticeable around 100 kips (650 ft-kip). These cracks extended down the specimen toward the supports and opened as the yielding load was approached. Cracking down the vertical face of the diaphragm varied on each side. The short overhang side showed significantly more cracking than the long side did. Figure 38 and Figure 39 show the crack formations for the short and long sides of the diaphragm of each specimen, respectively.

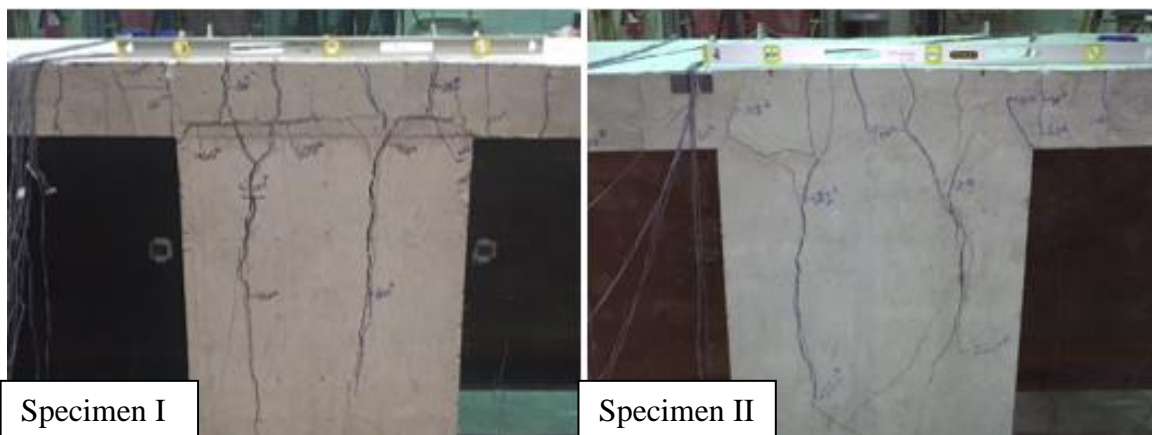


**Figure 38. Diaphragm cracks on short side for each specimen**



**Figure 39. Diaphragm cracks on long side for each specimen**

Cracks on the long side did not continue down the vertical face of the diaphragm, but continued to the bottom on the short side. Almost all of the cracking on the specimens ran in the transverse direction, along the width of the specimen. After the maximum load was reached and each specimen was unloaded, a few longitudinal cracks were noticed. Specimen II had a localized failure due to concrete crushing under the loading on the east side as shown in Figure 40.

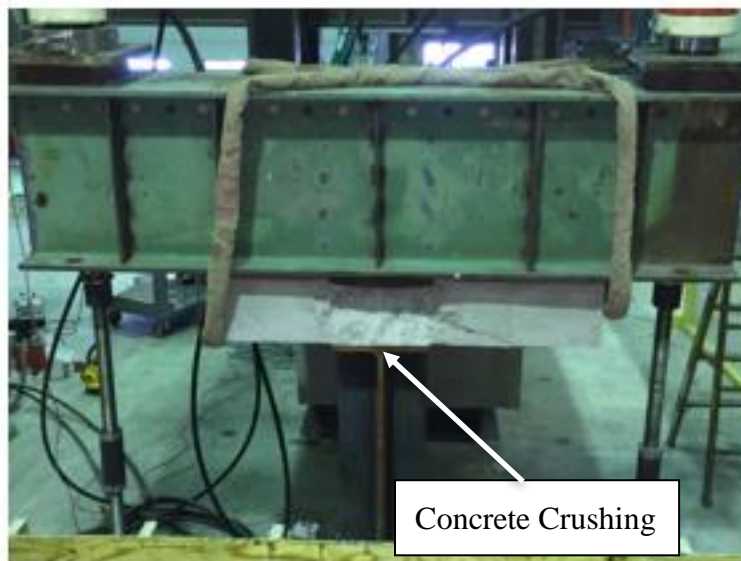


**Figure 40. Localized failure of Specimen II under the loading point**

The reinforcing steel mat over the diaphragm had yielded, but did not reach its ultimate strength. This implies that the concrete diaphragm would have been able to carry some amount of additional load before reaching its capacity. The diaphragm was also subject to permanent deformation since the reinforcing steel reached strain levels past the yielding point. No fracture was observed in the steel reinforcement as shown in Figure 41.

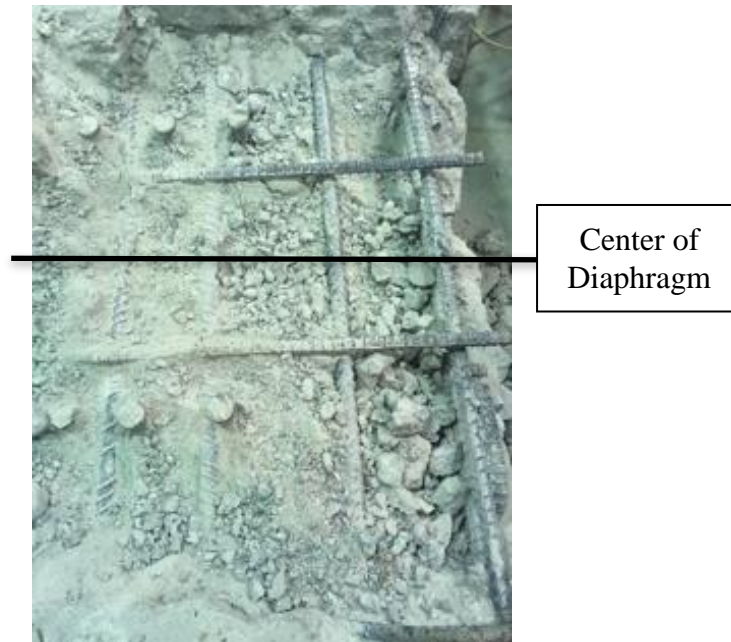


**Figure 41. Specimen II reinforcing steel examination**

Cracking and failure patterns for Specimen I were very similar to those of Specimen II. Again, the first cracks were noticed at a load of about 50 kips (300 ft-kip) applied to each side and spanned along the width of the specimen in line with the lifting hooks as shown previously in Figure 38. Cracking then followed the same pattern, showing up 1 ft outside the diaphragm, in the center of the diaphragm, and along the vertical face of the deck. Cracking of Specimen I appeared to be more spread out from the loading locations than Specimen II. The cracks on the face of the diaphragm were also very similar. Minimal cracking was observed on the long overhang side, but cracks extended all the way down the face to the supports on the short side, which was shown in Figure 38 and Figure 39. Small cracks formed on the bottom of the diaphragm and spread to the neoprene bearing pads as shown in Figure 42.

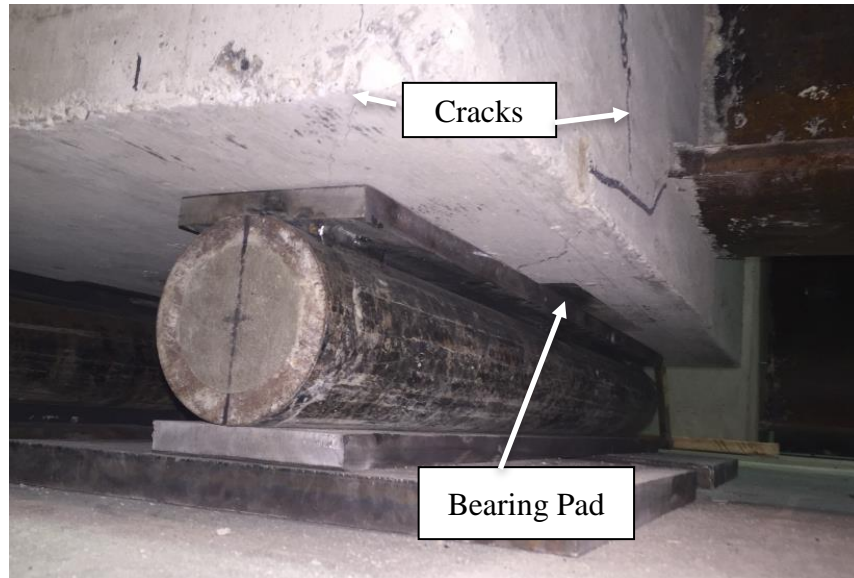


**Figure 42. Cracking of diaphragm for Specimen I**

A larger plate was used at the loading locations to prevent concrete crushing as shown in Figure 43.



**Figure 43. Revised loading configuration of Specimen I**

Ultimate failure was taken as the maximum loading withstood during testing. At this load, deflection continued to increase rapidly while the actual load was not increasing. The steel reinforcement over the diaphragm had yielded and the specimen was subject to permanent deformation.

### Loads, Strains, and Deflections

For both specimens, the concrete-cracking load, steel-yielding load, ultimate load, and deflection at maximum load were determined. Again, these loads were referenced in terms of moments, using the moment arm for each section as noted previously in Table 6.

For comparison purposes, strain results were discretized by location: 6 in. west of the diaphragm, center of the diaphragm, 6 in. east of the diaphragm, and midpoint of the girders. The cracking load was estimated based on the load-strain relationships of the embedded strain gauges, which are shown in Figure 44 through Figure 49.

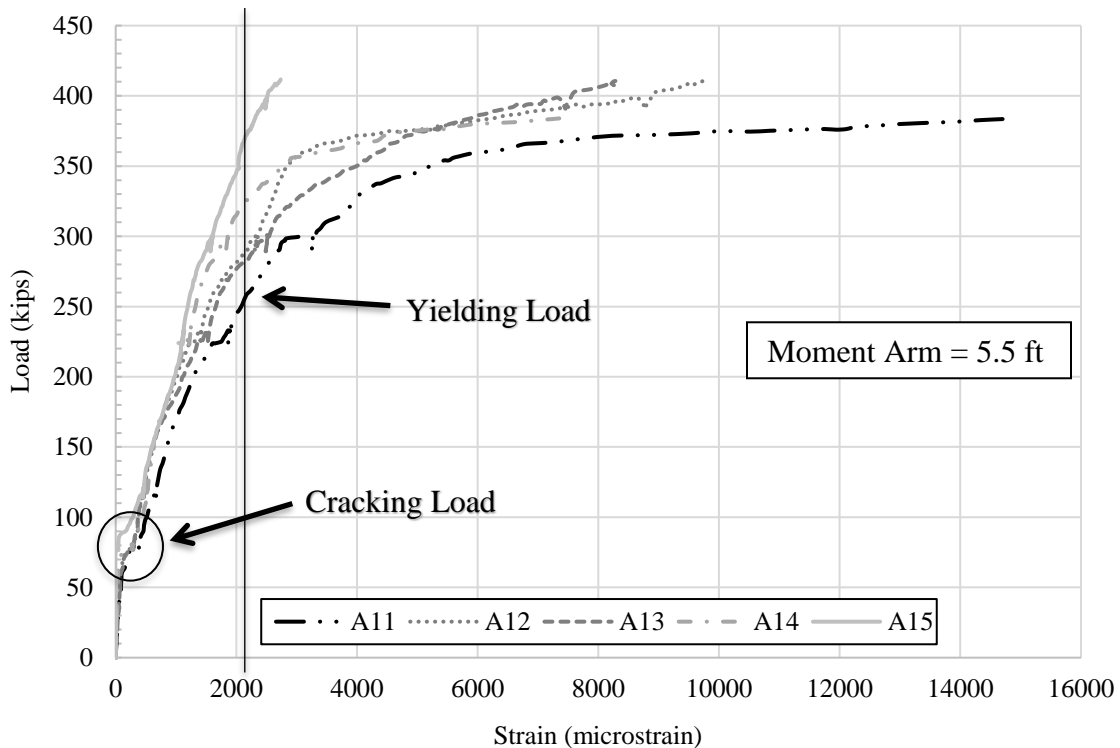


**Figure 44. Transverse connection load vs. strain 6 in. west of the diaphragm - Specimen I**

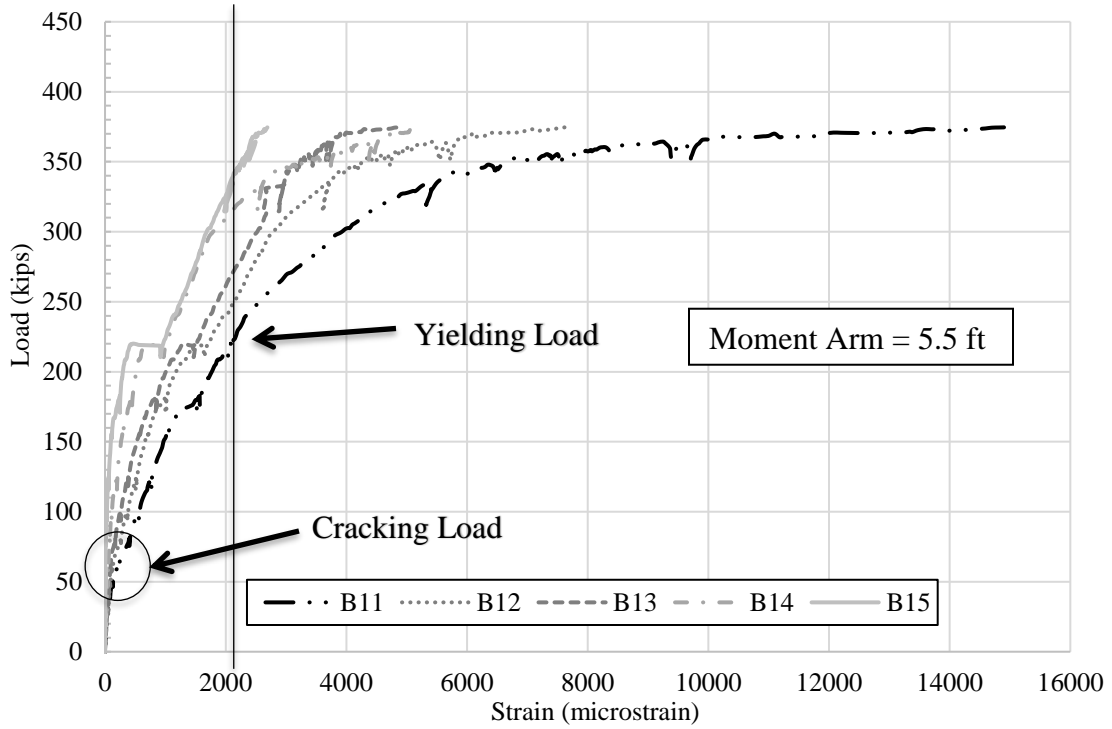


**Figure 45. Transverse connection load vs. strain 6 in. west of the diaphragm - Specimen II**

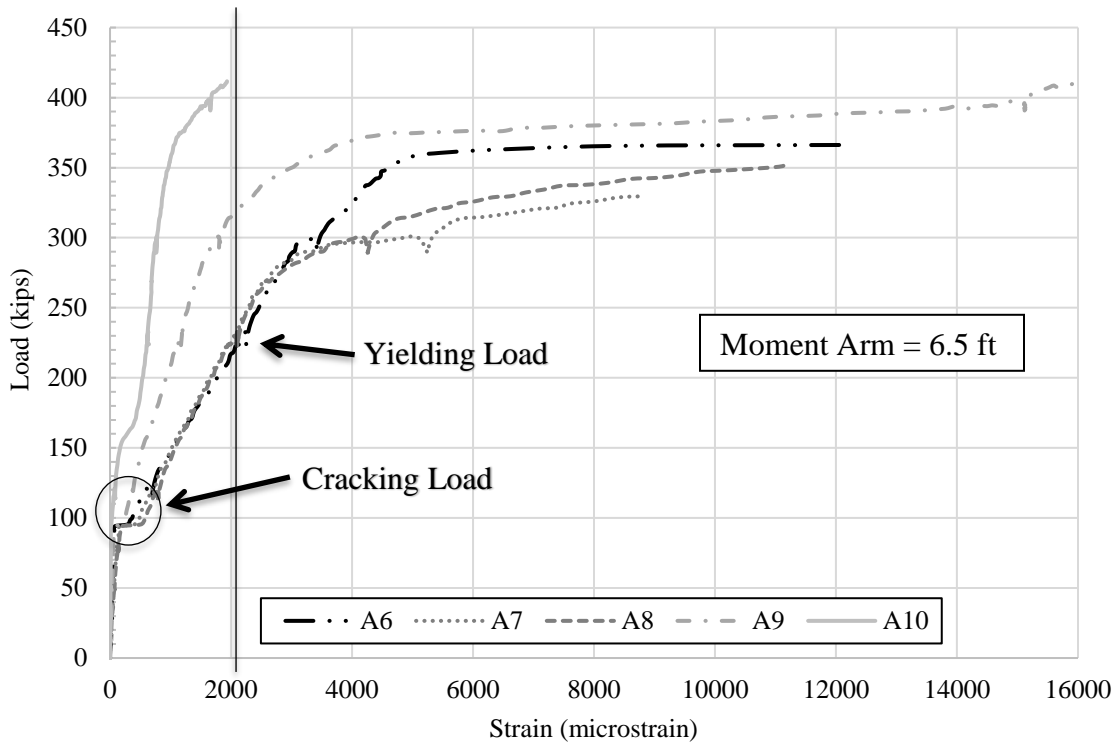


**Figure 46. Transverse connection load vs. strain center of the diaphragm - Specimen I**

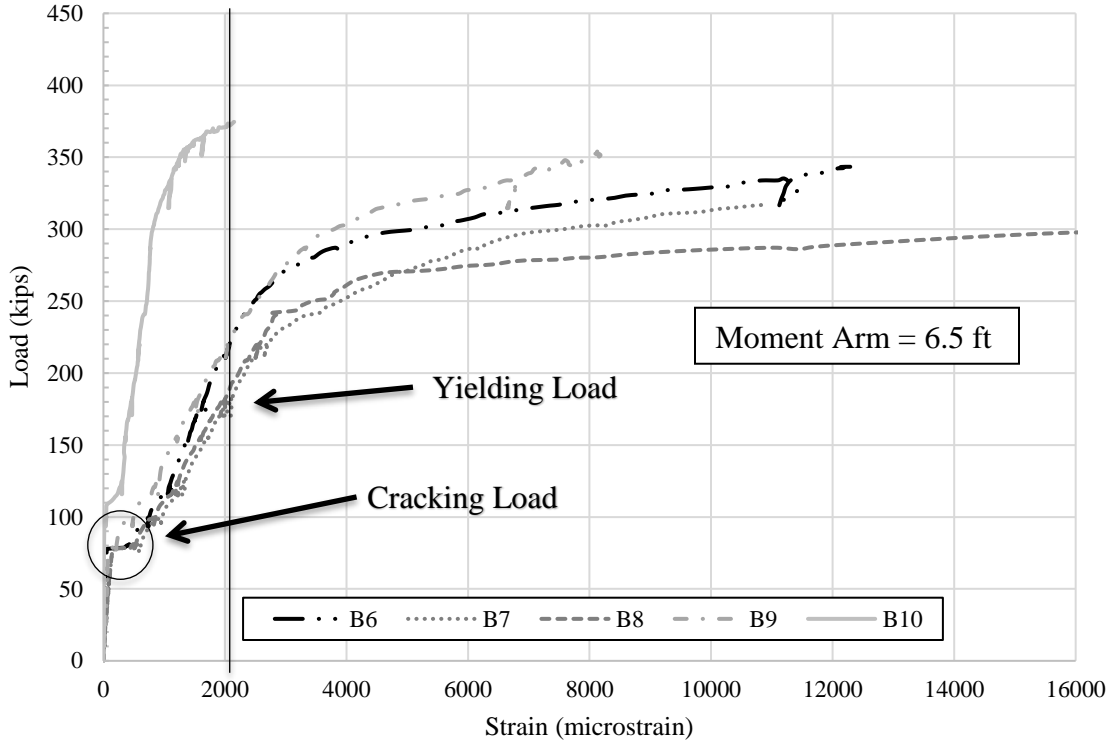


**Figure 47. Transverse connection load vs. strain center of the diaphragm - Specimen II**

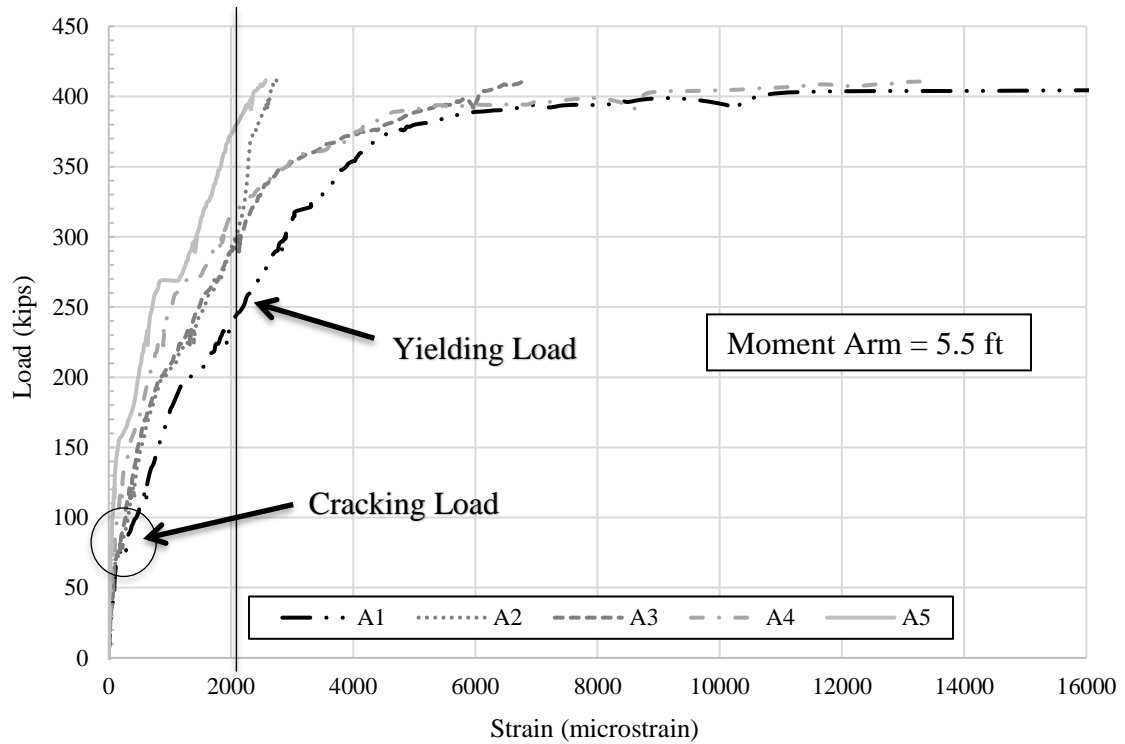


**Figure 48. Transverse connection load vs. strain 6 in. east of the diaphragm - Specimen I**

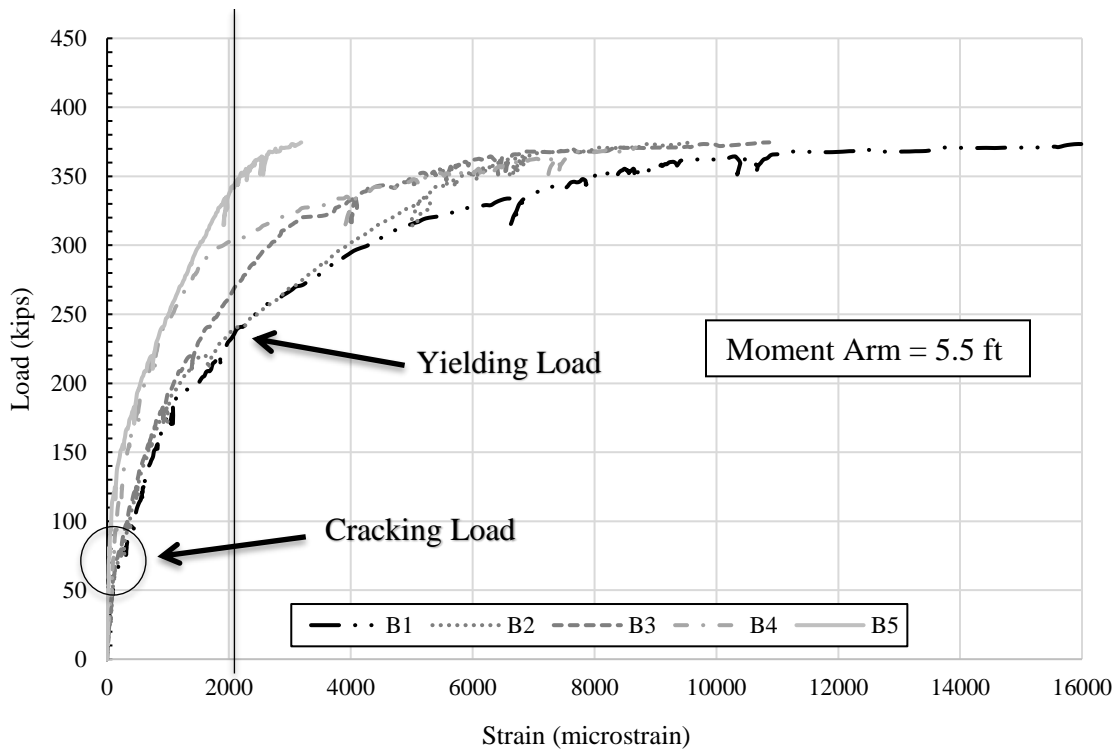


**Figure 49. Transverse connection load vs. strain 6 in. east of the diaphragm - Specimen II**

The first point the strain value reached a plateau (an abrupt increase in strain) was recorded as the cracking load. For locations where the initial plateau was not as evident, the cracking load was determined once the first steel reinforcement in the deck reached a strain value equal to that of tensile cracking of concrete, which corresponds to about 135 micro-strains based on a linear stress-strain curve. Since the embedded strain gauges were very close to the surface of the deck, the results produced from strain gauge readings are assumed to closely represent the strain values on the deck surface.

As for the yielding load, Grade 60 reinforcing steel was used for this project, which has a theoretical yield strain of 2,069 microstrain. The load at which the average strain in the cross-section exceeded this limit was taken as the yielding load of steel reinforcement.

Grade 50 steel was used for the W40x149 girders. The corresponding yielding strain is 1,724 microstrain, and the yielding strain during testing was tracked using the surface-mounted gauges positioned along each girder. The largest values during the test for load and deflection were recorded as the ultimate load and maximum deflection, respectively. The following load-strain relationships were developed from the embedded strain gauges attached to the top mat in each bridge deck specimen. The cracking and yielding load along with the moment arm to each section are illustrated Figure 44 through Figure 49.

A review of Figure 44 through Figure 49 reveals that Specimen I was able to sustain higher loads than Specimen II prior to the different failure points, such as cracking and yielding. For quicker

comparison between the different sections for the two specimens, the minimum values produced in these figures are shown in Table 7. Again, the load values for the failure points are referenced back to as moments based on the locations of the section.

**Table 7. Summary of test results at each cross-section**

	<b>Cracking Load (kip) (Moment / ft-kip)</b>		<b>Yielding Load (kip) (Moment / ft-kip)</b>	
	<b>Specimen I</b>	<b>Specimen II</b>	<b>Specimen I</b>	<b>Specimen II</b>
<b>6 in. West of the Diaphragm (Moment Arm = 5.5 ft)</b>	65 (357.5)	55 (302.5)	255 (1,402.5)	220 (1,210)
<b>Center of Diaphragm (Moment Arm = 6.5 ft)</b>	90 (585)	75 (487.5)	225 (1,462.5)	180 (1,170)
<b>6 in East of the Diaphragm (Moment Arm = 5.5 ft)</b>	70 (385)	65 (357.5)	245 (1,347.5)	240 (1,320)
<b>Minimum Load</b>	<b>65</b>	<b>55</b>	<b>225</b>	<b>180</b>
<b>Corresponding Moment (ft-kip)</b>	<b>357.5</b>	<b>302.5</b>	<b>1,462.5</b>	<b>1,170</b>

The overall load required for cracking was higher for Specimen I than for Specimen II. As previously discussed, the first cracks were noticed just outside of the diaphragm and worked their way toward the load lines before appearing in the center of the diaphragm. This pattern was also confirmed by the data, which show that the center of the diaphragm sustained a significantly higher load prior to cracking than the locations 6 in. outside of it. For Specimen I, this difference is clearly shown by comparing Figure 44 and Figure 46, which are strain relationships 6 in. west of the diaphragm and center of the diaphragm, respectively. Based on the strain values and a cracking strain of 2,069 microstrain, the first cracks for Specimen I were formed at a load of about 65 kips, which relates to a moment of 357.5 ft-kip. Cracks for Specimen II formed earlier – at about 55 kips, which relates to a moment of 302.5 ft-kip. However, these loads are the minimum loads to produce cracking at the section in which the embedded gauges were located (see previous Figure 35).

Specimen I also sustained higher loads at the point of the first bar yielding. The yielding of both specimens occurred first at the center of the diaphragm. Specimen I was able to withstand a total load of 225 kips prior to the first bar yielding, while Specimen II was only able to handle a load of 180 kips. This corresponds to a yielding moment of 1,462.5 ft-kip for Specimen I and 1,170 ft-kip for Specimen I. However, as shown in Figure 44 through Figure 49, there was a large deviation of strain results produced throughout each section.

To better understand how the forces were distributed throughout the two specimens, transverse strain values across the width of the specimens were plotted for all three different longitudinal cross-sections: 6 in. west of the diaphragm, center of the diaphragm, and 6 in. east of the diaphragm. Note the gauge locations for these cross-sections were shown in Figure 35, and the

strain distributions are shown in Figure 50 through Figure 52. For reference, the moment arm at each cross-section is given in Table 6.

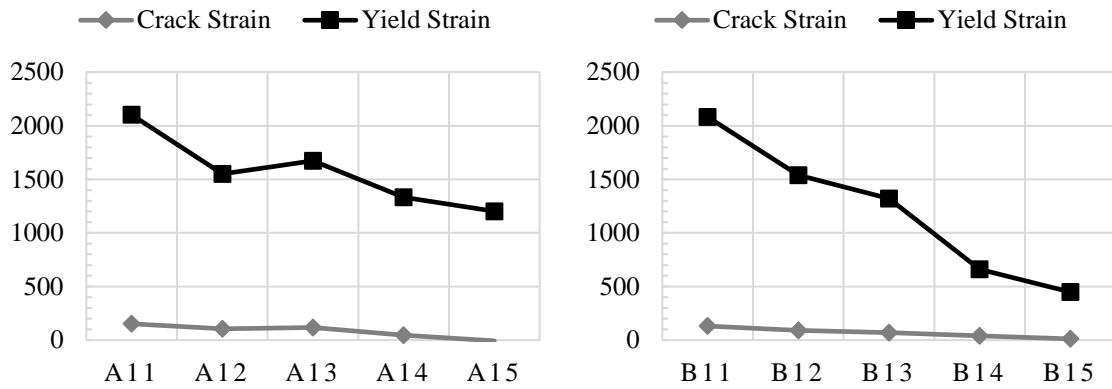


**Figure 50. Transverse strain values 6 in. west of the diaphragm for the two specimens**

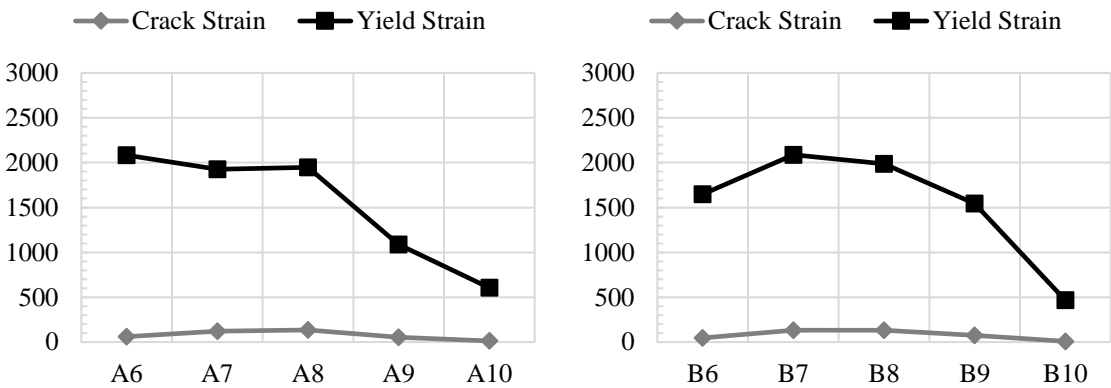


**Figure 51. Transverse strain values center of diaphragm for the two specimens**

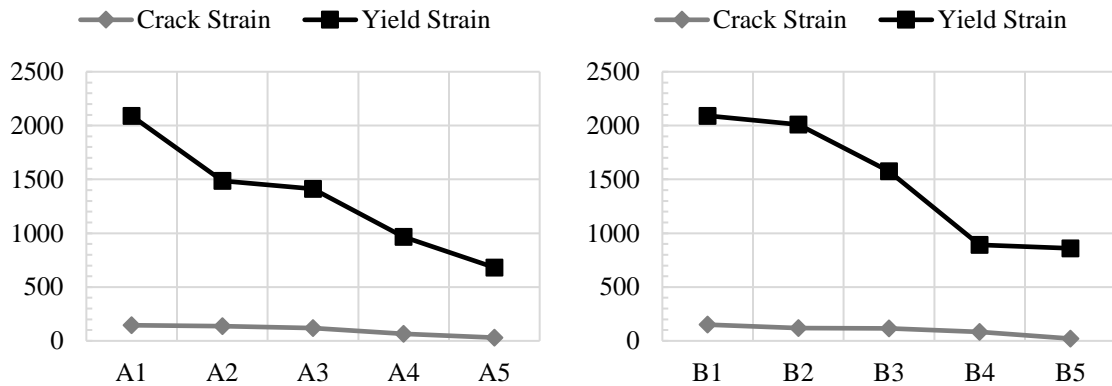


**Figure 52. Transverse strain values 6 in. east of the diaphragm for the two specimens**

The transverse strain relationships were developed individually for each cross-section. For example, once the first bar reached the theoretical yield limit of 2,069 microstrain, all other strain values at that point of time were used for each section. The same goes for cracking strain.

As shown previously in Figure 50 through Figure 52, both the east and west side of the diaphragm produced very similar results (see Figure 57 later for loading rates). Strain readings were highest toward the edge of the short overhang side and decreased along the width of the specimen to the edge of the long overhang side. This pattern was consistent for both crack and yield strains for the sections outside of the diaphragm. The center of the diaphragm, shown in Figure 51, showed slightly different results. The strain readings were highest toward the centerline of the girder, where the load was applied, and gradually became smaller as they got further away. The short overhang side still experienced about three times the strain as that seen on the long side. Relating back to the visual crack mapping that was previously discussed, it makes sense why several more cracks were noticed on the short overhang side. The gauges toward the edge of the long overhang side had substantially lower strain readings throughout the whole length of the specimen. The individual results for these three cross-sections were summarized in Table 7. The lowest load of the three sections was used for the overall comparison later in Table 8.

Relationships for loading and girder strains were also developed and are shown in Figure 53 and Figure 54.

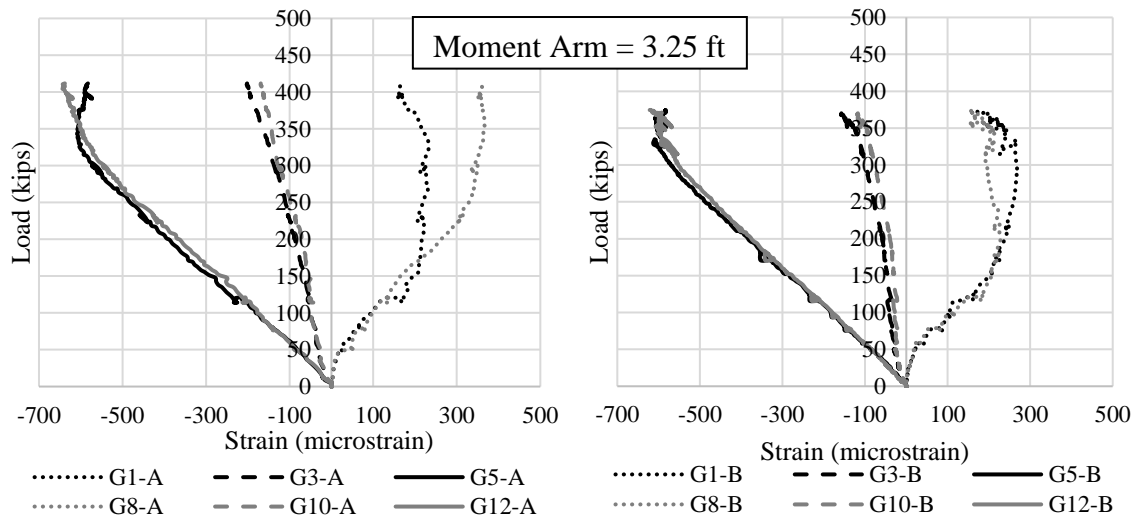


**Figure 53. Load vs. strain on girder at midpoint for the two specimens**

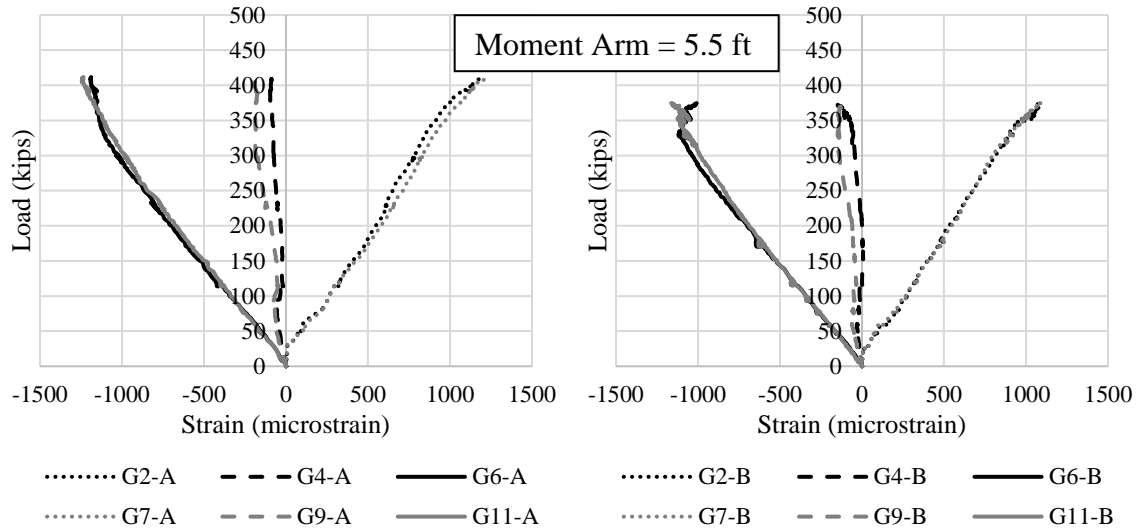


**Figure 54. Load vs. strain on girder 6 in. outside of diaphragm for the two specimens**

Locations of the strain gauges used for the comparisons were shown previously in Figure 36. Both the east and west gauges are included in Figure 53 and Figure 54. For quick identification, different line types were used based on whether the gauge was installed on the top flange (dots), middle of the web (dashed), or the bottom flange (solid). The darker line represents all of the gauges on the west girder and the lighter line represents all of the gauges on the east girder.

Strains on both the west and east side of the diaphragm were comparable for both specimens at matching locations. When comparing absolute strain values for both specimens, the results are almost identical. All of the gauges mounted to the middle of the web had very small strain readings. These readings were almost always negative indicating compressive forces and confirming the location of the neutral axis is just above the center of the girders. Specimen II showed very small readings of tensile forces for a short period of loading, but, for the most part, only compressive forces were seen in the center of the web. With a maximum strain at about 1,200 microstrain, all locations remained elastic, as the yield limit of 1,724 microstrain was not reached for the girders.

Load-strain relationships for the compression block were very similar to those of the bottom flange of the girder. As shown in Figure 55, only compressive forces were transferred through the compression block. Based on visual observation after testing was concluded, it was evident that the concrete diaphragm never failed under compression and was still able to transfer some of the compressive forces.

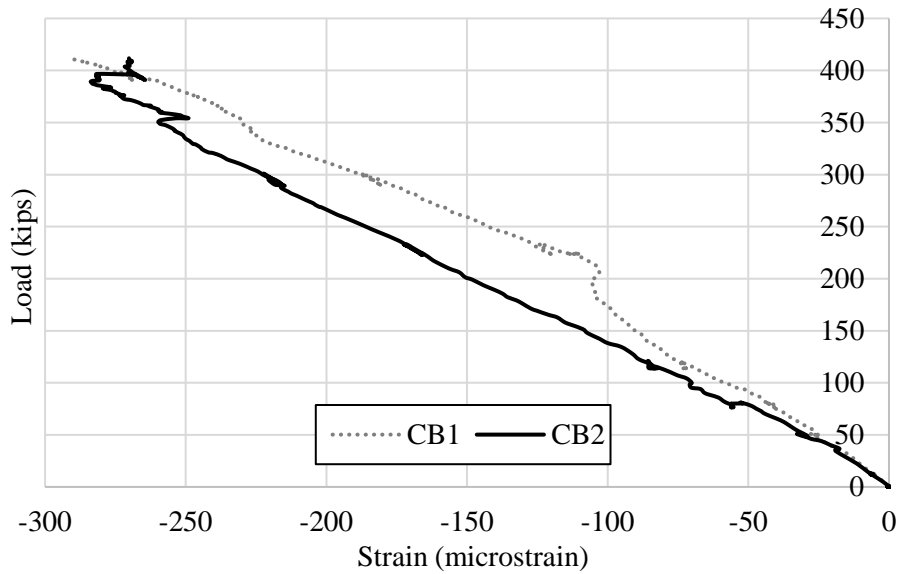


**Figure 55. Load vs. strain on compression block**

Load-deflection relationships for both specimens are shown in Figure 56.

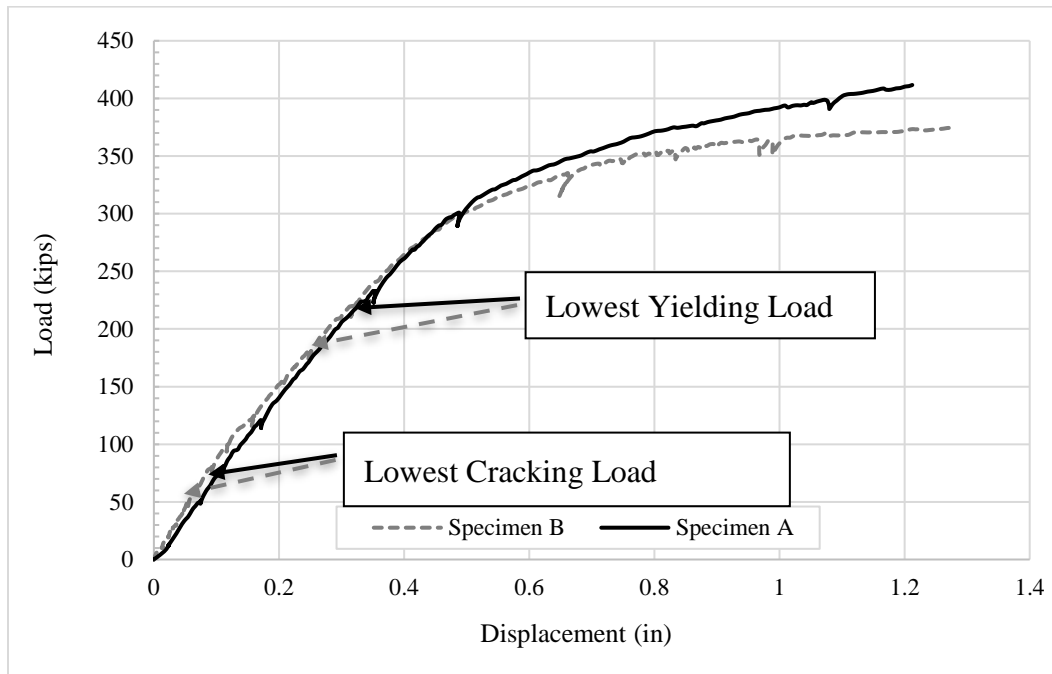


**Figure 56. Load vs. displacement of both specimens**

It should be noted that deflection during early stages of loading was very sensitive. Since an electric pump applied the east load and a hand pump applied the west load, it was difficult to keep the load rates constant at the beginning. For this reason, the average displacements for both sides were used to compare the specimens. Loading rates for both sides are shown in Figure 57.

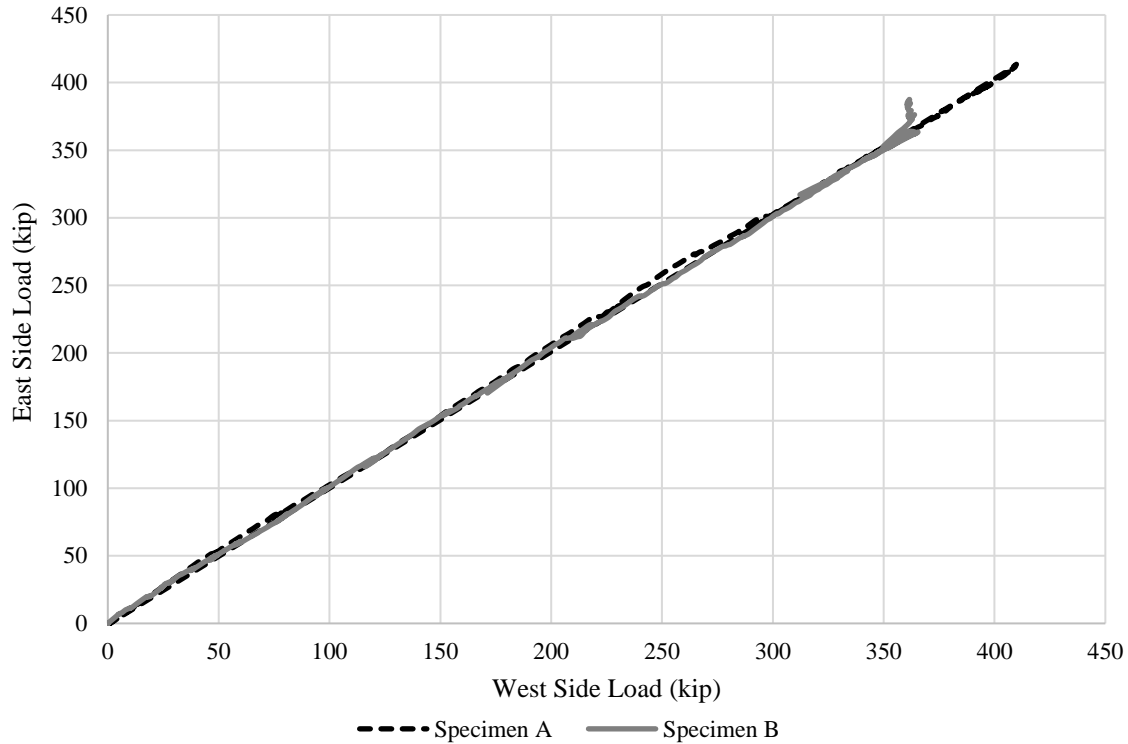


**Figure 57. West vs. east loading rates**

Both specimens had very similar deflection results. The specimens appeared to have a linear deflection until the steel bars in the center of the diaphragm had yielded. After yielding of the steel bars, the deflection of both specimens continued to increase due to smaller increments of loading. Specimen I was able to withstand a greater load than Specimen II at the same deflection. Toward the end of testing, it appeared that both specimens would not be able to handle much additional load, but the deflection significantly increased.

Based on the results provided in this section, it is evident that Specimen I, which included the compression block, produced more favorable results. The overall results are summarized in Table 8.

**Table 8. Summary of critical test results**

Specimen	Cracking		Yielding		Ultimate		Maximum Deflection (in.)
	Load (kip)	Moment (ft-kip)	Load (kip)	Moment (ft-kip)	Load (kip)	Moment (ft-kip)	
<b>I</b>	65	357.5	225	1,462.5	412	2,678	1.20
<b>II</b>	55	302.5	180	1,170	375	2,437.5	1.28

## Numerical Simulation, Results, and Discussions

Three-dimensional nonlinear FE models were established to further investigate the performance of the longitudinal and transverse joint specimens.

### *FE Modeling of Longitudinal Joints*

The concrete deck and longitudinal connection were both modeled using an eight-noded solid element with three translational degrees of freedom at each node plus cracking and crushing capabilities. The Poisson's ratio of the concrete was set to 0.2. The concrete material properties were also assigned with multi-linear isotropic hardening in combination with the von Mises yield criterion. The stress-strain relationships of the normal-strength concrete and UHPC can be expressed by Equations (1) and (2), respectively, according to Hognestad (1951) and Schmidt and Fehling (2005), respectively.

$$f_c = f'_c \left[ 2 \left( \frac{\varepsilon}{\varepsilon_{o,n}} \right) - \left( \frac{\varepsilon}{\varepsilon_{o,n}} \right)^2 \right] \quad (1)$$

$$f_c = f'_c \left[ 1 - \left( 1 - \frac{\varepsilon}{\varepsilon_{o,u}} \right)^n \right] \quad (2)$$

where,  $f_c$  and  $\varepsilon$  = stress and strain on concrete respectively,  $f'_c$  = concrete compressive strength,  $n$  = parameter, which equals 1.4 for the UHPC compressive strength of 18.2 ksi, and  $\varepsilon_{o,n}$  and  $\varepsilon_{o,u}$  = strain at peak stress for normal-strength concrete and UHPC respectively, expressed by Equations (3) and (4), respectively.

$$\varepsilon_{o,n} = 0.00048(f'_c)^{1/4} \quad (\text{in ksi}) \quad (3)$$

$$\varepsilon_{o,u} = \frac{f'_c}{E_{c,u}} \quad (4)$$

where,  $E_{c,u}$  = elastic modulus of UHPC, which can be expressed by Equation (5) (Russell and Graybeal 2013):

$$E_{c,u} = 1550\sqrt{f'_c} \quad (\text{in ksi}) \quad (5)$$

The smeared fixed crack model and Rankine maximum stress criterion were utilized to determine the initiation and development of concrete cracking. The tensile strength of the

normal-strength concrete and UHPC can be derived by Equations (6) and (7) based on AASHTO (2010) and Russell and Graybeal (2013), respectively.

$$f_t' = 0.24\sqrt{f_c'} \quad (\text{in ksi}) \quad (6)$$

$$f_t' = 0.21\sqrt{f_c'} \quad (\text{in ksi}) \quad (7)$$

The steel bars were modeled using a uniaxial tension-compression element with three translational degrees of freedom at each node. A perfect elastic-plastic uniaxial material model was used for the steel. The yield strength, elastic modulus, Poisson's ratio, and tangent modulus of the steel were set to 60 ksi, 29,000 ksi, 0.3 and 0, respectively. The steel bars were perfectly connected to the concrete through sharing of common nodes. The concrete deck was also perfectly connected to the UHPC connection through sharing common nodes. Note that no relative displacement was observed between the deck panels and connections and cracking was only found in the interface or normal-strength concrete during testing. Accordingly, full bond was assumed at the interfaces between the concrete decks and connections and the maximum bond strength should be equal to the tensile strength of the normal-strength concrete.

Due to the asymmetry of the reinforcing detail in the jointed specimens, full models were established for all specimens as shown in Figure 58.

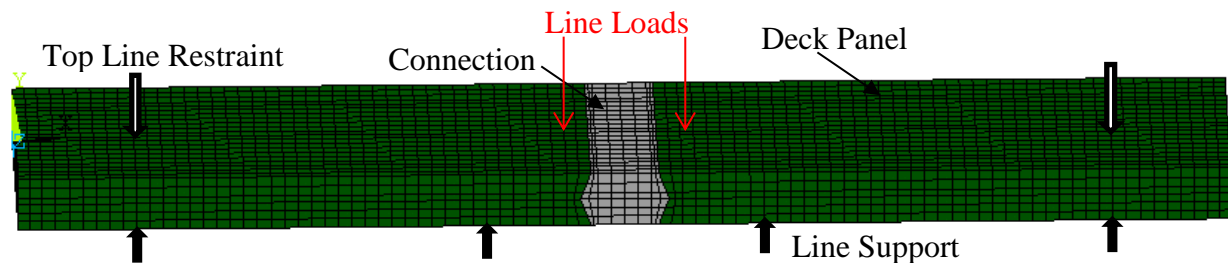


**Figure 58. FE model of jointed (or jointless) specimens**

Note that similar meshes were utilized for the two types of specimens, but the material properties of the normal-strength concrete and UHPC were appropriately assigned. Line loads were applied on the nodes of the FE model at the loading location, and boundary conditions were defined to simulate the four support locations shown in Figure 58.

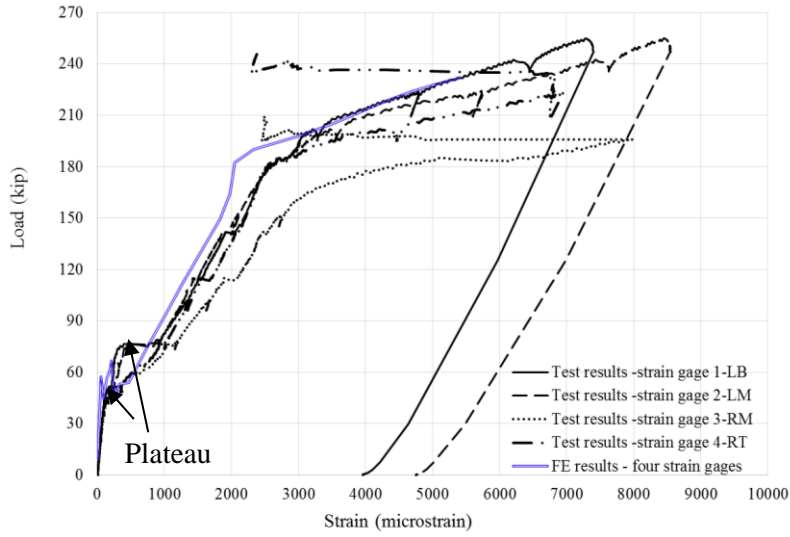
Convergence criteria and tolerances were set for the displacement and force. The following strategies were utilized to facilitate convergent computations (Deng et al. 2013, Deng and Morcouc 2013, Deng et al. 2016a, Deng et al. 2016b, Deng et al. 2016c):

1. Concrete compressive stress was constrained to a constant value after reaching its peak value

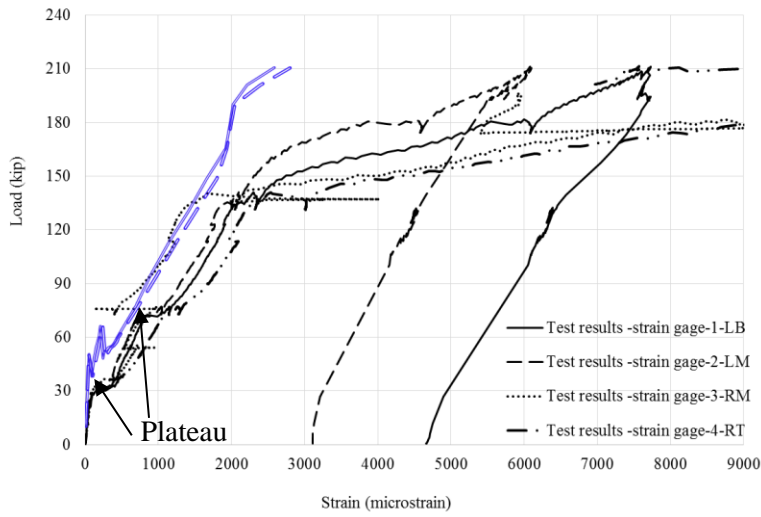
2. Appropriate shear transfer coefficients were used for open and closed cracks, respectively
3. Capability of concrete crushing was deactivated in the analysis, but the failure of the model was determined when the concrete reached the maximum compressive strain of 0.003 (i.e., concrete failure strain)
4. Suppression of extra displacement shapes and tensile stress relaxation after cracking were applied to solid elements

#### *Comparisons of Measured and Predicted Results for Longitudinal Joints*

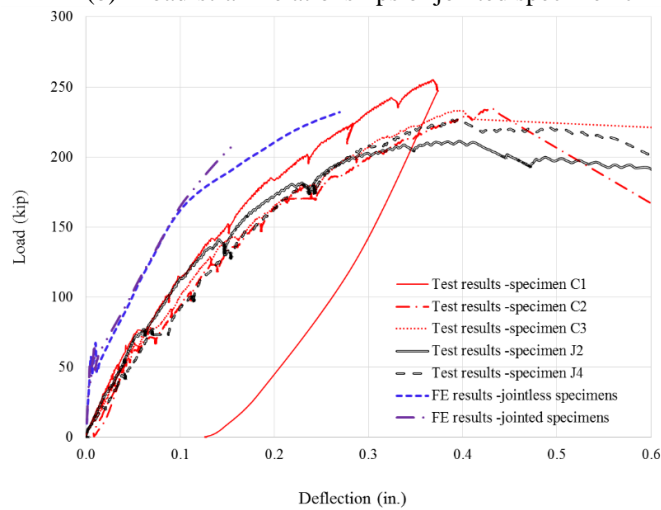
Load-strain relationships were developed based on the measured strains in the four gauges for each of these specimens. A typical load-strain relationship for jointless specimen C1 and jointed specimen J2 are illustrated in Figure 59(a) and Figure 59(b), respectively.



(a) Load-strain relationships of jointless specimen-C1



(b) Load-strain relationships of jointed specimen-J2



(c) Load-deflection relationships

**Figure 59. Comparison of relationships obtained from test results and FE models**

For each load-strain relationship, a plateau can be observed at an early loading stage due to the concrete cracking shown in Figure 59. For each specimen, the load at concrete cracking was determined based on the smallest plateau of the four load-strain relationships; these are summarized in Table 9.

**Table 9. Summary and comparisons of test and FE results**

Type of Specimens	Slab No.	Joint Surface Preparation Technique	Load at Concrete Cracking (kips)		Load at Steel Yield (kips)		Load at Specimen Failure (kips)			Deflection at Maximum Load (in.)	
			Test	FEA	Test	FEA	Test	FEA	STM	Test	FEA
Jointless Specimens	C1	N/A	52	57	115	164	250	232	225	0.37	0.27
	C2	N/A	56		123		235			0.42	
	C3	N/A	39		126		230			0.39	
Jointed Specimens	J1	Rubber sandblast medium	34	49	110	180	195	210	205	---	0.16
	J4	Plastic sandblast	20		112		225			0.39	
	J2	Retarder	31		114		210			0.38	

N/A = not applicable, --- = bad data

Likewise, the load at steel yield was determined based on the smallest load when the steel bars reached the yield strain (i.e., 2,069 micro-strains for 60-ksi steel) as summarized in Table 9. For each specimen, the maximum load at failure and the deflection at the maximum load are also summarized in Table 9.

As indicated in Table 9, the crack loads for the jointed specimens were slightly smaller than those on the jointless specimens. This was due to the fact that the bond strength at the longitudinal connection interface was less than the normal-strength concrete tensile strength. Additionally, the form liner, Plastic Sandblast, produced the least bond between the normal-strength concrete and the UHPC due to the lack of roughness at the interface.

Table 9 also shows that the yield loads and failure loads on the jointed specimens were slightly less than those on the jointless specimens, respectively. However, the deflections at failure of the jointed specimens were close to those of the jointless specimens. Table 9 also shows that the load-deflection relationships of the jointed specimens were comparable to those of the jointless specimens.

It can be concluded that the longitudinal closure pour connection has good performance at connecting the two deck panels and the strength and ductility of the jointed specimens are comparable to those of the jointless specimens.

The stresses and loads at failure of the specimens as predicted by the FE models were determined based on concrete crushing on the top of specimens for the jointless and jointed specimens as shown in Figure 60(a) and Figure 60(b), respectively.

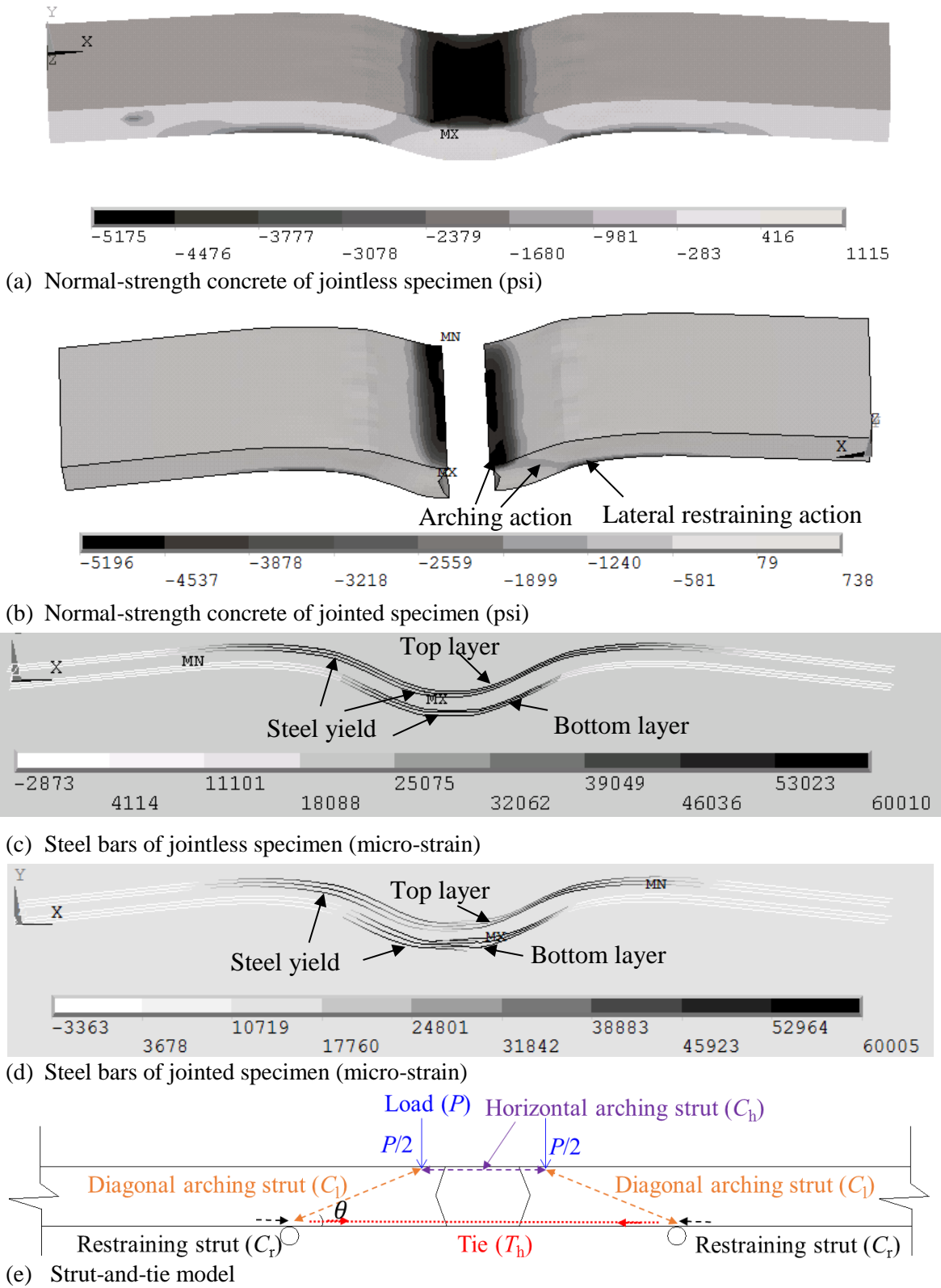


**Figure 60. Stresses in concrete and reinforcing bar at failure predicted by FE models and forces in developed STM model**

That is, the concrete compressive stress exceeds the normal concrete strength of 5,200 psi. The load-strain relationships obtained from FE models were compared with test results and are shown in Figure 59(a) and Figure 59(b). Additionally, the crack loads and yield loads were also determined based on the same approaches used for processing the experimental test results. The load-deflection relationships obtained from FE models were also compared with test results as shown in Figure 59(c). Figure 59 indicates that the relationships for the jointed specimen follow similar patterns to those for the jointless specimens and the predictions from the FE models indicate a higher stiffness and less ductility as compared to the test results.

Table 9 indicates that cracking and yield loads were slightly over-predicted by the FE models compared to the test results, and the failure deflections were slightly under-estimated. The discrepancies of prediction are due to the following reasons: (1) the smeared crack model utilized in the FE models did not provide accurate prediction on the deformation caused by the cracks and (2) the bond stress-slip relationship between the concrete and steel bars were not taken into account. However, the failure loads predicted using the FE models are in good agreement with the test results as shown in Table 9.

Because the shear span-to-depth ratio, 1.44, is less than 2, the center span falls into a D-region and the load carrying capacity should be evaluated using a strut-and-tie Model (STM). Based on the concrete compressive stress flow shown in Figure 60(a) and Figure 60(b), arching action was found between the two load lines and between the loads and supports, and lateral restraining action was also found at the bottom regions of the first and third spans.

Figure 60(c) and Figure 60(d) indicate that the steel bars were all in tension between the two center supports. For the jointless specimens, the top and bottom layers of steel bars yielded under the loading location and the top layer of steel bars also yielded above the center supports. For the jointed specimens, the bottom layer of steel bars yielded under the loading location and the top layer of steel bars only yielded above the center supports and had an average stress of 32 ksi under the loading location.

An STM was developed based on the FE predictions as illustrated in Figure 60(e). The STM consists of a horizontal arching strut ( $C_h$ ), two diagonal arching struts ( $C_d$ ), and two restraining struts ( $C_r$ ), and a tie ( $T_h$ ). The force in the restraining strut is equivalent to the tension force in the top layer of steel bars above the center supports. The tie force is equal to the tension force in the steel bars between the loading lines. The force in the horizontal arching strut is equal to the sum of the forces in the restraining strut and tie. The angle between the diagonal strut and tie is estimated based on the distance from the center supports to the nearest loading line and the center-to-center distance from the horizontal arching strut to the tie. The estimated ultimate load capacity of the jointless and jointed specimens using the STM are 225 and 205 kips respectively, which agree well with the test results and FE predictions shown previously in Table 9.

Due to arching action in the deck, a viable design approach using strut-and-tie methodologies rather than pure flexural bending methodologies may be utilized. In this approach, variable beam spacings can be strategically utilized in designs requiring such geometries making it possible for

the designer to limit tension in the longitudinal joint by inducing large compressive arching forces.

### *FE Modeling of Transverse Joints*

The steel beams and compression block were both modeled using a four-noded shell element with three translational and three rotational degrees of freedom at each node. An elastic-plastic uniaxial material model including bilinear kinematic hardening was used for the steel. The yield strength, elastic modulus, and Poisson's ratio of the steel were set to 50 ksi, 29,000 ksi, and 0.3, respectively. The strain hardening modulus was set to 5% of the elastic modulus. The concrete deck and diaphragm were modeled using an eight-noded solid element, which has three translational degrees of freedom at each node and incorporates cracking and crushing capabilities. The concrete material properties were assigned with multi-linear isotropic hardening in combination with the von Mises yield criterion. The stress-strain relationship of the concrete proposed by Hognestad (1951) was utilized for the concrete constitutive model:

$$f_c = f_c' \left[ 2 \left( \frac{\varepsilon}{\varepsilon_o} \right) - \left( \frac{\varepsilon}{\varepsilon_o} \right)^2 \right] \quad (8)$$

where,  $f_c$  and  $\varepsilon$  are stress and strain on concrete respectively; and strain at peak stress ( $\varepsilon_o$ ) is expressed as follows (Wee et al. 1996):

$$\varepsilon_o = 0.00078(f_c')^{1/4} \quad (\text{in MPa}) \quad (9)$$

The smeared fixed crack model and Rankine maximum stress criterion were utilized to determine the initiation and development of concrete cracking. According to the AASHTO LRFD Bridge Design Specifications (AASHTO 2015), maximum concrete tensile strength can be derived by the following:

$$f_t' = 0.63\sqrt{f_c'} \quad (\text{in MPa}) \quad (10)$$

The steel bars were modeled using a uniaxial tension-compression element with three translational degrees of freedom at each node. An elastic-plastic uniaxial material model was used for the steel. The yield strength, elastic modulus, Poisson's ratio, and tangent modulus of the steel were set to 60 ksi, 29,000 ksi, 0.3, respectively, and 5% of the elastic modulus.

The steel bars were perfectly connected to the concrete through sharing of common nodes. The concrete diaphragm was also perfectly connected to the steel beams and compression block through sharing of common nodes. The shear studs between the concrete deck and the steel beams were modeled using a unidirectional spring element, which can incorporate a nonlinear generalized force-deflection relationship. The spring element was active along the slip direction,

and the other two directions of the two nodes were coupled together. The shear force-slip relationship proposed by Ollgard et al. (1971) was incorporated in the spring element and can be expressed as:

$$Q = Q_n (1 - e^{-18s})^{\frac{2}{5}} \quad (11)$$

where,  $Q$  = shear force in a shear stud,  $s$  = slip at the weld point of the stud, and, according to AASHTO (2010), nominal shear resistance,  $Q_n$ , is determined by:

$$Q_n = 0.5A_{sc} \sqrt{f_c E_c} \leq F_u A_{sc} \quad (12)$$

where,  $A_{sc}$  = cross-sectional area of the stud;  $f_c$  = compressive strength of concrete;  $E_c$  = elastic modulus of the concrete;  $F_u$  = minimum specified tensile strength of the stud (60 ksi).

Due to the symmetry of the geometry, loading, and boundary conditions, a half model was established as shown in Figure 61.

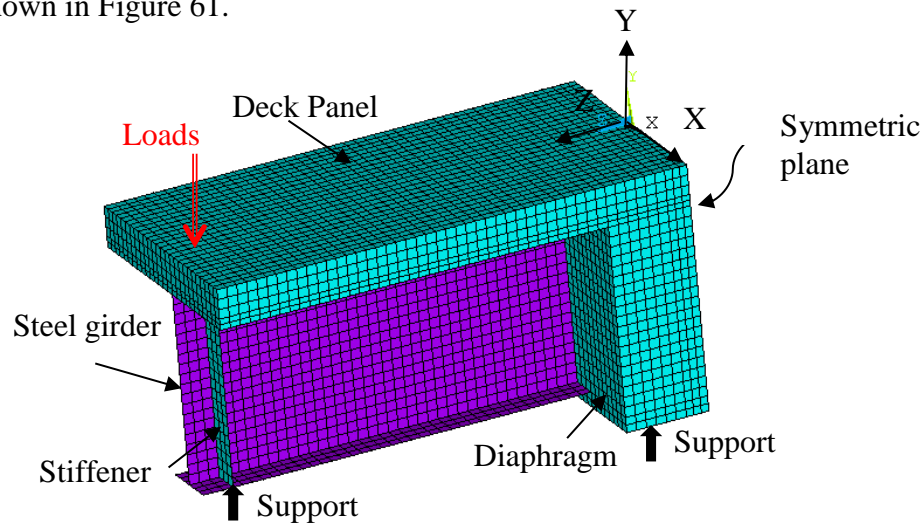


**Figure 61. Finite element model of specimens**

Loads were applied on the nodes of each FE model at the loading location. Boundary conditions were defined taking into account both geometric symmetry at the symmetric sections and simply supported condition at the support locations. Convergence criteria and tolerances were set for the displacement and force. The same strategies of FE modeling as used for the longitudinal joints were utilized to facilitate convergent computations.

#### *Comparisons of Measured and Predicted Results for Transverse Joints*

As presented in the laboratory testing section, load-strain relationships for the steel bars were developed based on the measured strains in the gauges for the two specimens. Typical load-strain relationships for the cross-sections at the edge and the center of the diaphragm are illustrated in

Figure 62. For each load-strain relationship, a plateau can be observed at an early loading stage due to the initiation of concrete cracking.

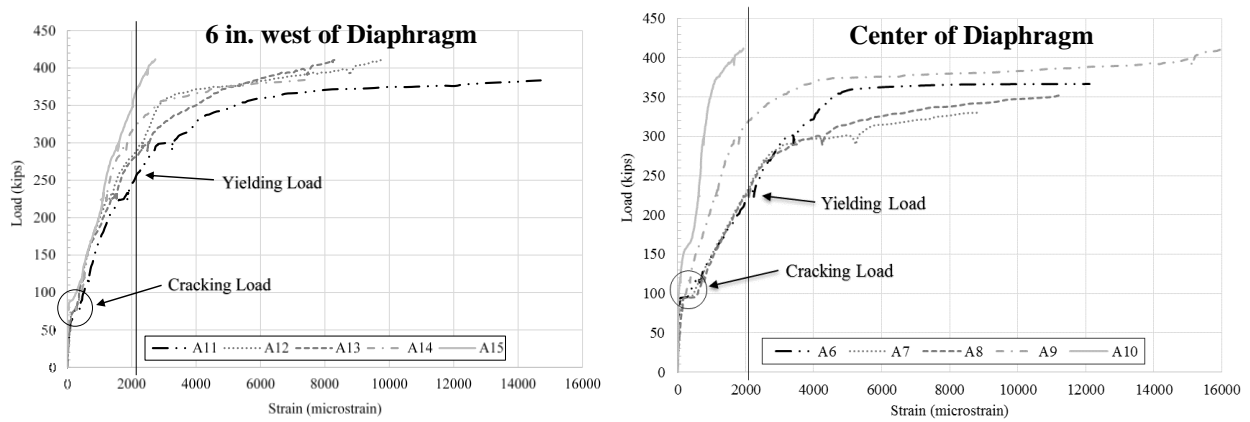


**Figure 62. Strains in steel bars - Specimen I**

For each specimen, the load at concrete cracking was determined based on the smallest plateau of the load-strain relationships. Likewise, the load at steel yield was determined based on the smallest load when the steel bars reached the yield strain (i.e., 2,069 micro-strains for 60-ksi steel). For each specimen, the failure load was determined to be the maximum load applied to the specimen. For consistency and comparison purposes, the cracking load, yielding load, and failure load for each specimen were further converted to the cracking moment, yielding moment, and ultimate moment, respectively, with respect to the location at the diaphragm center, which are summarized in Table 10.

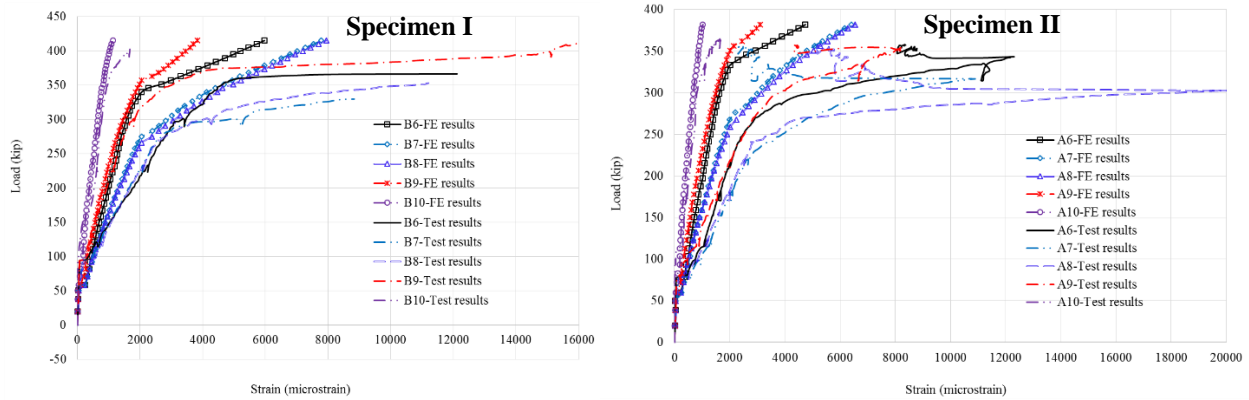
**Table 10. Summary of results**

Specimen No.	Bridge Girder Demand		Test Results			FE Predictions			Hand Calculations	
	Unfactored Service Moment (kip-ft)	Factored Ultimate Moment (kip-ft)	Cracking Moment (kip-ft)	Yielding Moment (kip-ft)	Ultimate Moment (kip-ft)	Cracking Moment (kip-ft)	Yielding Moment (kip-ft)	Ultimate Moment (kip-ft)	Cracking Moment (kip-ft)	Ultimate Moment (kip-ft)
I	816	1428	423	1456	2672	325	1729	2697	348	2136
II			358	1183	2434	325	1684	2482	348	2028

All moments refer to the location at the diaphragm center

The failure load of each specimen as predicted by the FE model was determined based on concrete crushing in the compression region of the critical section of the diaphragm. Note that, for Specimen I, the critical section was located at the interface between the steel girder end and the compression block; for Specimen II, the critical section was located at the steel girder end, which was embedded within the diaphragm. Concrete crushing was determined based on the longitudinal compressive strain in the critical section exceeding 0.003 as shown later in Figure 66(a).

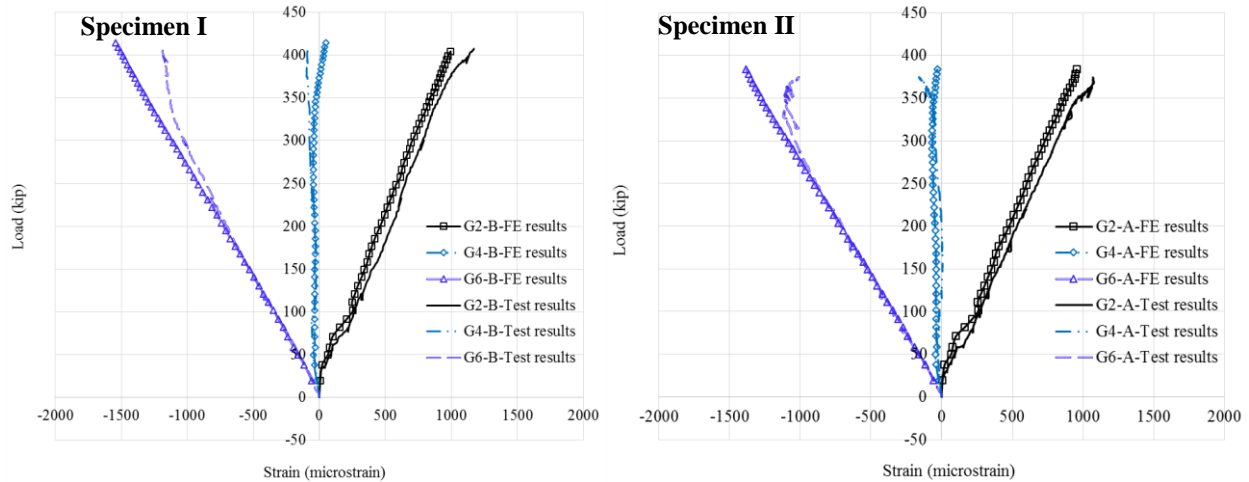
Note the limit state was based on the theoretical values (e.g., concrete crushing strain of 0.003) instead of the tested properties, and this approach is reasonable for the purposes of relative comparisons with design calculations. The load-strain relationships for the steel bars at the diaphragm center obtained from the FE models were compared with the test results and are shown in Figure 63.



**Figure 63. Strain comparison in steel bars at the diaphragm center**

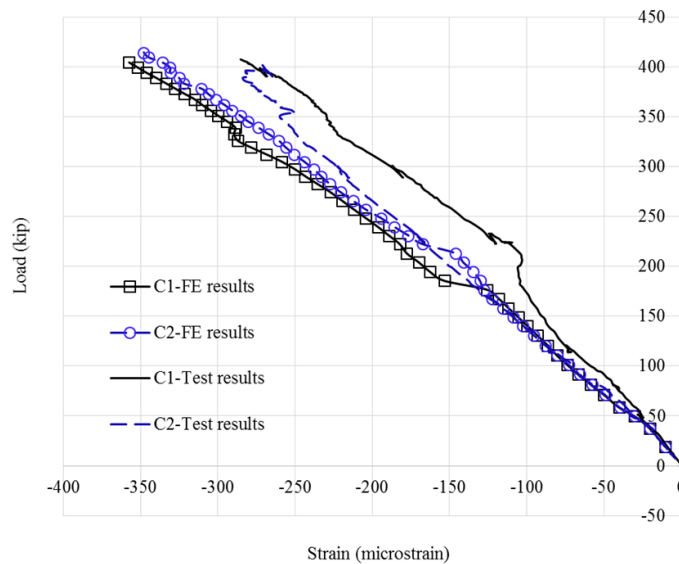
The other load-strain relationships for the steel bars showed similar patterns but are omitted in the interest of brevity. The cracking load and yielding load applied to the FE models were also determined based on the same approaches used for processing the experimental test results. Figure 63 indicates that the predictions from the FE models follow trends similar to those obtained from the test results; however, the FE models show a higher stiffness and less ductility.

Table 10 also indicated that cracking and yielding moments were slightly under-estimated and over-predicted by the FE models compared to the test results, respectively. The discrepancies in the prediction were due to the following: the smeared crack model utilized in the FE models did not provide accurate prediction of the deformation caused by the cracks, and the bond stress-slip relationships between the concrete and steel bars, between the concrete and steel girders, and between the concrete and compression block were not taken into account. However, the ultimate moments of the two specimens predicted using the FE models were in good agreement with the test results as shown in Table 10. Furthermore, the load-strain relationships for the steel girders predicted using the FE models were in good agreement with the test results as shown in Figure 64.



**Figure 64 .Strains in steel girders 6 in. from diaphragm**

Other load-strain relationships for the steel girders showing similar patterns were omitted for brevity. And, the load-strain relationships for the compression block predicted using the FE model compared well with the test results as shown in Figure 65. Consequently, the adequacy of the FE models was verified for representing the structural behavior of two transverse connections.



**Figure 65. Strain comparison in compression block**

The axial stress in the steel bars of the two specimens were extracted from the FE models as shown in Figure 66(b). Figure 66(b) indicates that the stress in steel bars gradually increases from girder ends to the diaphragm center, most of steel bars yielded at the ultimate state, and the stress in some steel bars was much higher than 50 ksi due to strain-hardening. Figure 66(c) shows the von Mises stress in steel girders of the two specimens.

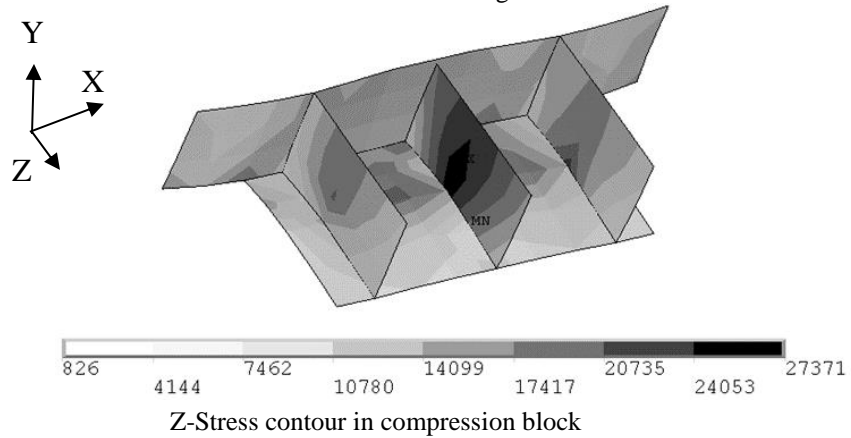
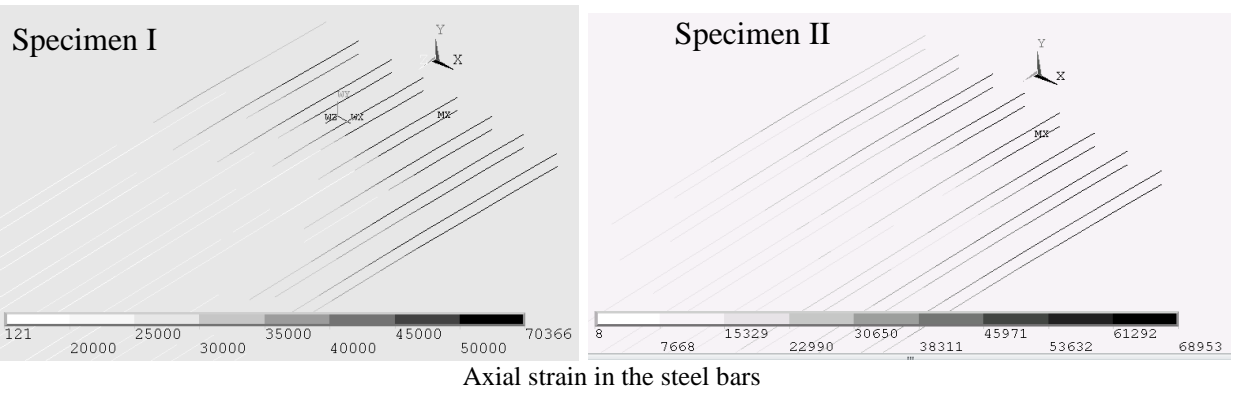
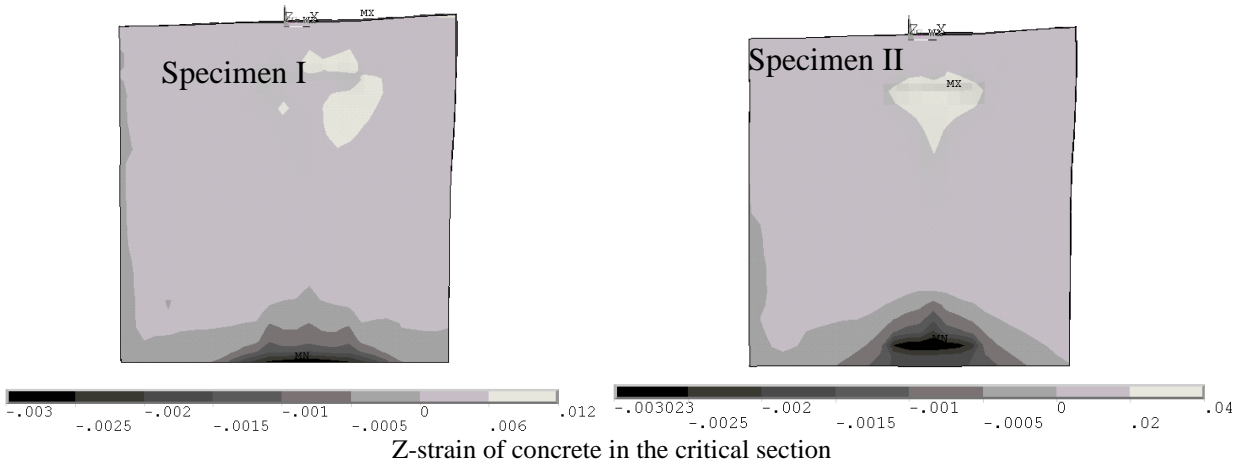


**Figure 66. Strains or stress in different components of specimens**

The steel yielded at the bottom flange in the vicinity of the edge of the diaphragm but most of the steel of the steel girder did not yield as shown in Figure 66(c), which verifies the conclusion that, for the two specimens, the critical section was located at the girder end within the diaphragm.

The longitudinal compressive stress in the compression block is plotted in Figure 66(d). Figure 66(d) indicates that the compression block transferred a significant amount of compression force at the bottom region of the diaphragm, and the steel of the compression block did not yield under the ultimate load. And, due to influence of the compression block, for Specimen I, the maximum compression strain was located at the bottom of the concrete diaphragm, while, for Specimen II, the maximum compression strain in the concrete diaphragm was located in the vicinity of the steel girder bottom flange.

For Specimen I, the centroid of the compression force at the bottom region of the diaphragm was assumed at the bottom of the bottom flange of the steel girders. For Specimen II, the neutral axis was located at 10.9 in. from the diaphragm bottom as shown in Figure 66(a). For conservative consideration, hand calculations of the ultimate capacity for Specimen II were based on the classic reinforced concrete design theory and an effective width equal to the bottom flange width of the steel girder. The hand calculations resulted in a compression depth 10.5 in., which was close to that predicted using the FE model (i.e., 10.9 in.).

For both specimens, the tension force was estimated based on the yield strength of the steel bars. According to force equilibrium and the moment arm between the tension and compression forces, the ultimate moments for the two specimens were estimated as summarized in Table 10. The crack moments for the two specimens were calculated based on the classic reinforced concrete beam design theory and are also summarized in Table 10. Additionally, the conventional design of the Little Silver Creek Bridge according to the AASHTO LRFD bridge design specifications (AAHSTO 2015), the bridge girder demand, including the unfactored service moment and factored ultimate moment, were calculated as summarized in Table 10.

The results summarized in Table 10 suggest that Specimen I with a compression block had higher yield and ultimate moment capacity than Specimen II. The FE models under-estimated the cracking moment, over-estimated the yielding moment, and predicted well the ultimate moment when compared with the test results. Specifically, the ultimate moment capacity predicted using FE models showed less than 2% difference when compared with the test results; and the ultimate moment capacity of Specimen I was 10% higher than that of Specimen II due to the compression block.

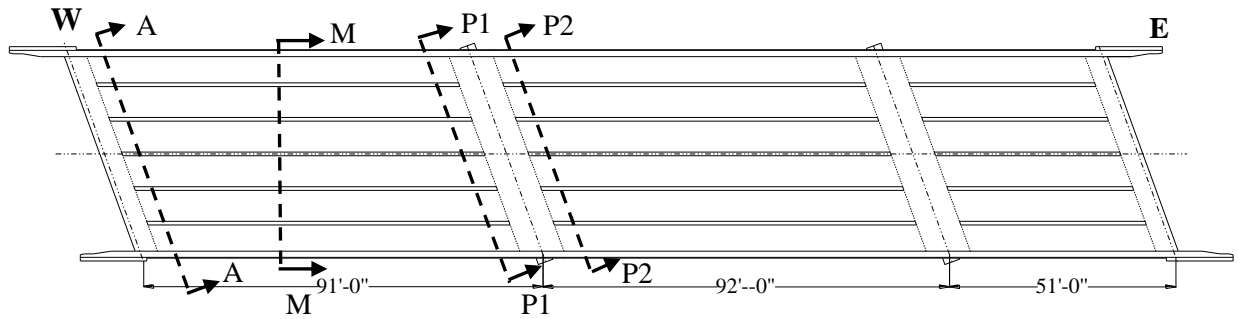
The moment capacity of the two connections were reasonably predicted using hand calculations, although the moment capacities were slightly under-estimated due to the fact that the strain hardening effects of steel were not taken into account. Concrete cracking in the deck of both specimens should occur under both the unfactored service and factored ultimate loads, but the two transverse connections are safe under the factored loads per the AASHTO LRFD bridge design specifications (AAHSTO 2015). Especially, due to the conservative design, Specimen I with a compression block can sustain the entire factored load prior to yield of the deck reinforcement.

## **FIELD TESTING, RESULTS, AND DISCUSSIONS**

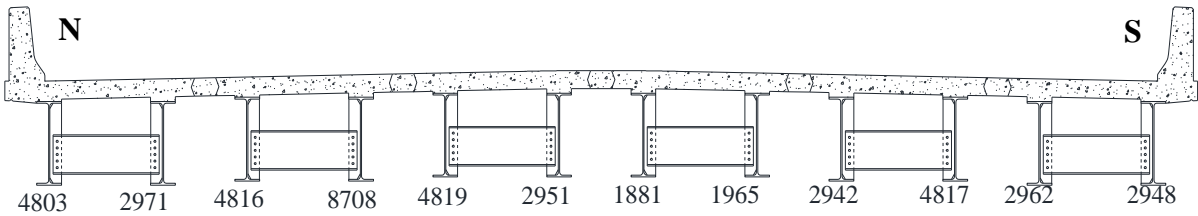
To evaluate the bridge behavior, two on-site, controlled field tests (Test #1 and Test #2) were conducted in December 2015 and October 2016, respectively. The goal of the field testing was to evaluate the span-to-span continuity at the pier locations and the lateral live load distribution of the bridge. Accordingly, the adequacy of the UHPC longitudinal joints between the adjacent prefabricated bridge elements and the HPC transverse joints at the pier locations for prefabricated bridge systems can also be evaluated through investigation of the measured bridge response.

### **Instrumentation and Loading Plan**

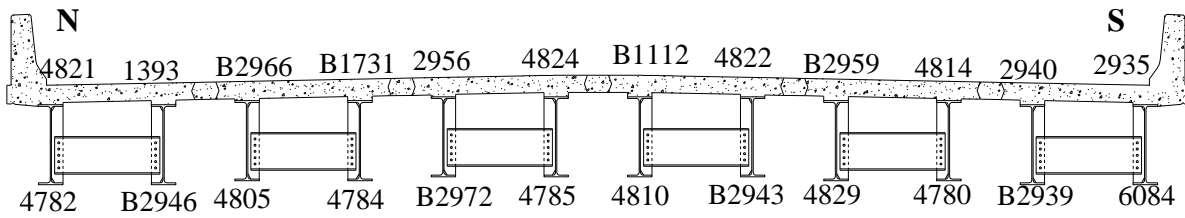
To measure the bridge behavior under live loading, four different cross-sections of the bridge were instrumented to measure its strain response, as shown in Figure 67(a). The four section views provided in Figure 67(a) show the location and number of each section. A represents abutment, M represents mid-span, and P represents pier section. Section A is located 4 ft from the west abutment and Sections P1 and P2 are both located 4 ft from the west pier. The strain gauges were placed on the bottom of the top flanges and the top of bottom flanges of the steel girders. For Test #1, the strain gauges installed at Sections A, M, P1, and P2 are illustrated in Figure 67(b), Figure 67(c), Figure 67(d), and Figure 67(e), respectively.



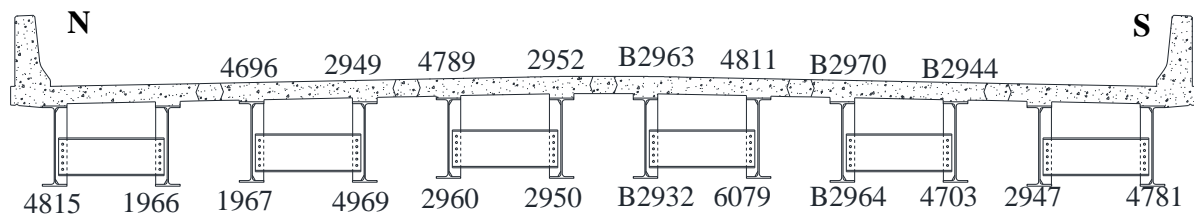
(a) Location of Section Views



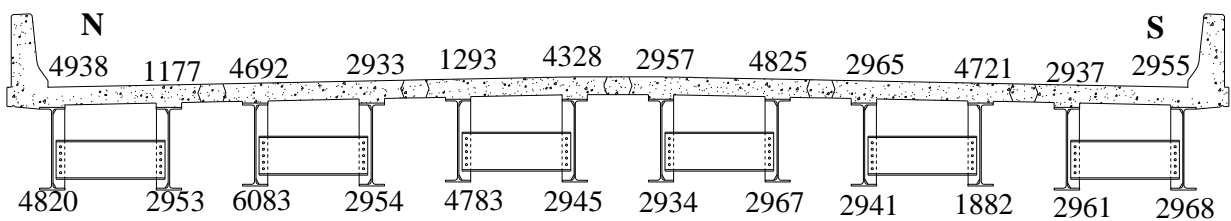
(b) Abutment Strain Gauges Installed-Section A



(c) Mid-Span Strain Gauges Installed-Section M



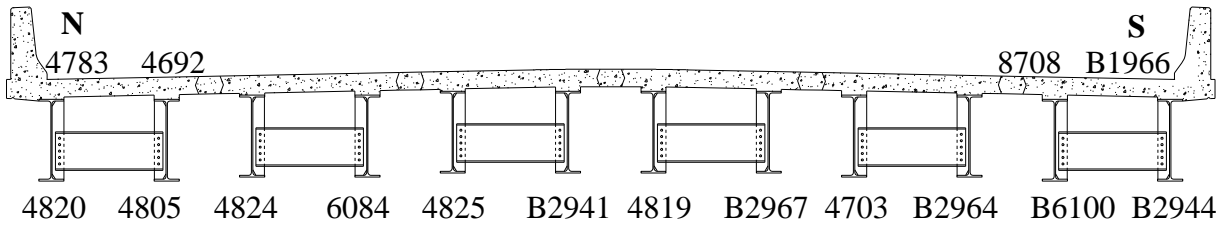
(d) Pier Next to West-Span Gauges Installed-Section P1



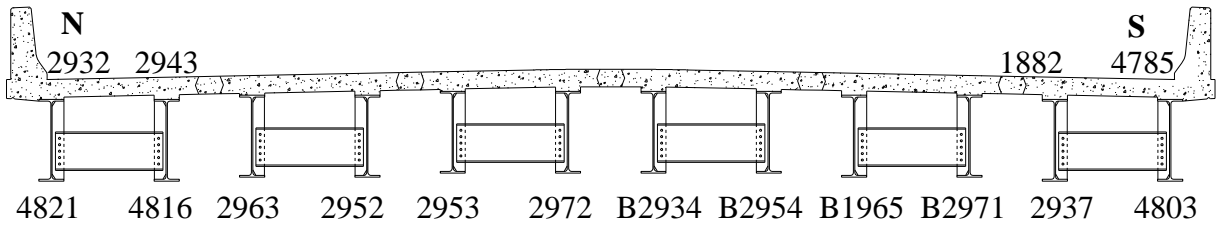
(e) Pier Next to Center Span Gauges Installed-Section P2

**Figure 67 .Strain gauges installed on the bridge-Test #1**

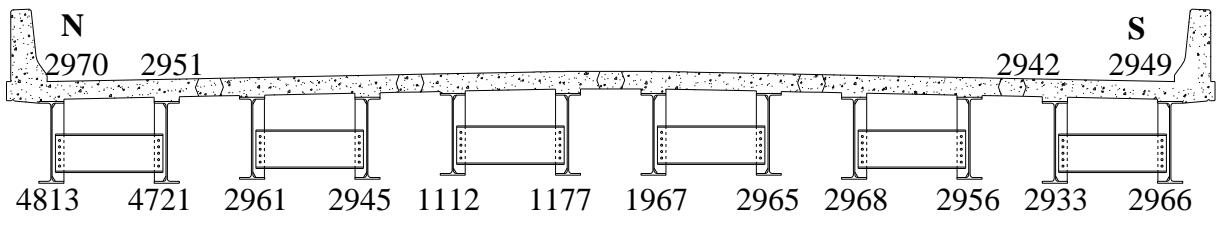
For Test #2, the strain gauges installed at Sections A, M, P1, and P2 are illustrated in Figure 68(a), Figure 68(b), Figure 68(c), and Figure 68(d), respectively.



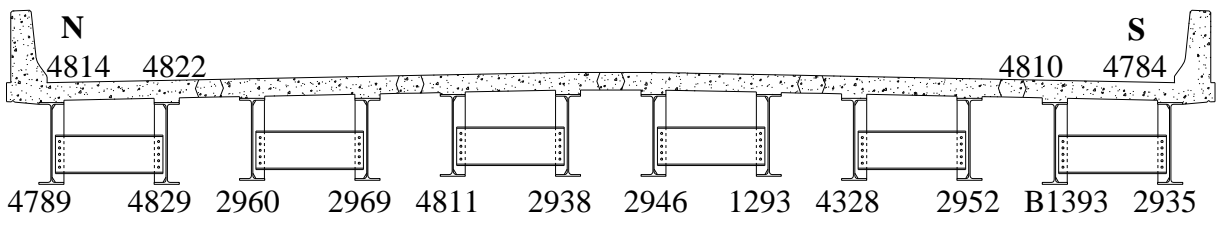
(a) Abutment Strain Gauges Installed–Section A



(b) Mid-Span Strain Gauges Installed–Section M



(c) Pier Next to West-Span Gauges Installed–Section P1



(d) Pier Next to Center Span Gauges Installed –Section P2

**Figure 68 .Strain gauges installed on the bridge-Test #2**

Note that gauges were not placed on every top flange. Eighty and sixty-four strain gauges were utilized for Test #1 and Test #2, respectively.

During testing, live loads were applied to the bridge using a dump truck traveling across the bridge at a crawl speed from west to east. Four load paths were utilized to simulate different load scenarios, as shown in Figure 69.

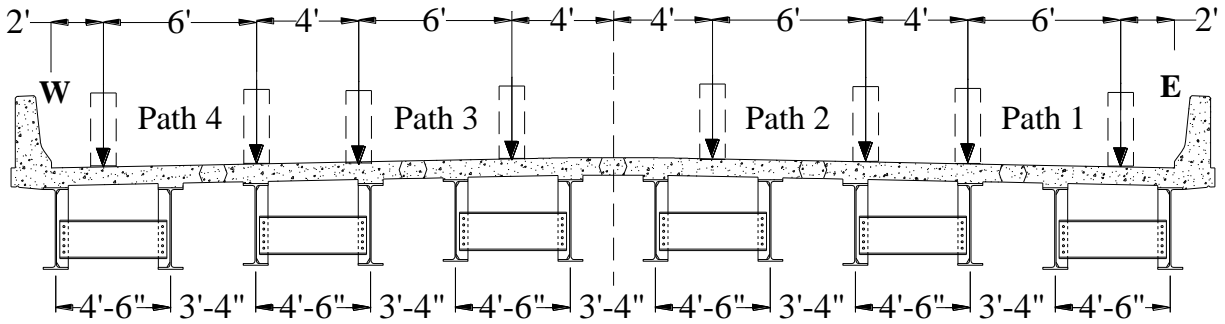


**Figure 69. Load paths on the bridge**

Load Path 1 or 4 represents the loading scenario with the exterior wheel line center located 2 ft from the inside of the barrier. Load Path 1 plus 2 or 4 plus 3 represents the loading scenario with two side-by-side trucks spaced at 4 ft on the bridge. Two passes were conducted for each load path. The configurations of the dump trucks used during Test #1 and Test #2 are shown in Figure 70(a) and Figure 70(b), respectively.

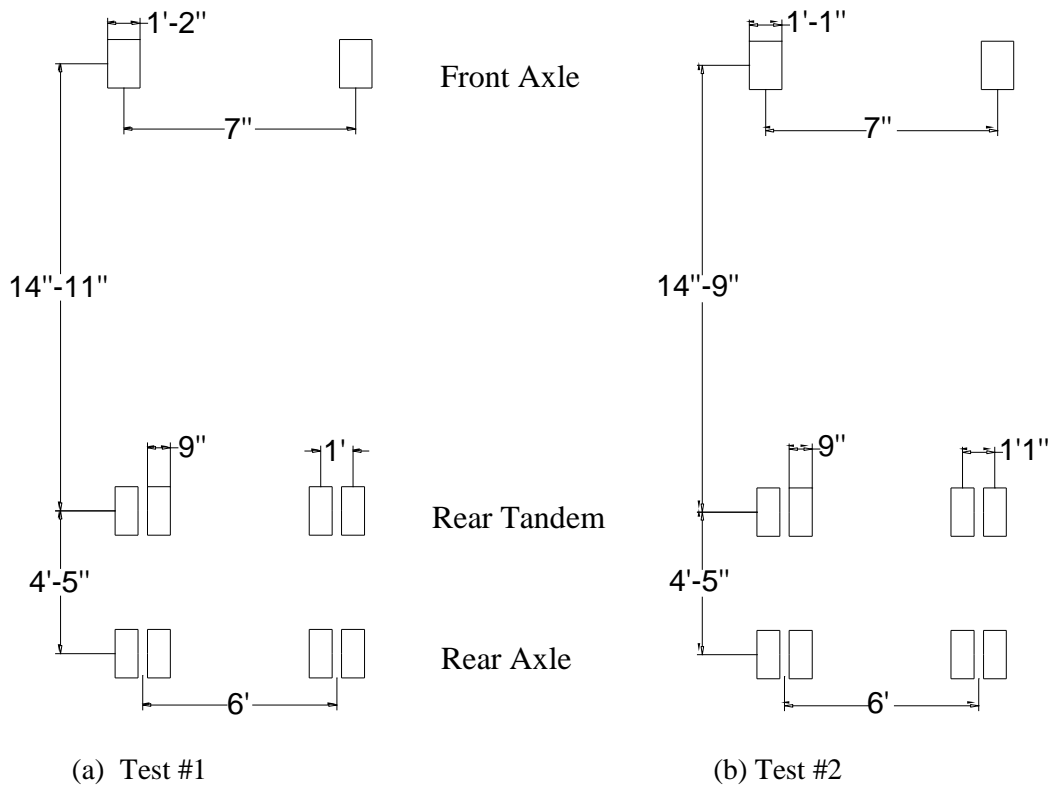


**Figure 70. Configurations of dump trucks for Test #1 and Test #2**

The dump trucks were three-axle trucks (front, rear tandem, and rear) with the dimensions and axle and wheel-line spacing shown in Figure 70. The gross weight and each axle weight for the two tests are summarized in Table 11.

**Table 11. Dump truck weight details**

	<b>Gross weight (lbs)</b>	<b>Front Axle (lbs)</b>	<b>Rear Tandem (lbs)</b>	<b>Rear Axle (lbs)</b>
Test #1	41,400	15,400	12,700	13,300
Test #2	40,460	13,600	13,430	13,430

**Live Load Distribution Factors**

For steel girder bridges, the moment load distribution factor (LDF) of one-lane loads for interior beams per lane can be determined by the following equation (AASHTO 2010):

$$LDF_{interior} = 0.06 + \left(\frac{S}{14}\right)^{0.6} \left(\frac{S}{L}\right)^{0.2} \left(\frac{K_g}{12.0Lt_s^3}\right)^{0.1} \quad (13)$$

where,  $S$  = girder spacing (ft),  $L$  = span length (ft),  $t_s$  = deck thickness (in.), and  $K_g$  = longitudinal stiffness parameter, which can be expressed by:

$$K_g = n(I + Ae_g^2) \quad (14)$$

where,  $A$  = area of beam,  $I$  = moment of inertia of beam (in.<sup>4</sup>),  $e_g$  = vertical distance between the centroids of the beam and deck (in.), and  $n$  = stiffness ratio of beam material to deck concrete.

The moment LDFs of two-lane loads for interior beams per lane can be determined by the following equation (AASHTO 2010):

$$LDF_{interior} = 0.075 + \left(\frac{S}{9.5}\right)^{0.6} \left(\frac{S}{L}\right)^{0.2} \left(\frac{K_g}{12.0Lt_s^3}\right)^{0.1} \quad (15)$$

The moment LDFs of exterior beams can be determined by the product of those of interior beams and the correction factor, ( $e$ ), and  $e$  can be expressed by:

$$e = 0.77 + \frac{d_e}{9.1} \quad (-1.0 \leq d_e \leq 5.5) \quad (16)$$

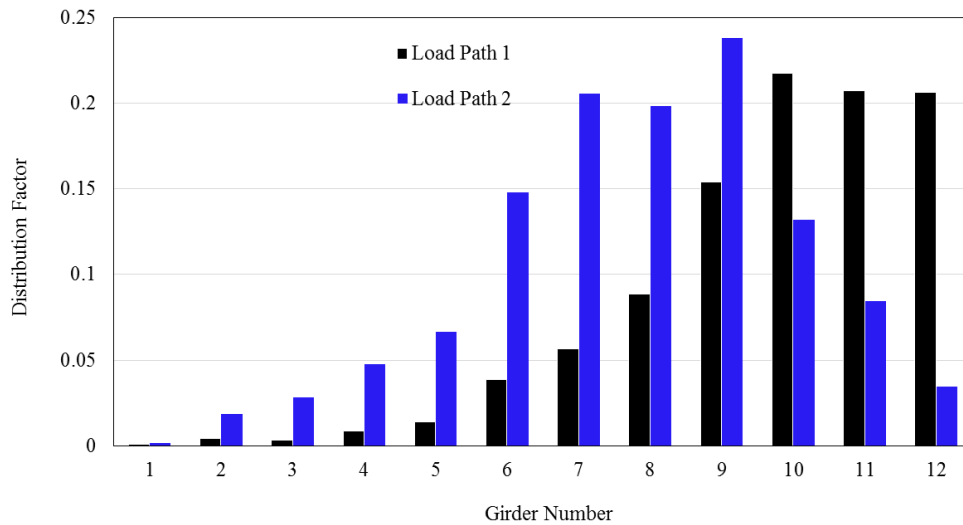
where,  $d_e$  = horizontal distance from the centerline of exterior web of exterior beam to the inside surface of barrier.

Experimentally, the LDF for each girder can be determined by:

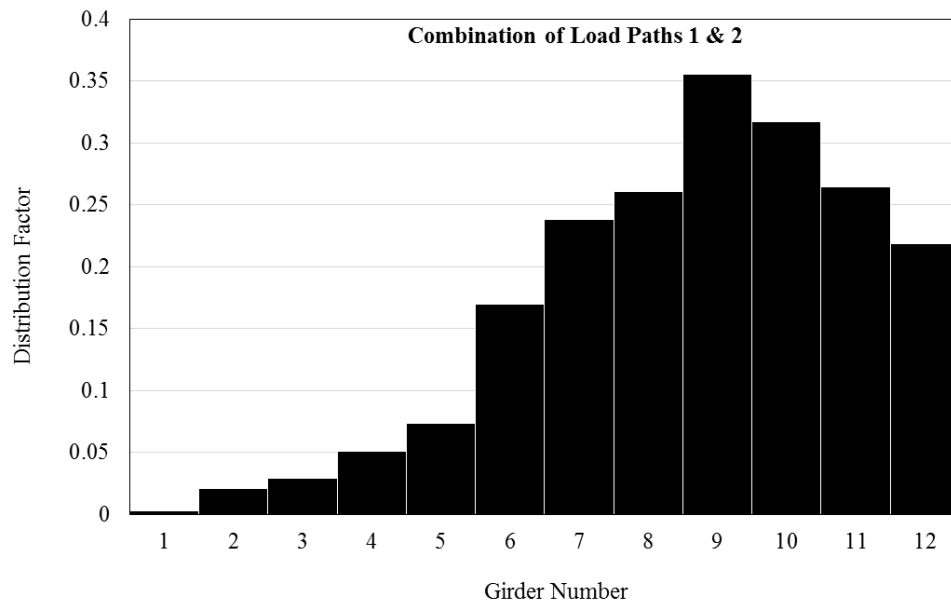
$$DF_i = \frac{\varepsilon_i}{\sum_i \varepsilon_i} \quad (17)$$

where,  $\varepsilon_i [i=1, 2, 3, \dots]$  = longitudinal strain component in girder  $i$ . The strains measured from the field tests were directly utilized to derive LDFs for different girders.

The experimentally determined LDFs at bridge Section M for Load Paths 1 and 2 are shown in Figure 71.



(a) One-Truck Load



(b) Two-Truck Load

**Figure 71. Derived LDFs at Section M for Load Paths 1 and 2**

Figure 71(a) illustrates the LDFs for the 12 girders subject to the truck loading through Load Path 1 or 2, representing a one-lane loading scenario. Figure 71(b) illustrates the LDFs for the 12 girders subject to the truck loading through the combination of Load Paths 1 and 2, representing a two-lane loading scenario. Figure 71 indicates that the LDFs of the girders in the vicinity of the truck loading are larger, and the LDFs gradually decrease from the truck loading location to the location away from the truck loading. Following the same approach, LDFs of girders at different bridge cross-sections were derived.

Since the maximum LDF is commonly utilized for conventional bridge designs, maximum LDFs at different bridge cross-sections and under different load paths were calculated for Tests #1 and #2 and are summarized in Table 12 and Table 13, respectively.

**Table 12. Maximum LDFs at different bridge cross-sections and under different load paths – Test #1**

Cases		Maximum LDFs	
		Interior Girders	Exterior Girders
Section M (Mid-Span)	Load Path 1	0.217	0.206
	Load Path 2	0.238	0.034
	Load Paths 1&2	0.356	0.219
	Load Path 3	0.207	0.039
	Load Path 4	0.219	0.213
	Load Paths 3&4	0.339	0.239
Section P1 (Pier)	Load Path 1	0.296	0.194
	Load Path 2	0.241	0.086
	Load Paths 1&2	0.413	0.157
	Load Path 3	0.220	0.085
	Load Path 4	0.267	0.290
	Load Paths 3&4	0.369	0.295
Section P2 (Pier)	Load Path 1	0.231	0.287
	Load Path 2	0.293	0.039
	Load Paths 1&2	0.431	0.220
	Load Path 3	0.262	0.095
	Load Path 4	0.276	0.261
	Load Paths 3&4	0.397	0.241

**Table 13. Maximum LDFs at different bridge cross-sections and under different load paths – Test #2**

Cases		Maximum LDFs	
		Interior Girders	Exterior Girders
Section M (Mid-Span)	Load Path 1	0.233	0.231
	Load Path 2	0.229	0.076
	Load Paths 1&2	0.396	0.282
	Load Path 3	0.195	0.041
	Load Path 4	0.267	0.236
	Load Paths 3&4	0.364	0.261
Section P1 (Pier)	Load Path 1	0.254	0.277
	Load Path 2	0.228	0.100
	Load Paths 1&2	0.376	0.223
	Load Path 3	0.262	0.077
	Load Path 4	0.271	0.273
	Load Paths 3&4	0.332	0.267
Section P2 (Pier)	Load Path 1	0.349	0.364
	Load Path 2	0.250	0.082
	Load Paths 1&2	0.458	0.336
	Load Path 3	0.271	0.113
	Load Path 4	0.239	0.261
	Load Paths 3&4	0.387	0.213

To make comparisons between the LDFs calculated using the test data and the AASHTO LRFD equations (AASHTO 2010), the maximum LDFs for the interior and exterior girders at the positive and negative moment regions were summarized and are shown in Table 14 and Table 15 for Tests #1 and #2, respectively.

**Table 14. Comparisons of LDFs with those estimated using AASHTO LRFD equations – Test #1**

Cases		Interior Girders		Exterior Girders	
		Test Results	AASHTO LRFD Equations	Test Results	AASHTO LRFD Equations
One-Lane Load	Positive Moment Region	0.238	0.268	0.213	0.211
	Negative Moment Region	0.296	0.268	0.290	0.211
Two-Lane Load	Positive Moment Region	0.356	0.353	0.239	0.278
	Negative Moment Region	0.431	0.353	0.295	0.278

**Table 15. Comparisons of LDFs with those estimated using AASHTO LRFD equations – Test #2**

Cases		Interior Girders		Exterior Girders	
		Test Results	AASHTO LRFD Equations	Test Results	AASHTO LRFD Equations
One-Lane Load	Positive Moment Region	0.267	0.268	0.236	0.211
	Negative Moment Region	0.349	0.268	0.364	0.211
Two-Lane Load	Positive Moment Region	0.396	0.353	0.282	0.278
	Negative Moment Region	0.458	0.353	0.336	0.278

Note that one-lane and two-lane load cases were taken into account in order to closely compare with the results calculated using the AASHTO LRFD equations. Table 14 and Table 15 indicate that, for the same girder cross-section and region, the LDFs derived for the two-lane load cases were generally larger than those derived for the one-lane load cases.

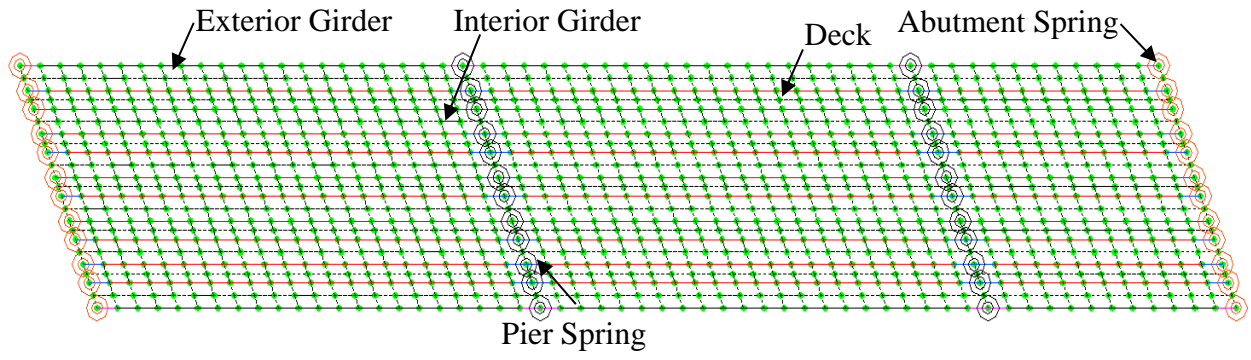
Table 14 and Table 15 indicate that the LDFs in the positive moment region are close to the values estimated using the AASHTO LRFD equations; however, the LDFs at the negative moment region are slightly larger than the values estimated using the AASHTO LRFD equations.

This is possibly due to the fact that, in the positive moment region, the bridge cross-section is perpendicular to the girder line while, in the negative moment region, the bridge cross-section is parallel to the bridge skew. Also, another reason is that the girder spacing is not constant for all girders, but the AASHTO LRFD equations are only applicable to constant girder spacing scenarios.

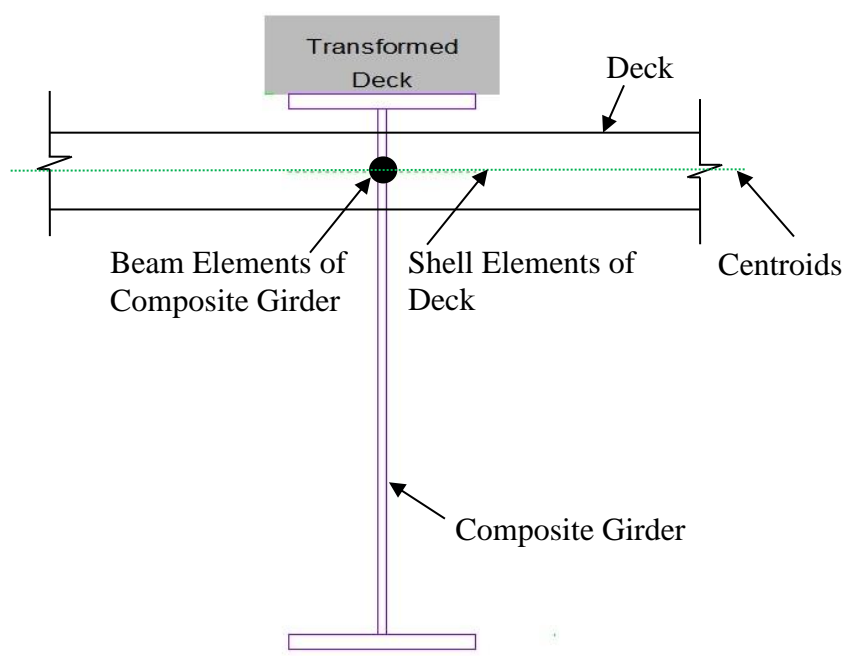
For this study, the average girder spacing was utilized in the AASHTO LRFD equations. In sum, the LDFs based on test data are reasonably compared with those calculated using the AASHTO LRFD equations.

### **FE Modeling of Little Silver Creek Bridge**

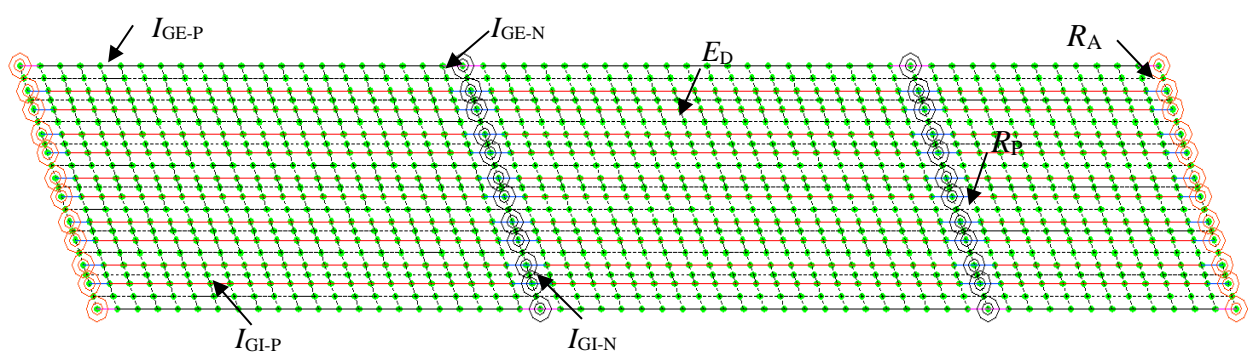
An FE model of the Little Silver Creek Bridge was established as shown in Figure 72(a). The girders and diaphragms were modeled using two-node beam elements, which have three translational and three rotational degrees of freedom at each node. The deck was modeled using four-node quadrilateral shell elements, which have three translational and three rotational degrees of freedom at each node and only incorporates bending behavior (ignoring tension membrane behavior). The restraint to girders at the abutment and pier supports is modeled using spring elements.



(a) Bridge Model and Sensors



(b) Modeling of Girder and Deck



(c) Optimized Bridge Parameters

**Figure 72. Details of Little Silver Creek Bridge FE model**

As shown in Figure 72(b), the beam elements of girders share the common nodes with the deck shell elements at the centroid locations. The composite section of the girder incorporating the transformed deck was utilized for the section properties of each beam element. The diaphragms only shared the common nodes with the girder elements at the connection locations. Linear elastic material models were used for the concrete and steel.

To calibrate the established FE model, a set of bridge parameters that correlated significantly to the bridge response were selected for the model optimization process. The common bridge parameters consisted of the moments of inertia of girders and diaphragms, the elastic modulus of the deck, and the spring constants at supports. For the Little Silver Creek Bridge, the seven bridge parameters included during model calibration included the moment of inertia of the exterior girder cross-sections in the positive moment region ( $I_{GE-P}$ ), the moment of inertia of the exterior girder cross-sections in the negative moment region near piers ( $I_{GE-N}$ ), the moment of inertia of the interior girder cross-sections in the positive moment region ( $I_{GI-P}$ ), the moment of inertia of the interior girder cross-sections in the negative moment region near piers ( $I_{GI-N}$ ), the modulus of elasticity of the deck ( $E_D$ ), the spring constant at the abutments ( $R_A$ ), and the spring constant at the piers ( $R_P$ ), as illustrated in Figure 72(c).

Various values and calibration ranges are tabulated and summarized in Table 16.

**Table 16. Little Silver Creek Bridge parameter values and ranges**

Parameter	Non-Composite Plan Value	Composite Plan Value	Lower Limit	Upper Limit
$I_{GI-P}$ , in <sup>4</sup>	9,407	25,531	7,055	42,126
$I_{GE-P}$ , in <sup>4</sup>	9,407	25,662	7,055	42,342
$I_{GI-N}$ , in <sup>4</sup>	9,407	25,531	7,055	48,508
$I_{GE-N}$ , in <sup>4</sup>	9,407	25,662	7,055	48,758
$R_A$ , kips-in./rad	1,000,000	1,000,000	0	10,000,000
$R_P$ , kips-in./rad	1,000,000	1,000,000	0	10,000,000
$E_D$ , ksi	5,387	5,387	4,040	6,734

$I_{GI-P}$  = moment of inertia of interior girders in the positive moment region,  $I_{GE-P}$  = moment of inertia of exterior girders in the positive moment region,  $I_{GI-N}$  = moment of inertia of interior girder cross-sections in the negative moment region,  $I_{GE-N}$  = moment of inertia of exterior girders in the negative moment region,  $E_D$  = modulus of elasticity of deck

The initial values of the elastic modulus of the deck were set as plan values, and upper and lower limits were set as 25% higher and 25% lower than the plan values, respectively. Note that the compressive strength of the deck was measured to be 7,896 psi based on cylinder test results. The initial values of the girders were set as plan values considering fully composite actions with deck and railings. The lower limits of the moments of inertia of the girders were set as 25%

lower than plan values considering non-composite action. And the upper limits were appropriately set taking into account the contribution of the UHPC and barrier to the stiffness.

The spring constants for both interior and exterior girders at abutments accounting for support restraint were set to have an initial value of 1,000,000 kip-in/rad, the lower limit of 0 kip-in/rad, and the upper limit of 10,000,000 kip-in/rad. Strains in the girder bottom flanges were utilized during the parameter optimization process. The parameters were calibrated through minimization of the discrepancy of the calculated and measured strain values.

Also note that the approach to estimate the actual centroid position of the girder cross-section is very significant for the accuracy of the calibrated moment of inertia. To realistically evaluate the centroid positions for different types of girder cross-sections, the strain responses in the top and bottom gauges were utilized to estimate the neutral axis location. Based on mechanics of materials, the strain profile is illustrated in Figure 73.

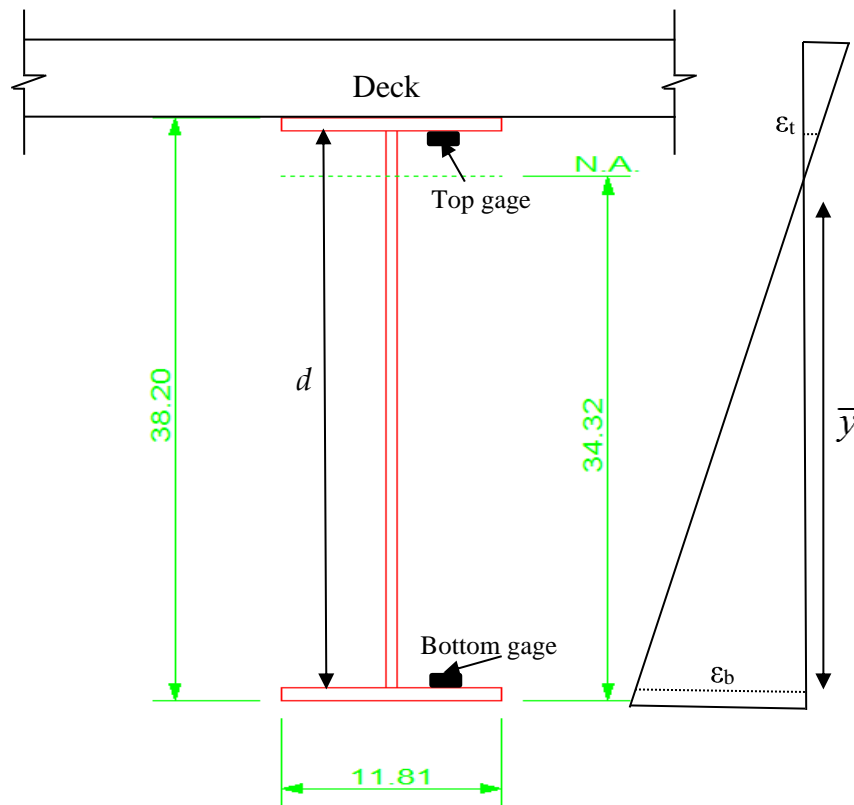


**Figure 73. Sensors on girder cross-section – positive moment region**

The neutral axis location can be derived as shown in Table 17 using the following equation:

$$\bar{y} = \frac{\varepsilon_b}{\varepsilon_b + \varepsilon_t} d \quad (18)$$

where,  $\bar{y}$  = neutral axis location relative to the bottom gauge location;,  $\epsilon_b$  = strain in the bottom gauge,  $\epsilon_t$  = strain in the top gauge, and  $d$  = the distance between the two gauges.

**Table 17. Neutral axis determination at different girder cross-sections**

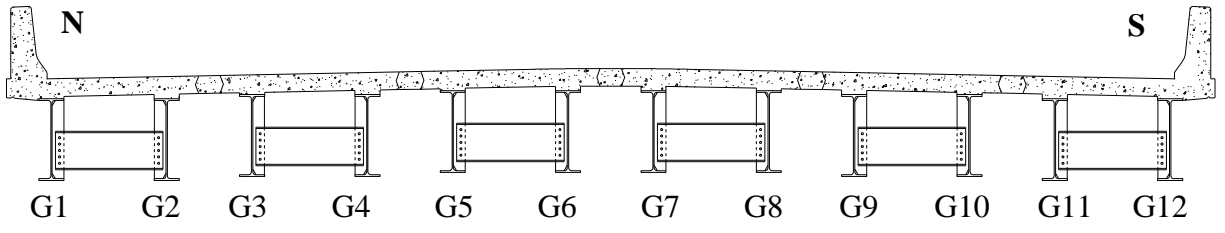
<b>Girder Cross-Sections</b>	<b>Mean (in.)</b>	<b>Standard Deviation (in.)</b>	<b>Minimum Delta Strain (<math>10^{-6}</math>)</b>
<b>Interior Girders in Positive Moment Region</b>	38.79	0.551	20
<b>Exterior Girders in Positive Moment Region</b>	37.65	0.065	20
<b>Interior Girders in Negative Moment Region</b>	37.60	0.606	20
<b>Exterior Girders in Negative Moment Region</b>	38.91	0.149	20

Neutral axis location = Relative to the bottom gauge location, Minimum delta strain = Minimum strain difference between the top and bottom gauges

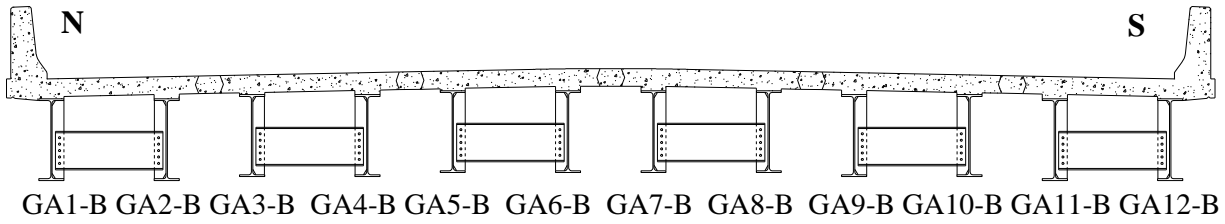
Since the small strains in gauges are not reliable, the minimum delta strain (commonly larger than 10–20 microstrains), which defined the minimum strain difference between the top and bottom gauges, was utilized to choose the strain response for the neutral axis location calculation. Likewise, the neutral axis locations in interior girders in the positive moment region, interior girders in the negative moment region, exterior girders in the positive moment region, and exterior girders in the negative moment region were calculated. The calculated means of neutral axis locations were imported into the FE model as the centroids of the cross-sections of the beam elements for the girders.

### **Analyses and Comparisons of Measured and Predicted Results**

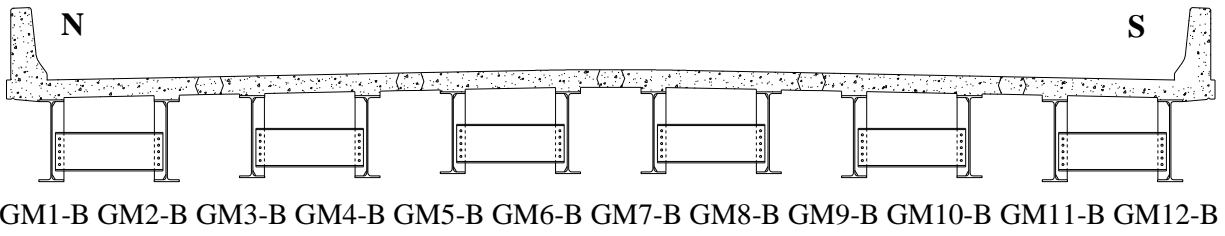
For comparison and illustration purposes, the gauges on the bottom flanges are re-named in Figure 74.



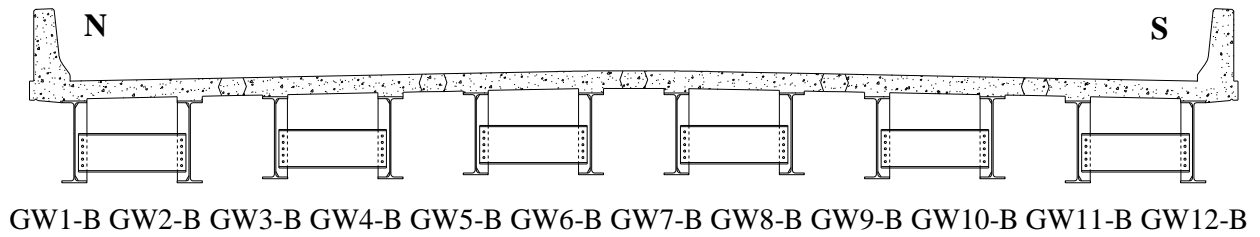
(a) Girder Number



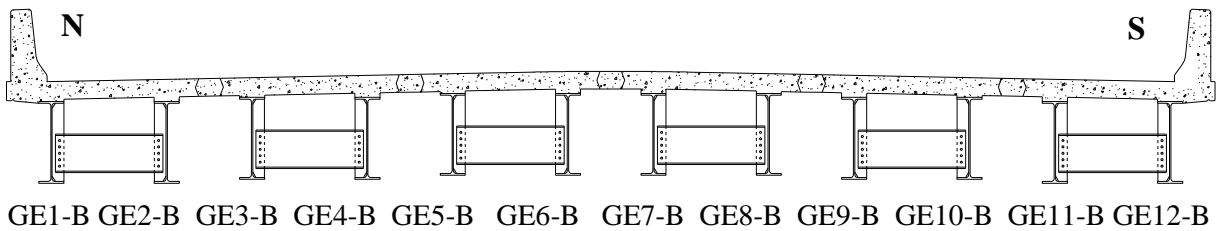
(b) Abutment Strain Gauges Installed–Section A



(c) Mid-Span Strain Gauges Installed–Section M



(d) Pier Next to West-Span Gauges Installed–Section P1



(e) Pier Next to Center Span Gauges Installed –Section P2

**Figure 74. Re-named strain gauges on bottom flanges**

The parameters were calibrated through minimization of the discrepancy between the measured test data and FE results taking into account all load paths from Test #1. As shown in Table 18, the optimized parameter values are generally larger than the initial values based on the information on the bridge plan sheets.

**Table 18. Optimized parameter values**

Parameter	Optimized Value	Initial Value
$I_{GL-P}$ , in <sup>4</sup>	37,240	25,531
$I_{GE-P}$ , in <sup>4</sup>	41,560	25,662
$I_{GL-N}$ , in <sup>4</sup>	43,520	25,531
$I_{GE-N}$ , in <sup>4</sup>	47,780	25,662
$R_A$ , kips-in/rad	9,045,000	1,000,000
$R_P$ , kips-in/rad	7,533,000	1,000,000
$E_D$ , ksi	5,862	5,387

$I_{GL-P}$  = moment of inertia of interior girders in the positive moment region,  $I_{GE-P}$  = moment of inertia of exterior girders in the positive moment region,  $I_{GL-N}$  = moment of inertia of interior girder cross-sections in the negative moment region,  $I_{GE-N}$  = moment of inertia of exterior girders in the negative moment region,  $E_D$  = modulus of elasticity of deck

The higher moments of inertia are mostly due to the extra stiffness contribution from the higher material strength of the HPC and UHPC, larger deck depth and haunch, and the barrier on the bridge. The larger spring constants at both abutment and pier locations are mostly due to the restraint from the supports and closure pours.

Note that the statistical values, percent error (PE), and correlation coefficient (CC), were used to describe the model's ability to represent the actual structure, and can be determined by:

$$PE = \frac{\sum (\varepsilon_R - \varepsilon_C)^2}{\sum \varepsilon_R^2} \quad (19)$$

$$CC = \frac{\sum (\varepsilon_R - \mu_{\varepsilon_R})(\varepsilon_C - \mu_{\varepsilon_C})}{\sum \sqrt{(\varepsilon_R - \mu_{\varepsilon_R})^2 (\varepsilon_C - \mu_{\varepsilon_C})^2}} \quad (20)$$

where,  $\varepsilon_R$  = measured strain;  $\varepsilon_C$  = strain calculated using the FE model;  $\mu_{\varepsilon_R}$  = average recorded strain in each gauge;  $\mu_{\varepsilon_C}$  = average calculated strain in each gauge.

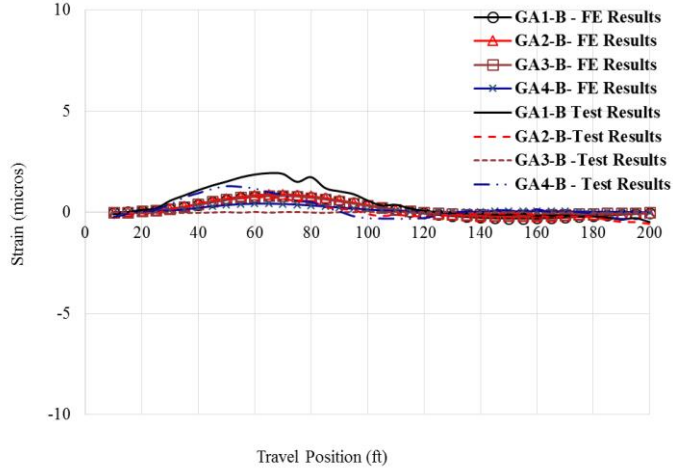
The percent error and correlation coefficient for all load paths and individual load paths for Tests #1 and #2 were summarized and are shown in Table 19. Based on the results shown in Table 19, the predictions from the FE model are in reasonable agreement with the test results.

**Table 19. Statistical values for optimization process**

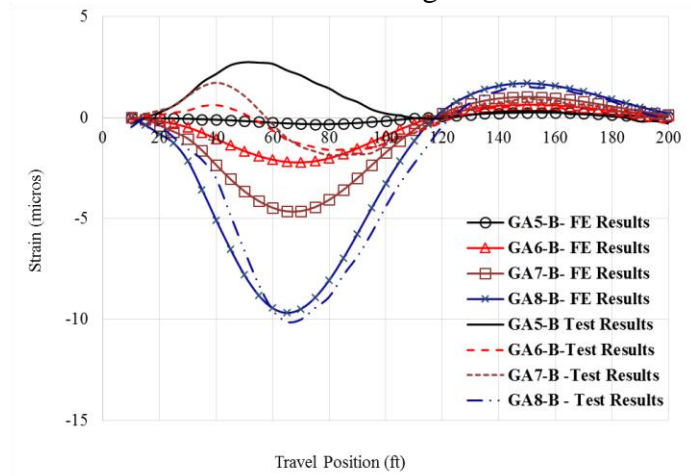
	All Paths		Load Path 1		Load Path 2		Load Path 3		Load Path 4	
	PE	CC	PE	CC	PE	CC	PE	CC	PE	CC
<b>Test #1</b>	12.9%	0.9371	11.9%	0.9582	9.1%	0.9534	16.5%	0.9184	13.9%	0.9461
<b>Test #2</b>	20.3%	0.8958	20.4%	0.9201	19.7%	0.8964	23.1%	0.8901	17.7%	0.9195

PE = percent error, CC = correlation coefficient

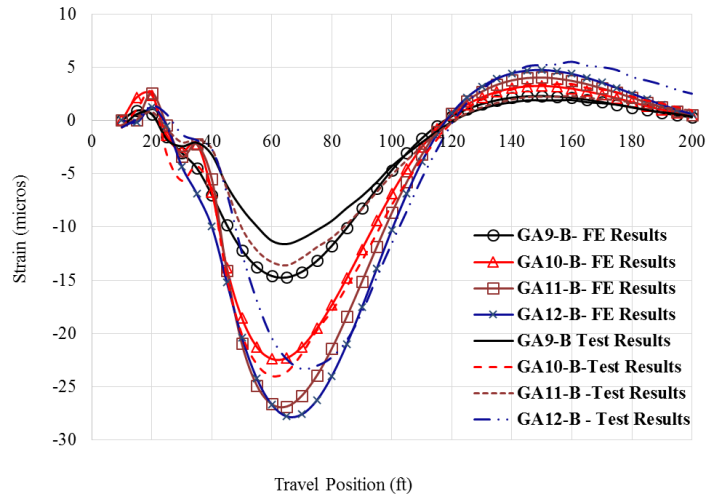
To further demonstrate the adequacy of the FE model, strain responses at different truck travel positions predicted from the FE model were compared with the test results. Load Path 1 was selected to show representative results, and the comparisons are shown in Figure 75 through Figure 78 for the four bridge cross-sections (i.e, Section A, M, P1, and P2).



Girders 1 through 4

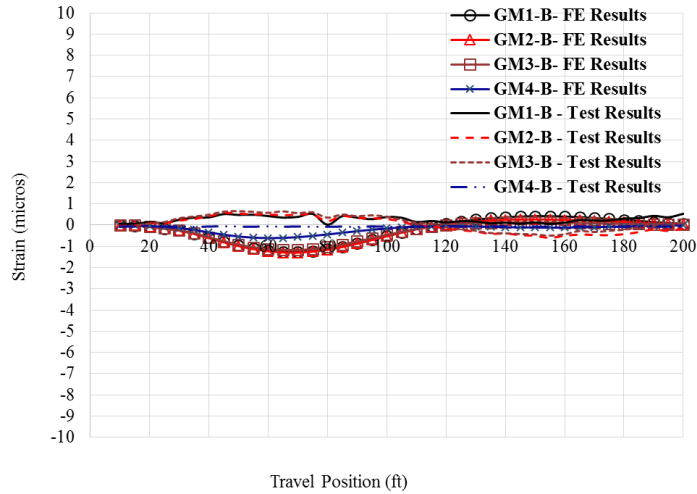


Girders 5 through 8

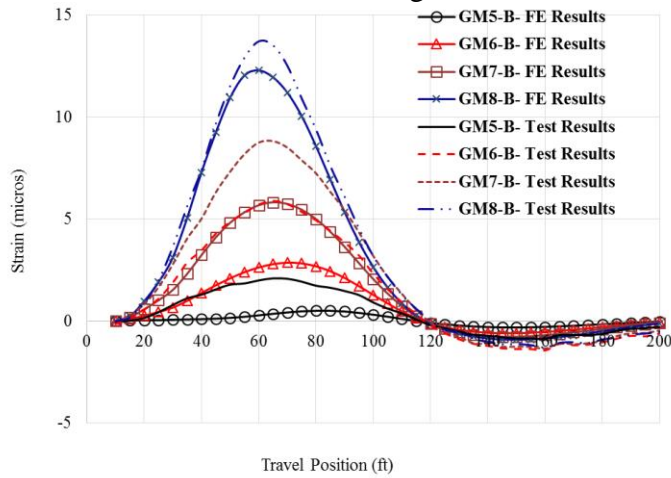


Girders 9 through 12

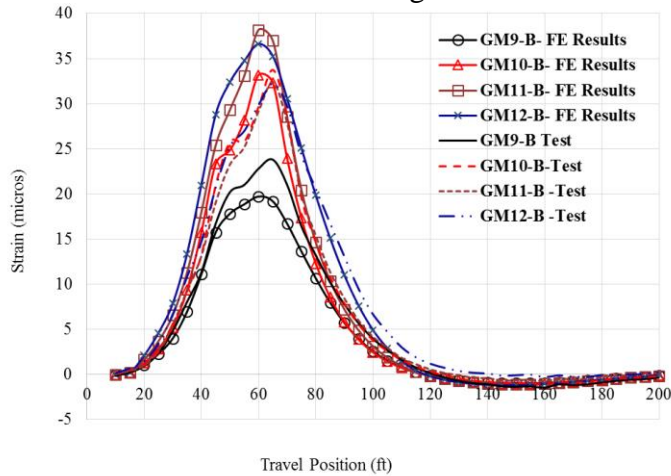
Figure 75. Strain comparisons between FE and test results at Section A



Girders 1 through 4

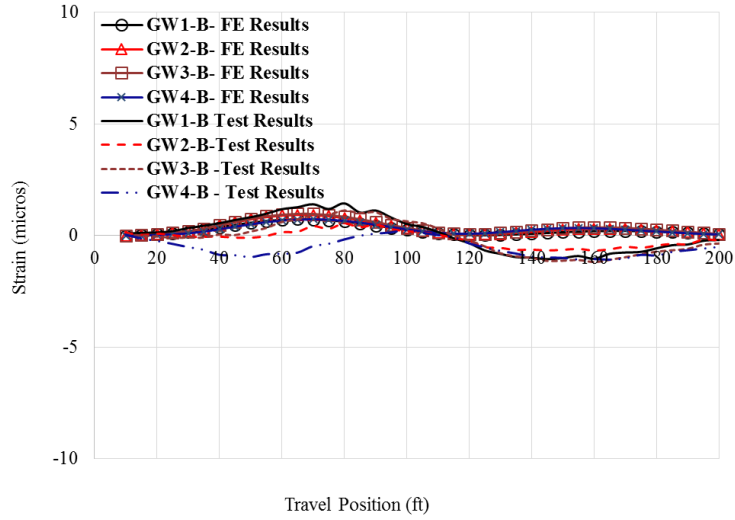


Girders 5 through 8

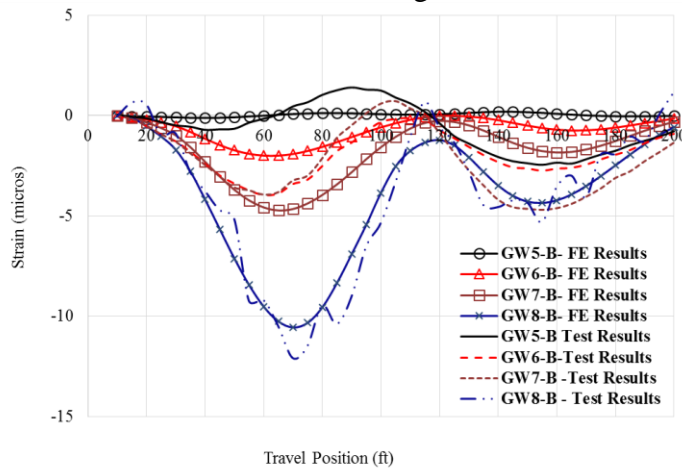


Girders 9 through 12

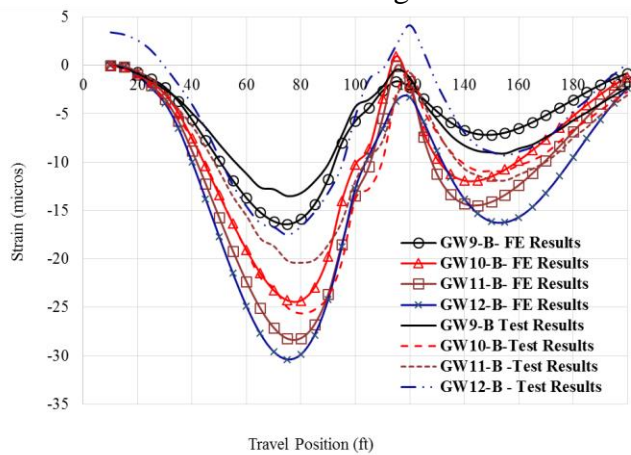
Figure 76. Strain comparisons between FE and test results at Section M



Girders 1 through 4

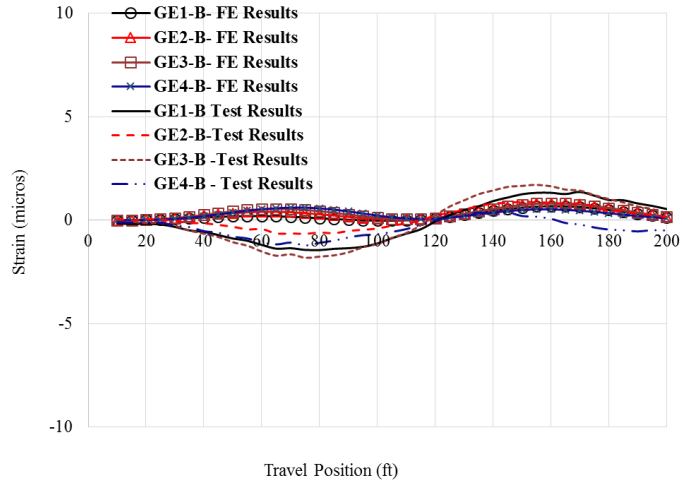


Girders 5 through 8

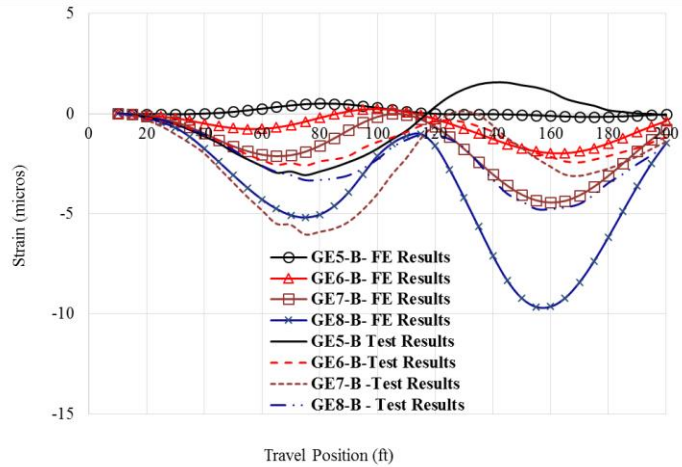


Girders 9 through 12

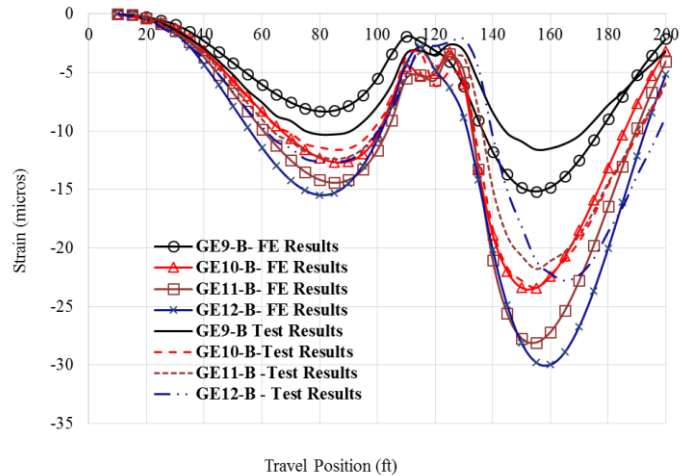
**Figure 77. Strain comparisons between FE and test results at Section P1**



Girders 1 through 4



Girders 5 through 8



Girders 9 through 12

Figure 78. Strain comparisons between FE and test results at Section P2

Figure 75 through Figure 78 indicate that the FE predictions follow the same order as the test results and the major differences are the magnitudes of the strain response. The discrepancy is due to the modeling errors, uncertainties associated with the transverse and longitudinal truck positions, uncertainties within the boundary conditions, etc.

As shown in Figure 77 and Figure 78, the large tensile strains in the bottom flanges indicate that the girders sustain negative moments, and a good continuity exists in the pier locations.

All in all, the bridge response can be well captured by the FE model. The comparison results indicate that the bridge has good span-to-span continuity at the pier location and good deck continuity for prefabricated bridge systems, and the UHPC longitudinal joints and the HPC transverse joints at the pier location are sufficient for the modular bridge systems of ABC projects.

## SUMMARY AND CONCLUSIONS

In this project, the performance and benefits of using PBES connected by closure pour connections were evaluated. The bridge replacement project consisting of the replacement of a bridge located on Iowa 92 over Little Silver Creek in Pottawattamie County, Iowa was used to demonstrate this ABC technique.

To further verify the adequacy of this technique, the performance of a UHPC longitudinal joint detail and an HPC transverse joint detail that were used for the Little Silver Creek Bridge were studied through laboratory testing and numerical simulations. Additionally, field testing was conducted to evaluate the in-place integrity of the bridge.

Overall, bridge construction was viewed as a success to the Iowa DOT, the contractor, and the public living and working in the vicinity of the project. A notable reduction in user costs was realized by using ABC techniques. The use of this grant was an important step in the Iowa DOT's continued adoption of ABC techniques and technologies.

For the longitudinal connections, the following conclusions were drawn:

- The UHPC connections had no cracks or leakage in the joint nor at the interface due to early-age drying shrinkage and temperature changes.
- Under strength loading conditions, the jointed specimens had slightly lower cracking loads compared to those of the jointless specimens, no matter which joint surface preparation technique was used (i.e., form-retarder or form liners). It was deemed that the bond at the longitudinal connection interface is less than normal-strength concrete tensile strength. Of the various surface preparation techniques, the form liner, Plastic Sandblast, achieved the worst surface roughness and bond at the interface.
- A flexural-shear failure mode (i.e., concrete crushed near the loading location and diagonal cracks extended from a center support) was found in the jointless and jointed specimens. Cracks formed at the connection interface and no cracks or concrete crushing were found in the UHPC pour.
- The strength and ductility of the jointed specimens with a longitudinal closure pour connection are comparable to those of the jointless specimens.
- Using the developed FE models, the failure loads were accurately predicted, but the cracking and yield loads were over-estimated and the deflections at failure were underestimated.
- Using the developed STM model, the ultimate load capacity of the specimens were accurately estimated.

- Due to arching action in the deck, a viable design approach using strut-and-tie methodologies may be utilized to limit tension in the longitudinal joint.
- At the end of loading, the concrete of the diaphragm bottom tended to crush, and no fracture was observed in the longitudinal steel bars. Measured strains indicated good continuity.

To evaluate the behavior of the transverse closure pour connection used to longitudinally connect adjacent prefabricated elements of the Little Silver Creek Bridge, negative moment flexural strength tests were conducted. For comparison purposes, specimens with and without a compression block were designed, fabricated, instrumented, and tested. FE models were also established to carry out a performance evaluation of the two specimens and to aid in the interpretation of the test results. Additionally, hand calculations were performed taking advantage of the classical reinforced concrete beam design theory and combined with the FE results to estimate the moment capacity of the specimens. For the transverse connections, the following conclusions were drawn:

- The established FE models were sufficient at representing the structural behavior of the two transverse connection specimens. Overall, the FE models showed a higher stiffness and less ductility, under-estimated the cracking moments, and over-predicted the yielding moments. However, the FE models very well predicted the ultimate moment capacities of the two specimens.
- The connection with a compression block had higher yield and ultimate moment capacity than the connection without a compression block. For both specimens, most of the longitudinal steel bars in the deck yielded at the ultimate state, and the critical section was located at the girder end that was embedded within the diaphragm. The maximum compression strain was located at the bottom of the concrete diaphragm and in the vicinity of the steel girder bottom flange for connections with and without a compression block, respectively.
- To design both types of connections per the classic reinforced concrete design theory, an effective width equal to the girder bottom flange width can be assumed for the connection without a compression block, and the centroid of the compression force at the bottom of the girder bottom flange can be assumed for the connection with a compression block. The hand calculations provide reasonable estimations on the moment capacity of the two connections.
- The compression block increased the performance of the connection and served as a more effective transfer mechanism for the compressive forces. However, both connections with and without a compression block showed satisfactory performance and are safe under the factored loads per the AASHTO LRFD bridge design specifications.
- No significant difference was found between the two specimens in terms of the crack patterns. For both specimens, cracks were initially found on the deck top and near the edge of the diaphragm and ultimately propagated to the bottom region of the diaphragm.

To evaluate the behavior of the bridge, two on-site, controlled field tests (Test #1 and Test #2) were conducted approximately one year apart. Four different cross-sections of the bridge (i.e., abutment section, mid-span section, two pier sections) were instrumented during testing. A dump truck following four load paths on the bridge was utilized for the live load tests. Moment load distribution factors (LDFs) were calculated using the test data and compared with those derived using the AASHTO LRFD equations. An FE model of the Little Silver Creek Bridge was established and calibrated to further interpret the test data. The following conclusions were drawn:

- The LDFs based on test data compared reasonably well with those calculated using the AASHTO LRFD equations.
- The actual bridge is stiffer than that shown in the bridge plan sheets due to the extra stiffness contribution from higher material strengths of the HPC and UHPC, larger deck depth and haunch and the barrier on the bridge, and notable restraint at both the abutment and pier locations.

The bridge had good span-to-span continuity at the pier locations and good deck continuity between the prefabricated bridge elements, indicating that the UHPC longitudinal joints and the HPC transverse joints at the pier locations are sufficient for the modular bridge systems of ABC projects.

## **TECHNOLOGY TRANSFER**

Work related to this project was presented at the 2016 and 2017 Annual Transportation Research Board meetings.

- Deng, Y., B. Phares, A. J. Putz, and C. Carter. 2017. Performance Evaluation of Transverse HPC Closure Pour Connection for Use in Modular Bridge Construction. Presented at the 96th Annual Meeting of the Transportation Research Board, January 8–12, Washington, DC.
- Deng, Y., B. Phares, A. J. Putz, C. Carter, M. Nop, and D. Bierwagen. 2016. Performance Evaluation of Longitudinal UHPC Closure Pour Connection for Use in Modular Bridge Construction – Pairwise Comparison of Capacity and Ductility at Failure Limit State. Presented at the 95th Annual Meeting of the Transportation Research Board, January 10–14, Washington, DC.

## REFERENCES

- AASHTO. 2015. *AASHTO LRFD Bridge Design Specifications, Customary U.S. Units, 7th Edition, with 2015 and 2016 Interim Revisions*. American Association of State Highway and Transportation Officials, Washington, DC.
- AASHTO. 2010. *AASHTO LRFD Bridge Design Specifications, Customary U.S. Units, 5th Edition, with 2010 Interim Revisions*. American Association of State Highway and Transportation Officials, Washington, DC.
- ASCE. 2015. *2015 Infrastructure Report Card*. American Society of Civil Engineering, Reston, VA. [www.infrastructurereportcard.org/bridges/](http://www.infrastructurereportcard.org/bridges/).
- Deng, Y., T. R. Norton, and C. Y. Tuan. 2013. Numerical Analysis of Concrete-Filled Circular Steel Tubes. *Structures and Buildings*, Vol. 166, No. 1, pp. 3–14.
- Deng, Y. and G. Morcouc. 2013. Efficient Prestressed Concrete-Steel Composite Girder for Medium-Span Bridges. II: Finite-Element Analysis and Experimental Investigation. *Journal of Bridge Engineering*, Vol. 18, No. 12, pp. 1358–1372.
- Deng, Y., B. M. Phares, H. Dang, and J. M. Dahlberg. 2016a. Impact of Concrete Deck Removal on Horizontal Shear Capacity of Shear Connections. *Journal of Bridge Engineering*, Vol. 21, No. 3.
- Deng, Y., B. M. Phares, and O. W. Steffens. 2016b. Experimental and Numerical Evaluation of a Folded Plate Girder System for Short-Span Bridges – A Case Study. *Engineering Structures*, Vol. 113, pp. 26–40.
- Deng, Y., B. M. Phares, A. J. Putz, C. Carter, C., M. Nop, and D. Bierwagen. 2016c. Performance Evaluation of Longitudinal UHPC Closure Pour Connection for Use in Modular Bridge Construction: Pairwise Comparison of Capacity and Ductility at Failure Limit State. *Transportation Research Record: Journal of the Transportation Research Board*, No. 2592, pp. 65–75.
- Graybeal, B. A. 2010. Behavior of Ultra-High Performance Concrete Connections between Precast Bridge Deck Elements. *Proceedings of the 2010 Concrete Bridge Conference: Achieving Safe, Smart & Sustainable Bridges*, February 24–26, Phoenix, AZ.
- Hartwell, D. R. 2011. Laboratory Testing of Ultra High Performance Concrete Deck Joints for Use in Accelerated Bridge Construction. MS thesis. Iowa State University, Ames, IA.
- Hognestad, E. 1951. *A Study of Combined Bending and Axial Load in Reinforced Concrete Members*. University of Illinois Engineering Experiment Station, Bulletin Series No. 399, Bulletin No. 1.
- Lafarge Ductal. 2011. *Ductal Solutions*. Martin-Saint-Leon, J., ed. pp. 1–9.
- Li, L., Z. J. Ma, M. E. Griffey, and R. G. Oesterle. 2010. Improved Longitudinal Joint Details in Decked Bulb Tees for Accelerated Bridge Construction: Concept Development. *Journal of Bridge Engineering*, Vol. 15, No. 3, pp. 327–336.
- Mulholland, D., and M. Vander Wert. 2015. *Iowa Infrastructure: 2015 Report Card*. American Society of Civil Engineering, Reston, VA. [www.infrastructurereportcard.org/wp-content/uploads/2016/10/ASCE-Report-Card-2.16.15-FINAL-1.pdf](http://www.infrastructurereportcard.org/wp-content/uploads/2016/10/ASCE-Report-Card-2.16.15-FINAL-1.pdf).
- Phares, B. M., S. Jayathilaka, and L. Greimann. 2015. *Investigation of Negative Moment Reinforcing in Bridge Decks*. Bridge Engineering Center, Institute for Transportation, Iowa State University, Ames, IA.

- Russell, H. G. and B. A. Graybeal. 2013. *Ultra-High Performance Concrete: A State-of-the-Art Report for the Bridge Community*. FHWA-HRT-13-060. Federal Highway Administration, Turner-Fairbank Highway Research Center, McLean, VA.
- Schmidt, M. and E. Fehling. 2005. Ultra-High Performance Concrete: Research, Development and Application in Europe. *Special Publication*, American Concrete Institute, No. 228.
- Shoup, L., N. Donohue, and M. Lang. 2011. *The Fix We're in For: The State of Our Nation's Bridges*. Retrieved March 2, 2016 from the Transportation for America website: [t4america.org](http://t4america.org).
- Ollgard, J. G., R. G. Slutter, and J. W. Fischer. 1971. Shear Strength of Stud Connectors in Lightweight and Normal Concrete. *Engineering Journal*, Vol. 8, pp. 55–64.
- Wee, T. H., M. S. Chin, and M. A. Mansur. 1996. Stress-Strain Relationship of High-Strength Concrete in Compression. *Journal of Materials in Civil Engineering*, Vol. 8, No. 2, pp. 70–76.



**THE INSTITUTE FOR TRANSPORTATION IS THE FOCAL POINT FOR TRANSPORTATION  
AT IOWA STATE UNIVERSITY.**

**InTrans** centers and programs perform transportation research and provide technology transfer services for government agencies and private companies;

**InTrans** manages its own education program for transportation students and provides K-12 resources; and

**InTrans** conducts local, regional, and national transportation services and continuing education programs.



**IOWA STATE  
UNIVERSITY**

Visit [www.InTrans.iastate.edu](http://www.InTrans.iastate.edu) for color pdfs of this and other research reports.